5-2014

On a combined adaptive tetrahedral tracing and edge diffraction model

Carl R. Hart
University of Nebraska-Lincoln, carl.hart@huskers.unl.edu

ON A COMBINED ADAPTIVE TETRAHEDRAL TRACING AND EDGE DIFFRACTION MODEL

By

Carl R. Hart

A DISSERTATION

Presented to the Faculty of

The Graduate College at the University of Nebraska

In Partial Fulfillment of Requirements

For the Degree of Doctor of Philosophy

Major: Architectural Engineering

Under the Supervision of Professors Siu-Kit Lau and Lily Wang

Lincoln, Nebraska

May, 2014

ON A COMBINED ADAPTIVE TETRAHEDRAL TRACING AND EDGE DIFFRACTION MODEL

Carl R. Hart, Ph.D.

University of Nebraska, 2014

Advisers: Siu-Kit Lau and Lily Wang

A major challenge in architectural acoustics is the unification of diffraction models and geometric acoustics. For example, geometric acoustics is insufficient to quantify the scattering characteristics of acoustic diffusors. Typically the time-independent boundary element method (BEM) is the method of choice. In contrast, time-domain computations are of interest for characterizing both the spatial and temporal scattering characteristics of acoustic diffusors. Hence, a method is sought that predicts acoustic scattering in the time-domain.

A prediction method, which combines an advanced image source method and an edge diffraction model, is investigated for the prediction of time-domain scattering. Adaptive tetrahedral tracing is an advanced image source method that generates image sources through an adaptive process. Propagating tetrahedral beams adapt to ensonified geometry mapping the geometric sound field in space and along boundaries. The edge diffraction model interfaces with the adaptive tetrahedral tracing process by the transfer of edge geometry and visibility information. Scattering is quantified as the contribution of secondary sources along a single or multiple interacting edges. Accounting for a finite number of diffraction permutations approximates the scattered sound field. Superposition of the geometric and scattered sound fields results in a synthesized impulse response between a source and a receiver.

Evaluation of the prediction technique involves numerical verification and numerical validation. Numerical verification is based upon a comparison with

analytic and numerical (BEM) solutions for scattering geometries. Good agreement is shown for the selected scattering geometries. Numerical validation is based upon experimentally determined scattered impulse responses of acoustic diffusors. Experimental data suggests that the predictive model is appropriate for high-frequency predictions. For the experimental determination of the scattered impulse response the merits of a maximum length sequence (MLS) versus a logarithmic swept-sine (LSS) are compared and contrasted. It is shown that a LSS is an appropriate stimuli for testing acoustic diffusors by comparing against scattered relative levels measured by a MLS signal.

Acknowledgments

I wish to express my sincere gratitude to several people that made this research a possibility. First, I thank Siu-Kit Lau for his patient mentoring and his tremendous support during my research. His guidance and research philosophy has shaped to a large extent my perspective on conducting research. The camaraderie and support fostered by the Nebraska Acoustics Group is due to Lily Wang. The group has served each member in many ways professionally. Much appreciation goes to Peter D'Antonio for hosting and mentoring my brief stay at RPG Diffusor Systems, Inc. Many thanks goes to him for providing access to his excellent goniometer. I am sincerely grateful to my parents for their tremendous support. Lastly, I thank my heavenly Father for making this venture a possibility in the first place.

Contents

List of Figures

List of Tables

Chapter 1

Introduction

A major challenge in architectural acoustics is the unification of diffraction models and geometric acoustics (Vorländer, 2008, p. 207). Geometric acoustics approximates the high frequency portion of an acoustic sound field, conceptualizing sound as the passage of rays, or as an ensemble of physical and image sources. Diffraction models account for the lower frequency portion of the sound field by predicting the scattering of sound from either geometric discontinuities or shadowing edges. Geometric acoustics alone is insufficient to characterize the sound field for a large number of elementary cases. For example, predicting the sound field of a source in the vicinity of a finite reflector is far from accurate with a geometric acoustic prediction. Alternatively, coupling a diffraction model with geometric acoustics better approximates the sound field. The unification of geometric acoustics and a diffraction model is one particular challenge addressed in this dissertation. In the context of this challenge acoustic diffusors serve as the primary case study for the combined model.

An acoustic diffusor is an architectural element that spreads the reflection of sound spatially and/or temporally (Schroeder, 1975; Schroeder and Gerlach, 1976; Schroeder, 1979). The ideal acoustic diffusor scatters sound energy into all

directions uniformly at all frequencies and temporally stretches the reflected sound into infinite time. However, physical limitations imposed by finite geometries constrains the extent of spatial and temporal spreading of reflected sound energy. Notwithstanding such limitations targeted diffusion is possible by crafting a surface in a specific manner to achieve a desired performance. The manner of crafting a surface for acoustic diffusion is informed by a knowledge of acoustic boundary interactions.

Variations in the geometric profile of a surface results in delayed reflections and diffraction. Similarly, variations in surface impedance results in the same propagation mechanisms with the possible addition of acoustic absorption. In contrast to specular reflection the combined effect of either delayed reflections or diffraction results in varying degrees of spatial and/or temporal spreading of sound energy. Anticipating the performance of an acoustic diffusor is an essential element in the development and evaluation process. Thus, an elementary basis for the prediction of scattering by acoustic diffusors is to compute the effects of delayed reflections and diffraction.

Of the numerical techniques available for predicting scattering by acoustic diffusors the most common technique is the boundary element method (BEM) (Cox and Lam, 1994; Cox, 1995). A central aspect of the BEM is the discretization of a contour for the purpose of solving the Kirchhoff–Helmholtz equation. The solution converges provided that the discretized elements of the contour are of the order of a fractional wavelength. As shorter and shorter wavelengths are modeled a corresponding increase in elements are required for solution convergence. Given infinite computational resources this aspect of the BEM is of no concern, but the finite computational resources available to the curious investigator or designer imposes a restriction for broadband prediction. Thus, an opportunity to minimize, or eliminate altogether, the discretization of space is an appealing approach to

broadband scattering prediction.

1.1 Research Objectives

The purpose of this research is to address the problem of predicting scattering by acoustic diffusors over a broadband frequency range. Combining the concepts of geometric acoustics and the viewpoint that an acoustic diffusor is an ensemble of scattering edges [cf. (Kinney et al., 1983; Novarini and Medwin, 1985)] leads to a particularly useful approach. Three primary challenges form the core of investigating this approach. In the context of predicting scattering, the first challenge is to define a relevant algorithm for geometric acoustics. The second challenge is to investigate the manner of unifying the geometric acoustic method, defined in the first challenge, with an edge diffraction model. Finally, the last challenge is to numerically verify, and validate the proposed approach for predicting scattering by acoustic diffusors. Each of these three challenges are cast into research objectives below.

The first objective is to define a relevant algorithm for geometric acoustics in the context of scattering prediction. Existing geometric acoustic methods include image sources (Allen and Berkley, 1979), ray tracing (Kulowski, 1985), and variations of beam tracing. Variations of beam tracing include classical beam tracing (Lewers, 1993), cone tracing (Dalenbäck, 1996), and adaptive beam tracing (Campo et al., 2000; Drumm and Lam, 2000). Inherently the image source method, ray tracing, classical beam tracing, and cone tracing lack the capability for diffraction prediction since diffracting edges are not precisely identified (Stephenson, 1996). Alternatively, adaptive beam tracing has many merits to recommend it for scattering predictions. The adaptive nature of the method lends itself to the precise identification of scattering edges, and the spatial coherence of propagating beams enables the use of a point source and a point receiver. As opposed to image sources, or ray tracing,

implementation of the adaptive beam tracing method presents a significant challenge due to the sparsity of algorithmic details. Therefore, the algorithm for adaptive beam tracing is to be defined as clearly and thoroughly for the purpose of scattering prediction.

The second objective is to investigate the unification of adaptive beam tracing and a secondary source model for edge diffraction (Svensson et al., 1999; Svensson and Calamia, 2006). Identifying common elements between geometric acoustics and edge diffraction serves as a basis for unifying the two methods. For any significantly complex surface, scattering is a mutual interaction of edges, surfaces, and vice versa. It is conceivable that the number of scattering combinations reaches an astronomical magnitude. Thus, the combinatorial nature of surface scattering necessitates a form of approximation. The manner of approximating total scattering and the issue of interfacing geometric acoustics and edge diffraction are the primary topics of this objective.

Lastly, the third objective is to numerically verify, and validate the computational approach investigated in objectives one and two. Numerical verification is conducted by comparing against analytic and numerical solutions of scattering geometries. Elementary scattering configurations serve as an initial check upon the accuracy of the proposed method. Numerical validation is achieved by a comparison against experimental results for diffusor scattering. The scattered impulse response is experimentally determined by a goniometer (Cox and D'Antonio, 2009, ch. 4). An acoustic excitation, such as a maximum length sequence (MLS), or a logarithmic swept–sine (LSS), is emitted from a loudspeaker, interacts with a diffusor at the center of a microphone array, and the back–scattered signal is captured by the array. The scattered impulse response is computed through digital signal processing techniques. Results gathered by the goniometer are compared against scattering predictions.

1.2 Numerical Computation of Acoustic Scattering Overview

Prediction methods for acoustic scattering are numerous with varying forms of assumptions, approximations, and conceptual approaches. Of all the methods available each can be categorized into one of two approaches: approximately solve the wave equation, or employ a semi-analytical technique. For low frequencies, approximate solutions to the wave equation are possible, but the computational demands increase as the analysis goes higher in frequency (Bies and Hansen, 2009, p. 618). Alternatively, semi-analytical approaches utilize analytical solutions to specific scattering geometries. An excellent review of methods for scattering prediction by acoustic diffusors is given by Cox and D'Antonio(2009, ch. 8). A brief overview of the wave based methods and semi-analytical approaches relevant to predicting scattering follows. Theoretical details are provided in Chapter 2.

1.2.1 Wave Based Methods

Wave based methods solve the well-known wave equation through numerical means. Three common methods exist: the finite element method (FEM) (Zienkiewicz et al., 2005a), the boundary element method (BEM) (Schenck, 1968), and the finite difference time-domain method (FDTD) (Botteldooren, 1994). The FEM and BEM recasts the wave equation into an integral form in order to solve a system of equations based on the discretization of either space or boundaries. Assuming the source is time–harmonic, solutions are computed at specific frequencies by transforming the wave equation into the time-invariant Helmholtz equation. The FDTD solves the elementary differential equations that govern the conservation of mass and momentum through finite difference schemes. Numerical solutions are computed within the time-domain.

The advantages of utilizing wave based methods include the accurate accounting of wave scattering and reflection. Generally, solutions are shown to coincide with experimental results and serve as a proper baseline for verification purposes. Disadvantages include the complex modeling of anechoic boundaries, the high computational cost of solving large geometric domains, or determining high frequency solutions. Plus, modeling time-domain impedance boundary conditions is complicated by the fact that current solutions either rely on a simplistic physical model, which is only applicable for low frequencies (Richter et al., 2011), or rely upon fitting a digital filter's frequency response to the impedance frequency response (Escolano et al., 2008). Frequency based impedance models are well established; however, time-domain impedance models are undergoing continual development.

1.2.2 Semi-analytical Methods

Semi-analytical methods combine solutions for scattering by simple geometries and extends the prediction to an ensemble of geometric features, replicating the base form. For example, boss models begin with a solution to the scattering of a semi–cylinder or hemisphere. The solution is extended to a periodic or random arrangement of semi–cylinders or hemispheres for the overall scattering (Lucas and Twersky, 1984). Another approach is to utilize the solution for a diffracting edge (Biot and Tolstoy, 1957). A geometric scattering surface is viewed as an ensemble of diffracting edge (Novarini and Medwin, 1985) and the overall scattered response is computed.

Advantages of a semi-analytical approach include fast solutions and a physical insight into the scattering problem. Since discretization is either avoided, or is of a low spatial order, it is expected that computations surpass the speed of wave based methods. Plus, computations conducted in the time domain permits the identification of individual scattering mechanisms, as opposed to continuous–wave

computations. Since an elementary geometric form is the basis of computation a disadvantage is the lack of geometric generality. Furthermore, if mutual reflections of scattering are significant then an image method must be employed. Despite the disadvantages of a semi-analytical approach it is shown that the combination of an advanced image source method with an edge diffraction model, as pursued in this dissertation, may be well suited to predict scattering in a number of cases, such as for acoustic diffusors.

1.3 Dissertation Overview

This dissertation proceeds with a chapter on the theory of scattering prediction methods, a chapter addressing each research objective, and a chapter with concluding remarks. Chapter 2 addresses the theoretical foundations of numerical methods relevant to scattering predictions. The foundations of the finite element method, finite difference time domain method, boundary element method, image sources, ray tracing, and classical beam tracing are described at length. Chapter 3 details the algorithmic structure of the adaptive tetrahedral tracing method, a variation on adaptive beam tracing. The process of the algorithm is defined by description and illustrations. Chapter 4 describes a secondary source model for edge diffraction, a unification of the edge diffraction model and adaptive tetrahedral tracing, and numerical verification of the proposed method. Numerical verification is shown for a rigid wedge and a reflecting panel geometry. Chapter 5 presents comparisons between the proposed scattering prediction method and experimental results from acoustic diffusors. The selected acoustic diffusors include designs based on primitive geometry, and number theory. Furthermore, a comparison of experimental results is made between two excitation signals: a maximum length sequence, and a logarithmic swept-sine. The concluding chapter, Ch. 6, offers final

remarks on the capabilities/limitations of the proposed scattering prediction method, and thoughts on future work.

1.4 Contributions

The contributions of this dissertation are as follows:

- A detailed algorithmic description of adaptive tetrahedral tracing is provided.
- A semi-analytical approach based on the fusion of adaptive tetrahedral tracing and a secondary source model for edge diffraction is presented.
- The scattering predictions of the semi-analytical approach are evaluated against experimental measurements of acoustic diffusors.
- Comparisons are given for goniometer measurements based on either a maximum length sequence signal or a logarithmic swept-sine signal.

Chapter 2

Scattering Prediction Methods

The prediction of sound scattering is an essential technique in architectural acoustics. For acoustic diffusors it is an essential element for the evaluation of diffusor designs (Cox and Lam, 1994), numerical optimization of diffusors (Cox, 1995), and the computation of scattering coefficients for geometric room modeling (Cox and D'Antonio, 2009, pp. 143–147, 416). Chapter 1 mentions in brief two types of prediction strategies that address sound scattering: wave based methods and semi-analytical methods. This chapter details the theory of wave based methods and semi-analytical methods relevant to acoustic scattering. Section 2.1 outlines the wave equation as the basis for the numerical methods described in the following sections. The theory of the finite element method (FEM) is described in Section 2.2. Next, the basis for the boundary element method (BEM) is given in Section 2.3. Following, the fundamentals of the finite difference time domain (FDTD) method are covered in Section 2.4. The boss model is described in Section 2.5. Edge diffraction models are described in Section 2.6, with particular emphasis on a secondary source model for edge diffraction.

2.1 The Wave Equation and Boundary Conditions

The linear homogeneous wave equation has its basis upon the linear equations of state, continuity, and momentum (Kinsler et al., 2000, pp. 113-120). The linear equation of state relates acoustic pressure to small variations in condensation,

$$p(\vec{r},t) = Bs(\vec{r},t), \tag{2.1}$$

where p is the acoustic pressure, s is condensation, B is the adiabatic bulk modulus, $\vec{r} = (x, y, z)$ is the field position vector, and t is time. The thermodynamic speed of sound is related to the adiabatic bulk modulus by,

$$c^2 = B/\rho_0, \tag{2.2}$$

where c is the speed of sound, and ρ_0 is the equilibrium density of the medium. The linear equation of continuity embodies the principle of conservation of mass,

$$\rho_0 \frac{\partial s(\vec{r},t)}{\partial t} + \nabla \cdot [\rho_0 \vec{u}(\vec{r},t)] = 0, \tag{2.3}$$

where $\vec{u}$ is the acoustic particle velocity, and ∇ is the gradient operator. Finally, the linear equation of momentum casts Newton's second law in a differential form,

$$\rho_0 \frac{\partial \vec{u}(\vec{r},t)}{\partial t} + \nabla p(\vec{r},t) = 0. \tag{2.4}$$

The essential equations above relating state, conservation of mass, and a balance of forces directly lead to the linear homogeneous wave equation.

The linear homogeneous wave equation is derived from Eqs. (2.1)–(2.4) resulting

in a fundamental equation of acoustics. The derivation proceeds by taking the second time derivative of the equation of state, Eq. (2.1), applying a time derivative to the equation of continuity, Eq. (2.3), and finally taking the divergence of the equation of momentum, Eq. (2.4). Substitution and rearrangement of the resulting equations leads to the linear wave equation,

$$\nabla^2 p(\vec{r},t) - \frac{1}{c^2}\frac{\partial^2 p(\vec{r},t)}{\partial t^2} = 0, \tag{2.5}$$

where ∇^2 is the Laplace operator. Equation (2.5) physically relates the transport of acoustic waves over space and time in a non-dispersive medium. The velocity of acoustic wave propagation is the speed of sound c.

A scattering problem is characterized as a boundary-value problem distinguished by an unbounded domain and the presence of a source. A source that characterizes mass injection at a rate per unit volume is introduced into the equation of continuity, Eq. (2.3), (Kinsler et al., 2000, pp. 140–142),

$$\rho_0 \frac{\partial s(\vec{r},t)}{\partial t} + \nabla \cdot [\rho_0 \vec{u}(\vec{r},t)] = f(\vec{r},t), \tag{2.6}$$

where f is a source term radiating as a monopole. The inclusion of a source results in the inhomogeneous linear wave equation,

$$\nabla^2 p(\vec{r},t) - \frac{1}{c^2}\frac{\partial^2 p(\vec{r},t)}{\partial t^2} = -\frac{\partial f(\vec{r},t)}{\partial t}. \tag{2.7}$$

The wave equation as posed in Eqs. (2.5) and (2.7) are hyperbolic partial differential equations. Separation of the time variable reduces the hyperbolic partial differential equation into an elliptic partial differential equation. Assume the

acoustic pressure to be time harmonic,

$$p(\vec{r},t) = p(\vec{r})e^{j\omega t}, \tag{2.8}$$

where j is the imaginary number ($\sqrt{-1}$), and ω is the radial frequency. Assume the source term f is time-harmonic, as the acoustic pressure, and substitute the acoustic pressure, Eq. (2.8) into the linear wave equation, Eq. (2.7), resulting in the inhomogeneous Helmholtz equation,

$$\nabla^2 p(\vec{r}) + k^2 p(\vec{r}) = -j\omega f(\vec{r}), \tag{2.9}$$

where $k = \omega/c$ is the wave number. An unbounded domain physically requires waves to diminish at infinity. The boundary which satisfies this requirement is Sommerfeld's radiation condition for three-dimensional space (Sommerfeld, 1949, p. 189),

$$\lim_{r\to\infty} r\left(\frac{\partial p(\vec{r})}{\partial r} + jkp(\vec{r})\right) = 0, \tag{2.10}$$

where r is the radial coordinate in spherical coordinates.

A well-posed scattering problem requires specification of the scattering boundary condition. In mathematical terms various boundary conditions may be specified: a Dirichlet boundary condition, a Neumann boundary condition, or a Robin boundary condition. For the purposes of rigid scattering a Neumann boundary condition is,

$$\nabla p(\vec{r}) \cdot \hat{n} = \frac{\partial p(\vec{r})}{\partial n} = 0 \text{ on } \Gamma, \tag{2.11}$$

where the vector $\hat{n}$ is the unit normal vector to the boundary Γ and it is understood that the partial derivative is with respect to the boundary normal, see Fig. 2.1. The boundary condition in Eq. (2.11) indirectly states that the particle velocity is zero in the normal direction relative to the boundary (cf. Eq. (2.4)), signifying a rigid

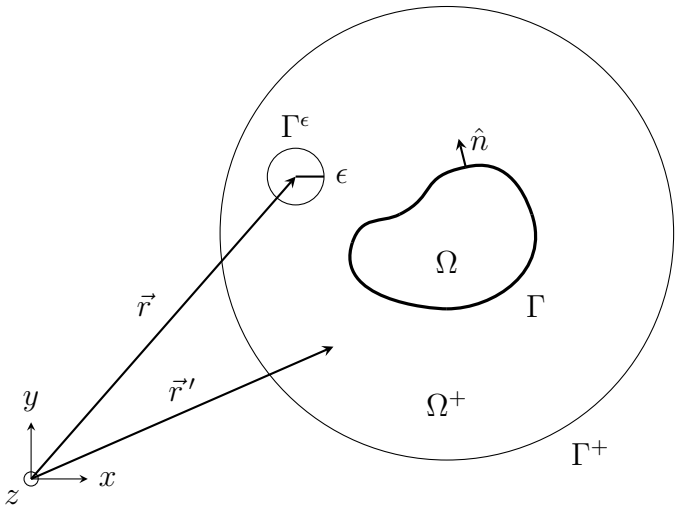

Figure 2.1: An acoustic scattering geometry in three-dimensional space is characterized by an unbounded domain, Ω^+, with one or more scattering objects. The scattering object encloses a domain Ω with a boundary Γ. The outward unit normal $\hat{n}$ is defined everywhere on Γ. The vector $\vec{r}$ is the observation position vector, and $\vec{r}'$ is a variable position vector. A infinitesimally small sphere, with radius ϵ, encloses the point in space at the observation position vector.

surface. A scattering problem is not restricted to simply rigid scattering. In a similar vein a radiation problem is posed by specifying a Dirichlet boundary condition,

$$p(\vec{r}) = h(\vec{r}) \text{ on } \Gamma, \tag{2.12}$$

where no source term exists other than what is specified on the boundary. Finally, an impedance boundary condition is given as a Robin boundary condition,

$$\frac{\partial p(\vec{r})}{\partial n} - jk\zeta'(\vec{r})p(\vec{r}) = 0 \text{ on } \Gamma, \tag{2.13}$$

where ζ' is the surface admittance defined with an outward pointing normal ($\zeta' = -\zeta$ where ζ is defined with an inward pointing normal).

The time-harmonic forms of the FEM and BEM have their basis in the Helmholtz equation, Eq. (2.9), for scattering predictions.

2.2 Finite Element Method

The FEM originated from solution techniques bearing on problems of a continuous nature (Zienkiewicz et al., 2005b). Physical phenomena such as fluid flow or structural displacements are inherently continuous and have a mathematical description as a partial differential equation. The FEM approximates the solution of a partial differential equation by subdividing the continuum into many small elements where the constitutive equations hold locally. Hence, the partial differential equation is discretized mathematically in space and/or time. By transforming the linear wave equation, Eq. (2.7), into the time-invariant Helmholtz equation, Eq. (2.9), a boundary-value problem forms the basis for discretizing the acoustic scattering problem in space.

In order to estimate the solution of acoustic scattering a finite domain must be imposed upon the problem. The restriction of a finite domain is based upon the fact that space is discretized in the FEM. Therefore, a finite domain is a necessary requirement for estimating a solution. For a three-dimensional geometry a sphere serves as a possible artificial boundary. The annular region between the artificial boundary Γ^+ and the scattering boundary Γ is denoted as Ω^+; see Fig. 2.1. Within the annular region, Ω^+, the sound field is computed for acoustic scattering. The essential requirement for the artificial boundary is that it satisfies Sommerfeld's radiation condition, Eq. (2.10). In other words the artificial boundary ideally acts as a non-reflecting boundary. A major challenge is defining the boundary condition of Γ^+ such that incident and scattered waves are not reflected back into the acoustic domain.

Several approaches exist for specifying the artificial boundary condition. A naive approach would be to simply set the boundary condition to Sommerfeld's radiation condition, neglecting the limit. Experience has shown that this approach results in poor approximations to the acoustic field (Givoli, 1992, pp. 49–51, 193–198).

Fortunately, other approaches exist which include non-reflecting boundary conditions, sponge layers (also known as perfectly matched layers), infinite elements, and Dirichlet to Neumann mapping (Givoli, 1992). Each technique has its own merits and drawbacks; however, a thorough discussion of each is beyond the scope of this work. Provided an appropriate artificial boundary condition is selected, the acoustic scattering problem is well defined.

The problem statement for acoustic scattering is defined by Eq. (2.9), applicable in Ω^+, one of the boundary conditions (Eqs. (2.11)–(2.13)) specified on Γ, and the appropriate artificial boundary condition. The problem statement has an equivalent integral form. Multiplying Eq. (2.9) by an arbitrary function $v(\vec{r})$, commonly known as a test function, and integrating over the annular domain yields (Zienkiewicz et al., 2005b, ch. 3),

$$0 = \int_{\Omega^+} \left[v(\vec{r})\nabla^2 p(\vec{r}) + k^2 v(\vec{r}) p(\vec{r}) + j\omega v(\vec{r}) f(\vec{r}) \right] \, \mathrm{d}\Omega^+, \tag{2.14}$$

where $\mathrm{d}\Omega^+$ is a differential element of the domain Ω^+. The differential element is a volume element for a three-dimensional domain or an area element for a two-dimensional domain. Utilizing Green's theorem for Eq. (2.14) transforms the integral relation into,

$$\begin{aligned} 0 = & \int_{\Omega^+} \left[-\nabla v(\vec{r}) \cdot \nabla p(\vec{r}) + k^2 v(\vec{r}) p(\vec{r}) + j\omega v(\vec{r}) f(\vec{r}) \right] \, \mathrm{d}\Omega^+ \\ & + \int_{\Gamma^+} v(\vec{r}) \frac{\partial p(\vec{r})}{\partial n} \, \mathrm{d}\Gamma^+ - \int_{\Gamma} v(\vec{r}) \frac{\partial p(\vec{r})}{\partial n} \, \mathrm{d}\Gamma, \end{aligned} \tag{2.15}$$

where $\mathrm{d}\Gamma$ is a differential element of Γ, similarly for Γ^+. The differential element is an area element for a three-dimensional surface or a line element for a parametric contour in two-dimensions. Eq. (2.15) is known as the *weak form* of Eq. (2.9). This problem statement is equivalent to satisfying Eq. (2.9) and any imposed boundary conditions on Γ (Givoli, 1992, pp. 245–248). Utilizing an integral formulation is

advantageous compared to the differential form since solutions admit a discontinuity of material properties (Zienkiewicz et al., 2005b, p. 60). The differential form assumes a strict smoothness in its formulation compared to realistic scenarios.

Once the integral form of the scattering problem is established an approximate solution is computed. First, the subdomain Ω^+ is subdivided into a mesh of geometric elements known as finite elements. The acoustic pressure is approximated as a discrete set of nodal pressures within each finite element and weighted with a set of basis functions. The test function is approximated similar to the acoustic pressure, being weighted with the same set of basis functions known as shape functions. In order for the solution to converge, the shape functions must satisfy certain continuity conditions (Zienkiewicz et al., 2005b, pp. 74–75). The local equations for each finite element are numerically integrated. Next, the local equations for each finite element are linked together to form a global set of linear equations with unknown nodal values of acoustic pressure. Finally, the linear equations are solved for the unknown pressure values. This method describes a quick sketch of the Galerkin method as it applies to solving the integral equation, Eq. (2.15), of acoustic scattering (Givoli, 1992, pp. 252, 253).

The FEM is a highly general method with the capability to solve coupled phenomena, such as elastic scattering. In the context of predicting acoustic scattering, it agrees well with BEM predictions for specular scattering angles (Redondo et al., 2007). In contrast, a consistent difference is shown between the FEM and BEM predictions for scattering angles far from the specular angle. In the study conducted by Redondo et al. (2007), the near field of an acoustic diffusor is computed by the FEM, and the far-field polar response is computed by the Helmholtz-Kirchhoff integral, Eq. (2.23). Compared to other numerical techniques the FEM does have some challenges.

Some challenges of the FEM are the increasing computational requirements as

the wavenumber increases, propagation errors, and the use of an absorbing boundary condition. In order to resolve wave propagation at smaller scales, space must be discretized to smaller scales as well. As a result the intermediate system of linear equations become larger. Hence, the demand upon computational resources becomes larger as shorter wavelengths of propagation are modeled (Zienkiewicz et al., 2005a, ch. 12). Another challenge inherent in the FEM are propagation errors. Two types of errors exist for the FEM: incorrect wave shape and incorrect wavelength (Zienkiewicz et al., 2005a, pp. 319, 351). These errors are only reduced by discretizing space to smaller scales and/or increasing the polynomial order of the shape functions. Lastly, care must be taken in the selection of an absorbing boundary condition in order to reduce spurious reflections from the artificial boundary. In spite of the challenges for solving scattering problems by the FEM, the state of the art is increasingly incorporating wave behavior into the solution algorithm, reaching new levels of computational capability (Thompson, 2006).

2.3 Boundary Element Method

The BEM approaches the scattering problem similarly to the FEM by transforming the Helmholtz equation, Eq. (2.9), into an integral equation. First, a Green's function is defined which satisfies the Helmholtz equation,

$$\nabla^2 G(\vec{r};\vec{r}\,') + k^2 G(\vec{r};\vec{r}\,') = \delta(\vec{r}-\vec{r}\,'), \tag{2.16}$$

where G is the Green's function, δ is the Dirac-delta function, and $\vec{r}\,'$ is a variable position vector, see Fig. 2.1. In the exterior domain, Ω^+, Eq. (2.16) is homogeneous since the observation position vector, $\vec{r}$, is excluded from the domain by the spherical surface Γ^ϵ, with radius ϵ. In the following derivation the gradient operator is symbolized as ∇' denoting differentiation with respect to $\vec{r}\,'$. Multiplying the

homogeneous form of Eq. (2.16) with acoustic pressure, multiplying the inhomogeneous Helmholtz equation, Eq. (2.9), with the Green's function, and subtracting the two equations results in,

$$p(\vec{r}\,')\nabla'^2 G(\vec{r};\vec{r}\,') - G(\vec{r};\vec{r}\,')\nabla'^2 p(\vec{r}\,') = -j\omega G(\vec{r};\vec{r}\,')f(\vec{r}\,'). \tag{2.17}$$

Integrating Eq. (2.17) over the exterior domain Ω^+,

$$\int_{\Omega^+} \left[p(\vec{r}\,')\nabla'^2 G(\vec{r};\vec{r}\,') - G(\vec{r};\vec{r}\,')\nabla'^2 p(\vec{r}\,')\right] \mathrm{d}\Omega^+ = -j\omega \int_{\Omega^+} G(\vec{r};\vec{r}\,')f(\vec{r}\,')\,\mathrm{d}\Omega^+, \tag{2.18}$$

recognizing the right hand side of Eq. (2.18) as the incident acoustic pressure, and transforming the left hand side by Green's theorem results in,

$$-\int_{\partial\Omega^+} \left[p(\vec{r}\,')\frac{\partial G(\vec{r};\vec{r}\,')}{\partial n'} - G(\vec{r};\vec{r}\,')\frac{\partial p(\vec{r}\,')}{\partial n'}\right] \mathrm{d}(\partial\Omega^+) = p_i(\vec{r}), \tag{2.19}$$

where the unit normal vector $\hat{n}'$ is an alternative normal on Γ. The boundaries of Ω^+ are denoted as $\partial\Omega^+ = \Gamma^+ \cup \Gamma^\epsilon \cup \Gamma$. Let the radius of the boundary Γ^+ extend to infinity, then by the Sommerfeld radiation condition, Eq. (2.10), the integral over Γ^+ vanishes. Thus, two integrals remain over Γ and Γ^ϵ. The integral over Γ^ϵ is evaluated in the limit of ϵ going to zero, provided the three-dimensional free-field Green's function is,

$$G(\vec{r};\vec{r}\,') = \frac{e^{-jk\epsilon}}{4\pi\epsilon}, \tag{2.20}$$

where $\epsilon = |\vec{r} - \vec{r}\,'|$. The integral for Γ^ϵ as ϵ becomes vanishingly small is,

$$\lim_{\epsilon\to 0}\int_{\Gamma^\epsilon} \left[p(\vec{r}\,')\frac{\partial G(\vec{r};\vec{r}\,')}{\partial n'} - G(\vec{r};\vec{r}\,')\frac{\partial p(\vec{r}\,')}{\partial n'}\right] \mathrm{d}\Gamma^\epsilon = \lim_{\epsilon\to 0}\left[p(\vec{r})\frac{\partial}{\partial\epsilon}\left(\frac{e^{ik\epsilon}}{4\pi\epsilon}\right)4\pi\epsilon^2\right] = -p(\vec{r}). \tag{2.21}$$

Substituting Eq. (2.21) into Eq. (2.19) and rearranging terms results in the total acoustic pressure in Ω^+,

$$p(\vec{r}) = p_i(\vec{r}) + \int_\Gamma \left[p(\vec{r}\,') \frac{\partial G(\vec{r};\vec{r}\,')}{\partial n'} - G(\vec{r};\vec{r}\,') \frac{\partial p(\vec{r}\,')}{\partial n'} \right] \mathrm{d}\Gamma, \tag{2.22}$$

where the second term on the right signifies the scattered acoustic pressure. The expressions for the total acoustic pressure in either the exterior or scattering surface domains are (Burton and Miller, 1971),

$$\left.\begin{array}{ll} p(\vec{r}) & \vec{r} \in \Omega^+ \\ \frac{1}{2} p(\vec{r}) & \vec{r} \in \Gamma \end{array}\right\} = p_i(\vec{r}) + \int_\Gamma \left[p(\vec{r}\,') \frac{\partial G(\vec{r};\vec{r}\,')}{\partial n'} - G(\vec{r};\vec{r}\,') \frac{\partial p(\vec{r}\,')}{\partial n'} \right] \mathrm{d}\Gamma. \tag{2.23}$$

Within the interior domain, Ω, the total acoustic pressure is identically zero for a nontransparent surface. Eq. (2.23) is the basis for the boundary element method (BEM).

In the derivation of Eq. (2.23) the Green's function for a three-dimensional free-field was given; however, other Green's functions satisfy the Helmholtz equation for other dimensions. The Green's function for a two-dimensional free-field is,

$$G(\vec{r};\vec{r}\,') = -\frac{j}{4} H_0^{(2)}(kR), \tag{2.24}$$

where $R = |\vec{r} - \vec{r}\,'|$, and $H_0^{(2)}(kR)$ is the Hankel function of order zero of the second kind. The Hankel function is defined as,

$$H_0^{(2)}(kR) = J_0(kR) - jY_0(kR), \tag{2.25}$$

where J_0 and Y_0 are Bessel functions of the first and second kind, respectively. Assuming large separations of source and receiver, the two-dimensional Green's

function may be approximated as,

$$G(\vec{r};\vec{r}\,') = \frac{Ae^{-jkR}}{\sqrt{kR}}, \tag{2.26}$$

where A is a constant and the assumption is based on $k|\vec{r}-\vec{r}\,'| \gg 1$.

A particular challenge associated with the integral formulation for acoustic scattering, Eq. (2.23), is the presence of non-unique solutions for a specific set of wavenumbers. Whenever the wavenumber corresponds to a resonance of the interior domain, Ω, non-unique solutions exist for the total acoustic pressure (Burton and Miller, 1971). The issue of non-uniqueness is exacerbated as the wavenumber increases since the density of resonant wavenumbers increases for Ω. One approach to overcome the non-uniqueness issue is the Burton-Miller method (Burton and Miller, 1971). For rigid scattering the normal derivative of Eq. (2.23) is taken for observation positions on Γ, a weighting is applied to the resulting equation, and the weighted result is added to Eq. (2.23). For a particular weighting a unique solution is obtained for resonant wavenumbers. An alternative method is due to Schenck (1968). The Kirchhoff-Helmholtz equation for the interior is imposed upon a discrete set of interior points resulting in an overdetermined system of linear equations. The system of equations is solved by a least-squares procedure for acoustic pressure. Alternatively, if the scattering surface is not enclosed and can be approximated as an ensemble of thin panels, then the Kirchhoff-Helmholtz may be recast in an alternative manner, which avoids the non-uniqueness issue.

Application of the thin-panel assumption to the Kirchhoff-Helmholtz equation, Eq. (2.23), casts the problem in terms of pressure differences and pressure sums across a thin panel. The normal derivative of Eq. (2.23) is used with a variation of the Kirchhoff-Helmholtz equation to simultaneously solve for pressures at the front

and back of a surface (Terai, 1980),

$$\frac{1}{2}\left[p(\vec{r}_1)+p(\vec{r}_2)\right] = p_i(\vec{r}) + \int_\Gamma \left\{ \left[p(\vec{r}\,'_1)-p(\vec{r}\,'_2)\right]\frac{\partial G(\vec{r};\vec{r}\,')}{\partial n'} - G(\vec{r};\vec{r}\,')\left[\frac{\partial p(\vec{r}\,'_1)}{\partial n'}-\frac{\partial p(\vec{r}\,'_2)}{\partial n'}\right]\right\} \mathrm{d}\Gamma, \tag{2.27}$$

$$\frac{1}{2}\left[\frac{\partial p(\vec{r}_1)}{\partial n}-\frac{\partial p(\vec{r}_2)}{\partial n}\right] = \frac{\partial p_i(\vec{r})}{\partial n} + \int_\Gamma \left\{ \left[p(\vec{r}\,'_1)-p(\vec{r}\,'_2)\right]\frac{\partial^2 G(\vec{r};\vec{r}\,')}{\partial n \partial n'} - \frac{\partial G(\vec{r};\vec{r}\,')}{\partial n}\left[\frac{\partial p(\vec{r}\,'_1)}{\partial n'}-\frac{\partial p(\vec{r}\,'_2)}{\partial n'}\right]\right\} \mathrm{d}\Gamma, \tag{2.28}$$

where the front and rear of a surface element are denoted by the subscripts 1 and 2, respectively, and the expressions are evaluated on Γ. Eqs. (2.27) and (2.28) solve for the unknown acoustic pressure differences on the surface of a scattering object. Assuming the surface is rigid results in a simplification of Eqs. (2.27) and (2.28),

$$p(\vec{r}_1)+p(\vec{r}_2) = 2p_i(\vec{r}), \tag{2.29}$$

$$0 = \frac{\partial p_i(\vec{r})}{\partial n} + \int_\Gamma \left[p(\vec{r}\,'_1)-p(\vec{r}\,'_2)\right]\frac{\partial^2 G(\vec{r};\vec{r}\,')}{\partial n \partial n'}\,\mathrm{d}\Gamma. \tag{2.30}$$

Boundary elements assume the pressure difference across an element is constant, resulting in no need for discretizing the front and rear portions of a surface. Following the solution of surface pressure differences the total acoustic pressure in Ω^+ is calculated as,

$$p(\vec{r}) = p_i(\vec{r}) + \int_\Gamma \left[p(\vec{r}\,'_1)-p(\vec{r}\,'_2)\right]\frac{\partial G(\vec{r};\vec{r}\,')}{\partial n'}\,\mathrm{d}\Gamma. \tag{2.31}$$

One particular advantage of the BEM is the fact that the dimensionality of the problem is reduced by one. For example a three-dimensional problem requires the solution of surface integrals as opposed to volumetric integrals in the FEM. This is

advantageous due to the reduced number of elements required to mesh the scattering domain. Whereas in the FEM matrices are sparse, in the BEM full matrices arise due to the mutual interaction of boundary elements (Cox and D'Antonio, 2009, p. 257). For example, in order to solve an acoustic scattering problem, first the surface pressures must be computed. This first step is the most demanding computationally. Once the surface pressures are computed then the total pressure at an exterior field point is computed fairly quickly.

In the context of predicting scattering from acoustic diffusors, the BEM has found widespread application. The method was used to predict the scattering of a quadratic residue diffusor and constant depth diffusor (Cox and Lam, 1994), numerically optimize a stepped diffusor (Cox, 1995), predict the scattering of a wide variety of geometric and number theoretic diffusors (Hargreaves et al., 2000), predict the scattering of Lüke and power residue diffusors (Dadiotis et al., 2008), and predict the transient scattering of a quadratic residue diffusor using a time-domain BEM (Hargreaves and Cox, 2008). Lastly, the BEM was used to predict and compute the autocorrelation diffusion coefficient of a wide variety of diffusors in a text by Cox and D'Antonio (2009). The widespread use of the BEM for predicting the scattering of acoustic diffusors illustrates the strength of the technique for predicting acoustic scattering.

Nevertheless, the BEM is challenged when computing broadband acoustic scattering due to the large computational demands of the method. As a general rule it is necessary to specify the maximum size of elements as one-eighth, or smaller, of the smallest wavelength of interest (Cox and D'Antonio, 2009, p. 256). Thus, it becomes intractable to compute broadband acoustic fields via the traditional BEM within a reasonably short amount of time. For example, prediction of a quadratic residue diffusor by a standard BEM requires a fortyfold increase in time to extend the frequency range from 2900 Hz to 8700 Hz (Cox and Lam, 1994).

2.4 Finite Difference Time Domain Method

The finite difference time domain (FDTD) method originated within the electromagnetic community for predicting wave propagation in space and time. The first implementation of the method for acoustics was utilized to study an irregularly shaped acoustic cavity and duct bend (Botteldooren, 1994). Over time the method has matured and is applied to a variety of acoustic problems.

The governing equations of concern are the conservation of mass, Eq. (2.3), and momentum, Eq. (2.4). The equation of continuity is transformed into a relation between acoustic pressure and particle velocity by assuming the equilibrium density is isotropic, and substituting Eq. (2.1) into Eq. (2.3),

$$\frac{\partial p(\vec{r},t)}{\partial t} + B\nabla \cdot \vec{u}(\vec{r},t) = 0. \tag{2.32}$$

With the equations of continuity and momentum in terms of acoustic pressure and particle velocity, the prediction of transient sound propagation proceeds by discretizing the relationships spatially and temporally.

Discretization of the governing acoustic equations in space and time, by finite difference equations, is the first step in the FDTD technique. The following formulas apply for two-dimensional problems, which can be extended to three dimensions by including the third vector component of particle velocity. Pressure and particle velocity components are approximated as functions of discrete space and time (Redondo et al., 2007),

$$p_{l,m}^{n+1/2} = p(l\Delta x, m\Delta y, (n+1/2)\Delta t), \tag{2.33}$$

$$ux_{l+1/2,m}^{n} = \vec{u}((l+1/2)\Delta x, m\Delta y, n\Delta t) \cdot \hat{i}, \tag{2.34}$$

$$uy_{l,m+1/2}^{n} = \vec{u}(l\Delta x, (m+1/2)\Delta y, n\Delta t) \cdot \hat{j}, \tag{2.35}$$

where $\hat{i}$ and $\hat{j}$ are the Cartesian unit vectors, for the x and y coordinate axis respectively, ux is the x-component of the particle velocity, uy is the y-component of particle velocity, Δx and Δy are spatial steps in the x and y coordinate directions respectively, and Δt is the time step. In the function definitions for discretized pressure and particle velocities, the superscript, n, indicates the time index, and the subscript, l, m, indicates the spatial indices. The time and spatial indices are integers. Note, the pressure time indices are offset from the particle velocity indices by one half of a time step and the particle velocity spatial indices are offset by one half of a spatial subdivision. The reason for staggering the grids of each variable is to minimize the effect of higher order error terms inherent in each finite difference equation. Staggering the spatial and temporal grids is known as a leapfrog scheme (Cox and D'Antonio, 2009, p. 278).

The spatial and temporal derivatives of pressure and particle velocity are computed as central finite difference equations. For example, the derivative of pressure in the x-coordinate direction is given as,

$$p_x(x,y,t) \approx \frac{p(x+\Delta x, y, t+\Delta t/2) - p(x-\Delta x, y, t+\Delta t/2)}{2\Delta x} = \frac{p_{l,m}^{n+1/2} - p_{l-1,m}^{n+1/2}}{2\Delta x}, \tag{2.36}$$

where the p_x is shorthand for differentiation with respect to x ($p_x = \partial p/\partial x$), and the (x, y, t) argument corresponds to a particular node and time step, $(l\Delta x, m\Delta y, n\Delta t)$, in the Cartesian computation grid for a specific (l, m, n) pairing. Application of the central finite difference scheme to the acoustic pressure and particle velocities for spatial and temporal derivatives results in,

$$p_y(x,y,t) \approx \frac{p(x, y+\Delta y, t+\Delta t/2) - p(x, y-\Delta y, t+\Delta t/2)}{2\Delta y} = \frac{p_{l,m}^{n+1/2} - p_{l,m-1}^{n+1/2}}{2\Delta y}, \tag{2.37}$$

$$p_t(x,y,t) \approx \frac{p(x, y, t+3\Delta t/2) - p(x, y, t-\Delta t/2)}{2\Delta t} = \frac{p_{l,m}^{n+1/2} - p_{l,m}^{n-1/2}}{2\Delta t}, \tag{2.38}$$

$$ux_x(x,y,t) \approx \frac{ux(x+3\Delta x/2,y,t)-ux(x-\Delta x/2,y,t)}{2\Delta x} = \frac{ux^n_{l+1/2,m}-ux^n_{l-1/2,m}}{2\Delta x}, \tag{2.39}$$

$$uy_y(x,y,t) \approx \frac{uy(x,y+3\Delta y/2,t)-uy(x,y-\Delta y/2,t)}{2\Delta y} = \frac{uy^n_{l,m+1/2}-uy^n_{l,m-1/2}}{2\Delta y}, \tag{2.40}$$

$$ux_t(x,y,t) \approx \frac{ux(x,y,t+\Delta t)-ux(x,y,t-\Delta t)}{2\Delta t} = \frac{ux^{n+1}_{l+1/2,m}-ux^n_{l+1/2,m}}{2\Delta t}, \tag{2.41}$$

$$uy_t(x,y,t) \approx \frac{uy(x,y,t+\Delta t)-uy(x,y,t-\Delta t)}{2\Delta t} = \frac{uy^{n+1}_{l,m+1/2}-uy^n_{l,m+1/2}}{2\Delta t}. \tag{2.42}$$

Substitution of the finite difference equations, Eqs. (2.36)–(2.42) into the continuity equation, Eq. (2.32), and the equation of momentum, Eq. (2.4), gives the finite difference time domain equations,

$$p^{n+1/2}_{l,m} = p^{n-1/2}_{l,m} - B\Delta t\left(\frac{ux^n_{l+1/2,m}-ux^n_{l-1/2,m}}{\Delta x}+\frac{uy^n_{l,m+1/2}-uy^n_{l,m-1/2}}{\Delta y}\right), \tag{2.43}$$

$$ux^{n+1}_{l+1/2,m} = ux^n_{l+1/2,m} - \frac{\Delta t}{\rho_0}\left(\frac{p^{n+1/2}_{l+1,m}-p^{n+1/2}_{l,m}}{\Delta x}\right), \tag{2.44}$$

$$uy^{n+1}_{l,m+1/2} = uy^n_{l,m+1/2} - \frac{\Delta t}{\rho_0}\left(\frac{p^{n+1/2}_{l,m+1}-p^{n+1/2}_{l,m}}{\Delta y}\right). \tag{2.45}$$

First, the particle velocities are computed, based on past pressure values. After, the subsequent pressure values are computed. The computations continue in a leapfrog manner.

In order to ensure computational stability exists, the Courant-Friedrichs-Lewy condition (CFL condition) number, s, must be less than or equal to one,

$$s = c\Delta t\sqrt{\left(\frac{1}{\Delta x}\right)^2+\left(\frac{1}{\Delta y}\right)^2} \le 1. \tag{2.46}$$

To resolve wave propagation up to a specific frequency there must be ten spatial steps per the corresponding wavelength. Thus, if the maximum frequency of interest

is given then it is possible to find the required sampling frequency to fulfill the CFL criteria:

$$f_s \geq c\sqrt{\left(\frac{1}{\Delta x}\right)^2 + \left(\frac{1}{\Delta y}\right)^2}. \tag{2.47}$$

Since it is generally not possible to simulate far field wave propagation with the FDTD method directly, the contour equivalence theorem is utilized. The theorem states that the scattered pressure in the far field may be computed by integrating the scattered pressure, and particle velocity, in the near field along a contour which encloses the scattering object. Thus, at a far field position, $\vec{r}_f = (x_f, y_f)$, the scattered pressure is computed with the near-field scattered pressure and particle velocities along a bounding contour, Γ^+, which surrounds the domain Ω^+ (Hansen and Yaghjian, 1999, p. 66),

$$p(\vec{r}_f, t) = -\nabla \cdot \int_{\Gamma^+} \frac{\hat{n}p(\vec{r}, t - R/c)}{4\pi R}\, \mathrm{d}\Gamma^+ + \frac{\partial}{\partial t}\int_{\Gamma^+} \frac{\rho_0 \hat{n} \cdot u(\vec{r}, t - R/c)}{4\pi R}\, \mathrm{d}\Gamma^+, \tag{2.48}$$

where $R = |\vec{r} - \vec{r}_f|$. Transforming the above relation to the frequency domain gives a variant of the familiar Helmholtz-Kirchhoff integral (cf. Eq. (2.23)),

$$p(\vec{r}_f) = \int_{\Gamma^+} \left[p(\vec{r}\,') \frac{\partial G(\vec{r}_f; \vec{r}\,')}{\partial n'} - G(\vec{r}_f; \vec{r}\,') \frac{\partial p(\vec{r}\,')}{\partial n'} \right] \mathrm{d}\Gamma^+, \tag{2.49}$$

where the Green's function, $G(\vec{r}_f; \vec{r}\,')$, is defined as either Eq. (2.20) or Eq. (2.24).

In the context of predicting scattering of acoustic diffusors, one study is known that employs the FDTD method (Redondo et al., 2007). The predictions in the study agree well with BEM predictions (Cox and D'Antonio, 2011) for specular scattering angles. In contrast, a consistent difference is shown between the FDTD and BEM predictions for scattering angles far from the specular angle. The major appeal of the technique is the ability to compute transient scattering. Once the transient scattering characteristics are predicted, the spatial scattering

characteristics are evaluated in the frequency domain. Similar to the FEM the FDTD is computationally intensive. Both space and time are discretized according to Eqs. (2.43)–(2.45). Thus, the dimensionality of the problem is usually restricted to a two-dimensional domain, as in the referenced study. Acoustic diffusors which exhibit scattering characteristics in more than one plane suggests a need for a three-dimensional prediction.

2.5 Boss Theory

Rough surface scattering is closely related to acoustic diffusor scattering. The scattering induced by a rough surface includes coherent scattering by periodic roughness and incoherent scattering by random roughness. Consideration of either one or both effects have resulted in various models on the effective surface admittance for hemispherical bosses (Biot, 1957) and cylindrical bosses (Lucas and Twersky, 1984). The theory in the cited studies apply for continuous-wave scattering. In what follows the theory developed by Lucas and heuristically extended by Boulanger et al. (1998) are considered.

Consider a plane situated in the xy-plane with cylindrical bosses oriented parallel to the y-axis. The cylindrical bosses have a radius a and a mean center-to-center spacing b. An incident plane wave has a propagating vector pointing towards the origin. The reverse of the propagating vector has an azimuth angle θ and polar angle ϕ. The effective surface admittance is (Lucas and Twersky, 1984),

$$\zeta(\theta, \phi) = \chi(\theta, \phi) + j\xi(\theta, \phi), \tag{2.50}$$

where ζ is the effective surface admittance, χ is the real part of the surface admittance due to incoherent scattering, and ξ is the imaginary part of the surface admittance due to coherent scattering. The real and imaginary parts of the effective

surface admittance are defined as,

$$\chi(\theta,\phi) = \frac{k^3V^2}{2n}(1-W^2)\{[1-\sin^2(\theta)\sin^2(\phi)] \times [1+(\delta^2\cos^2(\theta)/2-\sin^2(\theta))\sin^2(\phi)]\}, \tag{2.51}$$

$$\xi(\theta,\phi) = kV[-1+(\delta\cos^2(\theta)+\sin^2(\theta))\sin^2(\phi)], \tag{2.52}$$

where V is the raised cross-sectional area per unit length (in the case of a semicylinder $V = n\pi a^2/2$, $n = 1/b$ is the number of bosses per unit length). The term $(1-W^2)$ is a packing factor, which is identically equal to zero for periodic bosses, otherwise it is between zero and one for $W = nb^*$, where b^* is the minimum separation between bosses. The δ term indicates the dipole-coupling between bosses (Boulanger et al., 1998),

$$\delta = \frac{1+K}{1+I[K(1+K)/2]}, \tag{2.53}$$

where K is a hydrodynamic factor based on the boss shape ($K = 1$ for a semicylinder), and $I = (\pi a)^2/(3b^2)$ for periodic bosses. Additional expressions for non-periodic boss arrangements are given by Lucas and Twersky (1984), and hydrodynamic factors by Boulanger et al. (1998).

A heuristic extension of Twersky's boss model accounts for the diffraction grating effect of periodic roughness. First, the total pressure field is considered for a homogeneous impedance plane (Boulanger et al., 1998),

$$p(\vec{r}) = p_1(\vec{r}) + p_2(\vec{r}) = A\frac{e^{-jkR_1}}{R_1} + AQ\frac{e^{-jkR_2}}{R_2}, \tag{2.54}$$

where A is a constant, R_1 is the distance from the source to receiver, and R_2 is the distance from the image source to receiver. The first term on the right of Eq. (2.54), p_1, corresponds to the direct wave and the second term corresponds to the ground reflection. The Q term in Eq. (2.54) is the spherical wave reflection coefficient

(Attenborough et al., 2007, p. 417),

$$Q(R_2, \phi, \zeta) = R_p(\phi, \zeta) + [1 - R_p(\phi, \zeta)]F, \tag{2.55}$$

where ϕ is the polar angle of incidence, and R_p is the plane wave reflection coefficient,

$$R_p(\phi, \zeta) = \frac{\cos(\phi) - \zeta}{\cos(\phi) + \zeta}. \tag{2.56}$$

The F term is defined as,

$$F(w) = 1 - j\sqrt{\pi} w e^{-w^2} \text{erfc}(jw), \tag{2.57}$$

where erfc() is the complex error function (Weideman, 1994), and w is the numerical distance,

$$w = \sqrt{-jkR_2/2}[\cos(\phi) + \zeta]. \tag{2.58}$$

The grating effect is hypothesized to be a reflected wave originating from an image source with an extra path length,

$$p'(\vec{r}) = A\frac{e^{-jk(R_2+\Delta)}}{(R_2 + \Delta)}, \tag{2.59}$$

where $\Delta = qb\sin(\phi)$, and q is an integer depending on the order of interference. The total pressure field taking into account the diffraction grating effect is,

$$p_d(\vec{r}) = w_r p(\vec{r}) + (1 - w_r)(p_1(\vec{r}) + p'(\vec{r})), \tag{2.60}$$

where w_r is the ratio of area covered by bosses. Note, Eq. (2.60) corrects a typographic error in Eq. (16) of (Boulanger et al., 1998).

Specific studies on predicting acoustic diffusor scattering by boss theory are nonexistent. The major difficulty in applying boss theory to diffusor prediction is

the limited geometric applicability. Often, acoustic diffusors are designed as notched surfaces with varying depths or as curved surfaces. It is not clear how boss theory may address the vast majority of number theoretic diffusors. Furthermore, the inherent assumptions of the spherical wave reflection coefficient constrains the source and receiver to positions close to the surface, large separations relative to the wavelength, and is only valid for high frequencies. However, it is conceivable that boss theory may be applied to predicting acoustic scattering by geometric diffusors. Notwithstanding the narrow range of applicability, the theory agrees well with experimental results (Bashir et al., 2013).

2.6 Edge Diffraction Theory

Edge diffraction is a form of acoustic scattering. Sound incident upon a wedge or knife edge scatters sound into all directions creating a continuous sound field across the direct and reflected geometric boundaries; see Fig. 2.2. The exclusion of acoustic diffraction in many cases leads to incorrect predictions of the sound field. Thus, acoustic diffraction forms a vital component of many computed sound fields.

The omission of acoustic diffraction by several traditional propagation prediction methods presents an opportunity to extend the frequency range of geometric methods such as the image source method, ray tracing, or beam tracing. Acoustic diffraction is vitally important for scattering geometries, especially acoustic diffusors. The scattered sound field of a rigid diffusor consists of reflected and diffracted sound fields. The mutual scattering across the surface and edges of a diffusor are completely omitted by geometric propagation methods. Thus, the inclusion of diffraction is necessary to model the sound field correctly.

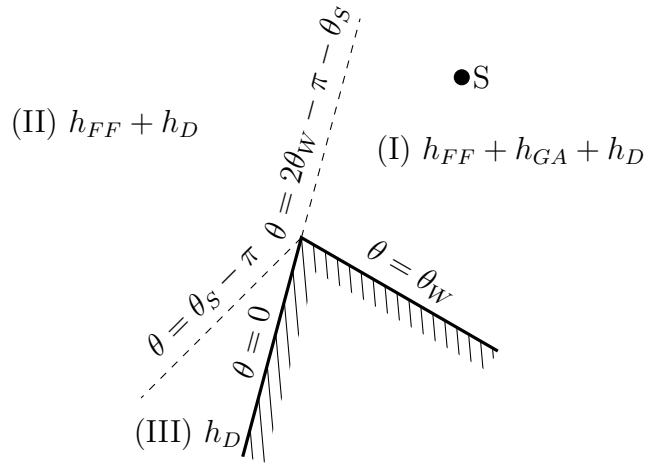

Figure 2.2: Geometric boundaries for a diffracting wedge delineate the extent of free-field radiation and geometric acoustic propagation. The angle $\theta_S - \pi$ demarcates the shadow boundary beyond which no free-field radiation is present. The angle $2\theta_W - \pi - \theta_S$ demarcates the geometric boundary beyond which no geometric propagation is present. Three regions are defined by the geometric boundaries for the wedge geometry shown. Region (I) contains the sum of free-field radiation, geometric propagation, and diffraction. Region (II) only contains free-field radiation, and diffraction. Lastly, region (III) only contains diffraction. After (Pierce, 1974).

2.6.1 Classical Solutions of Infinite Plane/Wedge Diffraction

Acoustic diffraction by wedges is a well studied problem, tracing back to work conducted in the nineteenth century. The solution of plane wave acoustic diffraction from a rigid screen is due to Sommerfeld (2004). The solution to diffraction by a wedge was eventually generalized for a wedge of any angle (Carslaw, 1920). Acoustic diffraction by a point source, incident upon a wedge of any angle, was solved by MacDonald (1915). The solution of point source diffraction was later extended to any arbitrary source type (Bromwich, 1915). The handbook solutions for screen and wedge diffraction are based on the above developments (Bowman et al., 1987, chs. 6 and 8). All of the solutions mentioned are for time-harmonic sources. In contrast, the development of transient solutions of acoustic diffraction followed time-harmonic solutions by several decades.

Transient solutions of acoustic diffraction originated with the landmark study by Biot and Tolstoy (1957). A normal coordinates approach was employed for the solution of transient acoustic diffraction by an infinite rigid wedge. Figure 2.3 illustrates the geometry and cylindrical coordinate system of the problem. The original solution assumed a doublet source and was modified to account for a point source (Medwin, 1981). The expressions by Medwin (1981), and Kinney et al. (Kinney et al., 1983) are combined to express the transient scattering of an infinite wedge (Svensson et al., 1999),

$$h_d(\tau) = -\frac{c\nu}{2\pi} \frac{\beta(\tau)}{r_S r_R \sinh \eta(\tau)} H(\tau - \tau_0), \tag{2.61}$$

where

$$\beta(\tau) = \beta_{++}(\tau) + \beta_{+-}(\tau) + \beta_{-+}(\tau) + \beta_{--}(\tau), \tag{2.62}$$

$$\beta_{\pm\pm}(\tau) = \frac{\sin[\nu(\pi \pm \theta_S \pm \theta_R)]}{\cosh[\nu\eta(\tau)] - \cos[\nu(\pi \pm \theta_S \pm \theta_R)]}, \tag{2.63}$$

$$\eta(\tau) = \cosh^{-1}\left[\frac{c^2\tau^2 - (r_S^2 + r_R^2 + (z_R - z_S)^2)}{2r_S r_R}\right], \tag{2.64}$$

where h_d is the first-order diffraction impulse response, $\nu = \pi/\theta_w$ is the wedge index, θ_w is the exterior wedge angle, $H(\tau - \tau_0)$ is the Heaviside step function, and τ_0 is the onset time of diffraction for the least time path L_0. The cylindrical coordinates of the source and receiver are (r_S, θ_S, z_S), and (r_R, θ_R, z_R), respectively; see Figs. 2.2 and 2.3. The least time path L_0 is the distance from source, to wedge apex, to receiver given as $L_0 = [(r_S + r_R)^2 + (z_R - z_S)^2]^{1/2}$. The distance is the shortest diffraction path for a wedge.

The closed form solution for transient wedge diffraction, by Biot and Tolstoy, does not immediately suggest how to compute multiple order diffraction nor diffraction for finite wedges (Svensson et al., 1999). However, a reinterpretation of acoustic diffraction according to Huygens principle does suggest how to generalize

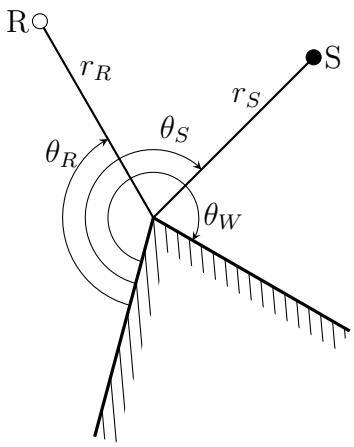

Figure 2.3: Acoustic diffraction geometry for an infinite rigid wedge. The z-axis of the cylindrical coordinate system is aligned with the diffracting wedge, and pointing into the page. Azimuth angles indicate the angular position of the source (θ_S), receiver (θ_R), and open wedge angle (θ_W). The radial distances of the source to edge and receiver to edge are denoted by r_S, and r_R, respectively. The z-coordinates (not shown) of the source and receiver are z_S, and z_R, respectively.

acoustic diffraction to more complex scenarios. This interpretation was shown to be fruitful for computing the diffraction of finite wedges (Medwin, 1981), and doubly diffracting wedges (Medwin et al., 1982). In contrast to interpreting acoustic diffraction as propagating modes, the application of Huygens principle interprets acoustic diffraction as the radiation of secondary sources along a wedge. This reinterpretation laid the ground work for specifying more precisely the directivity function of theoretical secondary sources.

2.6.2 Secondary Source Model for Finite Edge Diffraction

The basis for the secondary source model for edge diffraction begins by computing the impulse response according to Kirchhoff's retarded potential method (Berryhill, 1977). The pressure response for wedge diffraction is considered as a convolution between a source signal and diffraction impulse response (Svensson et al., 1999,

Eq. (12)),

$$\begin{aligned} p_d(t) &= q(t) * h_d(t) \\ &= \int_{-\infty}^{\infty} q(t-\tau) h_d(\tau)\, \mathrm{d}\tau, \end{aligned} \tag{2.65}$$

where $p_d(t)$ is the diffracted pressure, $q(t)$ is the source signal, and $h_d(t)$ is the diffraction impulse response. The initial derivation by Berryhill (1977) considers a collocated source and receiver, and the special case of a knife edge ($\theta_W = 2\pi$). A non-collocated source and receiver position are then considered, which are arranged either perpendicularly or parallel to the diffracting edge. The diffraction integral is computed as an area integration in the spatial domain. Later, the analysis is extended and reinterpreted by Svensson et al. (1999). The starting point of the analysis is an infinite wedge, with arbitrary wedge angle, arbitrary source position, and arbitrary receiver position. Eq. (2.65) is cast as a convolution between the source signal and an unknown directivity function, attenuated by the path lengths from source to edge and edge to receiver (Svensson et al., 1999, Eq. (9))),

$$p_d(t) = \int_{-\infty}^{\infty} q\left[t - \frac{m(z) + l(z)}{c}\right] \frac{D[\alpha(z), \gamma(z), \theta_S, \theta_R]}{m(z) l(z)}\, \mathrm{d}z, \tag{2.66}$$

where m and l are path lengths from source to edge and edge to receiver, respectively, and the projected angles for path lengths m and l are α and γ, respectively; see Figs. 2.3 and 2.4. The key difference in the integral is that a line integral is being formulated as opposed to an area integral. Conversion of the line integral to a integration in time results in (Svensson et al., 1999, Eq. (11)),

$$p_d(t) = \int_{-\infty}^{\infty} q(t-\tau) \frac{D[\alpha(\tau), \gamma(\tau), \theta_S, \theta_R]}{m(\tau) l(\tau)} \frac{\mathrm{d}z}{\mathrm{d}\tau}\, \mathrm{d}\tau, \tag{2.67}$$

where $\tau = (m(z) + l(z))/c$. By mathematical analysis it is shown that the unknown directivity function is related to Eq. (2.62) (Svensson et al., 1999, Eq. (18)),

$$D[\alpha(\tau), \gamma(\tau), \theta_S, \theta_R] = -\frac{\nu}{4\pi}\beta[\alpha(\tau), \gamma(\tau), \theta_S, \theta_R]. \tag{2.68}$$

Substitution of Eq. (2.68) into Eq. (2.67) results in the diffracted impulse response (Svensson et al., 1999, Eq. (19)),

$$h_d(\tau) = -\frac{\nu}{4\pi}\frac{\beta[\alpha(\tau), \gamma(\tau), \theta_S, \theta_R]}{m(\tau)l(\tau)}\frac{\mathrm{d}z}{\mathrm{d}\tau}, \tag{2.69}$$

where β is defined as Eq. (2.62) and Eq. (2.63), and η is defined as (Svensson et al., 1999, Eq. (16)),

$$\eta(\tau) = \cosh^{-1}\left[\frac{1 + \sin\alpha(\tau)\sin\gamma(\tau)}{\cos\alpha(\tau)\cos\gamma(\tau)}\right]. \tag{2.70}$$

Note, Eq. (2.69) is the continuous-time expression for finite wedge diffraction. Solution of the diffraction impulse response is based on a line integral along the diffracting edge. Parameters derived for the Biot and Tolstoy solution are determined to satisfy the unknown directivity function. The second order diffraction impulse response, for a truncated wedge, is derived following the same procedure of retarded potentials. It is shown the second order diffracted impulse response is a scaled first order diffraction impulse from the secondary sources along the first edge to the receiver, via the second edge. The scaling is based on a sum of directivity functions with respect to the first and second edge (Svensson et al., 1999, Fig. (4) and Eq. (27)).

2.6.3 Solution of Diffraction Singularities

The closed form solutions for diffraction impulse responses contain two types of singularities. The first singularity occurs at the onset time of diffraction, τ_0. It is

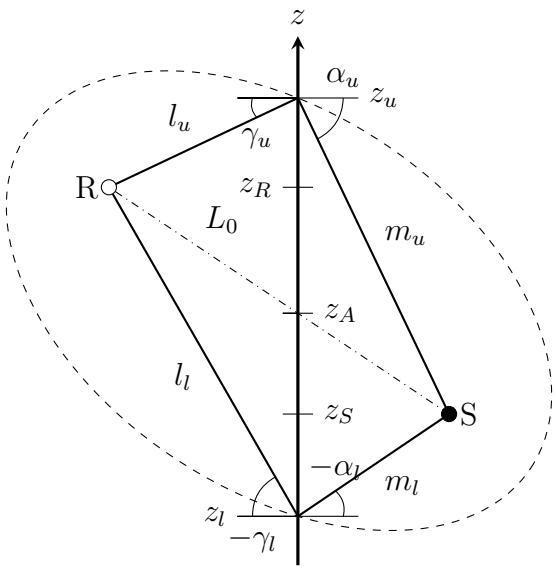

Figure 2.4: Unfolded diffraction geometry. Two diffracting paths of propagation exist for an infinite wedge. Upper and lower paths, denoted by subscript u and l, are of the same length. The path lengths correspond to confocal ellipses with foci at the source and receiver. The shortest path length, L_0, passes through the wedge apex, z_A. Projected angles of the path lengths, with respect to the edge, are parameters for the directivity function in Eq. (2.68). After (Svensson et al., 1999).

present for all source and receiver positions. The expression for diffraction in Eq. (2.69) becomes infinite when the travel time, $\tau = \tau_0$, corresponds to the least time path L_0. The reason for the singularity is due to the term $\mathrm{d}z/\,\mathrm{d}\tau$. This term inherently contains $\sinh(\nu)^{-1}$ (Svensson et al., 1999, Eq. (14)) in the denominator, which becomes infinite for the least time path (when τ corresponds to the least time path then ν is zero, resulting in $\sinh(\nu) = 0$). This singularity is suppressed by transforming the continuous-time expression to a discrete-time expression and applying a low-pass filter (Clay and Kinney, 1988). One form of the low-pass filtered discrete-time diffraction impulse response is (Svensson et al., 1999, Eq. (30)),

$$h_d[n] = \int_{(n-1/2)/f_s}^{(n+1/2)/f_s} h_d(\tau)\,\mathrm{d}\tau \tag{2.71}$$

where n is the discrete sample number, $\tau = n/f_s$ is the travel time corresponding to discrete sample number n, and $h_d(\tau)$ is the continuous-time diffraction impulse

response as in Eq. (2.69). The integration effectively acts as a low-pass filter. To decrease the attenuation by low-pass filtering, it was suggested to integrate over a time window of $4/f_s$ (Clay and Kinney, 1988); however, increasing the sampling frequency achieves a similar reduction in attenuation. The second singularity arises when the receiver is along a geometric acoustic boundary at the onset time of diffraction. Two geometric boundaries exist: the shadow boundary and reflection boundary; see Fig. 2.2. When the receiver is located on the shadow boundary or reflection boundary, the expression for β becomes infinite. The term $\cosh[\nu\eta(\tau)]$ is equal to one at the onset time of diffraction. For a receiver on a geometric boundary the term $\cos[\nu(\pi \pm \theta_S \pm \theta_R)$ is equal to one. Thus, the denominator of β is zero at the onset time of diffraction for a receiver on a geometric boundary; see Eqs. (2.63) and (2.64). This singularity exists in order to account for the discontinuity of the geometric acoustic field. An analytic approximation, which suppresses the singularity, bounds the diffraction impulse response (Svensson and Calamia, 2006). The form of the approximation is,

$$\frac{\beta[\alpha(z), \gamma(z), \theta_S, \theta_R]}{m(z)l(z)} \approx \frac{B_0}{(z_{rel}^2 + B_1)(z_{rel}^2 + B_2 z_{rel} + B_3)}, \tag{2.72}$$

where $z_{rel} = z - z_A$ is the z-coordinate relative to the wedge apex, see Fig. 2.4. The variables B_0 through B_4 are defined as,

$$\begin{aligned}
B_0 &= \frac{4L_0^2\rho^3 \sin[\nu(\pi \pm \theta_S \pm \theta_R)]}{\nu^2(1+\rho^4)[(1+\rho)^2\sin^2\psi - 2\rho]}, \\
B_1 &= \frac{4L_0^2\rho^2 \sin^2[\nu(\pi \pm \theta_S \pm \theta_R)/2]}{\nu^2(1+\rho)^4}, \\
B_2 &= -\frac{2L_0(1-\rho)\rho\cos\psi}{(1+\rho)[(1+\rho)^2\sin^2\psi - 2\rho]}, \\
B_3 &= \frac{2L_0^2\rho^2}{(1+\rho)^2[(1+\rho)^2\sin^2\psi - 2\rho]}.
\end{aligned} \tag{2.73}$$

The dimensionless variable $\rho = r_R/r_S$ is the ratio of radial receiver distance and source distance, and ψ is the projected angle of the least time path with the wedge defined implicitly as,

$$\tan\psi = \frac{r_S + r_R}{z_R - z_S}. \tag{2.74}$$

The approximation in Eq. (2.72) facilitates the numerical computation of wedge diffraction when either the receiver is on the reflection or shadow boundaries and the time sample closely corresponds to the onset time of diffraction. Special care is required for the exact limits of integration over the time sample corresponding to the onset of diffraction (cf. Eq. (2.71)). The simplest case requires the upper limit of integration to be the extent of the first sample. Other considerations are provided in (Svensson and Calamia, 2006).

2.6.4 Discrete-time Diffraction Formulation

Numerical computation of first, second, and higher order diffraction are achieved by numerically integrating the continuous-time impulse response, as in Eq. (2.71). Transformation of the variable of integration, in Eq. (2.71), from time to a differential element along the wedge allows the integration to be conducted as a line integral. Distinct diffraction contributions are approximated by the midpoint of two coordinates corresponding to the starting and ending times for one time sample. For example, first order diffraction is determined by a simple midpoint approximation to the integral of the continuous-time impulse response as (Svensson et al., 1999, Eq. (34)),

$$h_d(n) \approx -\frac{\nu}{4\pi}\frac{\beta[\alpha(z_n), \gamma(z_n), \theta_S, \theta_R]}{m(z_n)l(z_n)}\Delta z_n, \tag{2.75}$$

where z_n is the midpoint coordinate of z_{n2} and z_{n1}, which corresponds to discrete times $\tau = (n \pm 1/2)/(f_s)$, and Δz_n is the edge element width $(z_{n2} - z_{n1})$. Setting the length of each edge element width to a constant, Δz, results in determining the i^{th}

diffraction contribution from element i,

$$\Delta h_{d,i} = -\frac{\nu}{4\pi}\frac{\beta[\alpha(z_i), \gamma(z_i), \theta_S, \theta_R]}{m(z_i)l(z_i)}\Delta z, \tag{2.76}$$

where the i^{th} contribution should be added to the time sample, $n = f_s(m(z_i) + l(z_i))/c$, or subdivided between two time samples. Setting the edge element width to $\Delta z < c/f_s$ results in the diffraction contribution spreading over no more than two time samples. Extension to second and third order diffraction is formulated similarly to Eq. (2.76), except contributions of second order diffraction must take into account each distinct combination of secondary source along each edge. For example, the second order diffraction contribution from the i^{th} edge element at z_i, for the first diffracting edge, along the j^{th} edge element at z_j, for the second diffracting edge, is computed as,

$$\Delta h_{d,ij} = \frac{\nu_1\nu_2}{32\pi^2}\frac{\beta[\alpha_1(z_i), \gamma_1(z_i, z_j), \theta_{S1}, \theta_{R1}]\beta[\alpha_2(z_i, z_j), \gamma_2(z_j), \theta_{S2}, \theta_{R2}]}{m_1(z_i)m_2(z_i, z_j)l_2(z_j)}\Delta z_1 \Delta z_2, \tag{2.77}$$

where the subscript 1 denotes the first diffracting edge, subscript 2 denotes the second diffracting edge, and the respective edge element lengths are Δz_1 and Δz_2. Furthermore, the $32\pi^2$ term is valid for two edges connected by a plane and accounts for the doubling of pressure for a source mounted on an infinite baffle. Otherwise, the term should be written as $16\pi^2$ when no plane connects the two edges.

Combinations of geometric reflection and diffraction are based on the computation of both image sources and image receivers. Calculating edge diffraction due to an image source via Eq. (2.76) or Eq. (2.77) takes into account geometric reflections prior to diffraction. Similarly, calculating edge diffraction for an image receiver accounts for geometric reflections following diffraction (Torres et al., 2001).

In the context of predicting scattering by acoustic diffusors, no known studies exist which utilize an edge diffraction model. The closest related studies are on

surface roughness (Kinney et al., 1983; Novarini and Medwin, 1985). Possible reasons for the lack of studies include the limited geometric generality, the increasing complexity of higher-order diffraction, and an incompatibility with most geometric propagation methods. In spite of the limited geometric generality of edge diffraction models the wedge shape was shown to approximate a sinusoidal surface fairly well (Novarini and Medwin, 1985). A second difficulty is the computational bottleneck for computing higher orders of diffraction. Consider two edges, with the same length, that are subdivided into N edge elements. For second-order diffraction N^2 diffraction contributions must be computed. A potential solution to this difficulty is an integral equation formulation for higher-order diffraction (Asheim and Svensson, 2013). Another challenge for edge diffraction models are the present incompatibilities with most geometric propagation models. Studies on edge diffraction using image sources (Torres et al., 2001) or ray tracing (Antani et al., 2012) demonstrate an inherent incompatibility between the two models. It is suggested that adaptive beam tracing is a compatible technique, which is considered in Chapter 4.

2.7 Summary

The theoretical foundations for scattering prediction methods are discussed at length for wave-based methods, and analytic models. Wave-based methods, especially the BEM, have found widespread use in the prediction of acoustic diffusor scattering. The future trend is to compute the transient scattering characteristics with either the time-domain BEM or FDTD. Alternatively, analytic models offer the potential for faster computations at the expense of geometric generality. For example the dimensionality of edge scattering is reduced to a line integral as opposed to a surface or volume integration. The potential for computing transient scattering by

edge diffraction and adaptive beam tracing is explored in Chapters 4 and 5.

Chapter 3

Adaptive Tetrahedral Tracing

Adaptive tetrahedral tracing is an advanced image source method. As a geometric propagation method it shares many similarities with other techniques such as the image source method (Allen and Berkley, 1979), ray tracing (Kulowski, 1985), and classical beam tracing (Lewers, 1993). However, several features distinguish the method from those mentioned previously. The primary distinction is the conceptual view of sound propagation: free-field radiation of sound is a set of expanding tetrahedrons and geometric reflection is a larger set of expanding tetrahedral frustums. The initial set of tetrahedrons generally increases upon reflection due to tetrahedral subdivision. For example, as an initial tetrahedron expands in volume, intersecting with the geometric domain, portions of the tetrahedron split according to the incident geometry. Being most closely related to adaptive beam tracing (Campo et al., 2000; Drumm and Lam, 2000; Stephenson, 1996) the adaptive tetrahedral algorithm presented in this chapter expands upon previous work by defining the algorithm as clearly as possible and proposing alternative strategies when appropriate.

This chapter details the adaptive tetrahedral tracing algorithm. Section 3.1 presents related past work on beam tracing for acoustics, including non-adaptive and

adaptive techniques. Theoretical and algorithmic details of the adaptive tetrahedral tracing method are given in Section 3.2, and a summary is given in Section 3.3.

3.1 Prior Work

Beam tracing first developed as a method for computer graphics applications (Heckbert and Hanrahan, 1984; Dadoun et al., 1985). The geometric coherence of beam tracing was found to be a superior method for generating computer images as opposed to ray tracing. In the context of computer graphics, geometric coherence is the conceptual treatment of continuous light propagation as opposed to discrete light propagation, as in ray tracing. For example, a propagating beam may be thought of as an infinite bundle of rays as opposed to discrete rays. Applications of beam tracing to acoustic modeling started emerging in the following decades. A number of different beam tracing models have been developed that are both non-adaptive and adaptive.

A non-adaptive beam tracing model was combined with a radiant exchange model to simulate the decay response of a space (Lewers, 1993). The non-adaptive beam tracing algorithm developed by Lewers was supplemented by a radiant exchange model in order to predict the late energy decay within a space. Another implementation examined the effect of multilayer boundaries within an enclosure (Wareing and Hodgson, 2005). More recently a non-adaptive beam tracing model was applied to study the effects of modeling enclosure boundaries as either an impedance boundary or an energy absorption boundary (Jeong, 2012).

The first study on adaptive beam tracing outlined a rough algorithmic description (Stephenson, 1996). However, no results based on the algorithm were provided in the study. An adaptive beam tracing model combined with binary space partitioning was developed for real-time auralization purposes (Funkhouser et al.,

2004). This implementation is distinguished from non-adaptive beam tracing models by including a model for diffraction: the uniform theory of diffraction (UTD) (Kouyoumjian and Pathak, 1974). Another adaptive beam tracing model approximates the reflection of propagating beams by omitting portions of the incident beam after beam subdivision, which is supposedly balanced by distributing the acoustic energy across the reflected beams (Campo et al., 2000). In the study by Campo et al. (2000) diffraction is treated by Maekawa's noise barrier model (Maekawa, 1968) for room acoustic predictions. Lastly, an adaptive beam tracing model was combined with a radiosity method for the purpose of computing the energy decay of rooms (Drumm and Lam, 2000). Unlike other adaptive beam tracing models the study by Drumm and Lam (2000) omits diffraction effects.

There are several inherent drawbacks for classical beam tracing algorithms. First, the reliance upon a central vector for determining the propagation paths of a beam does not account for a beam incident upon two or more polygons (Campo et al., 2000). As a result specular paths of propagation are incorrectly detected or missed leading to an incorrect computation of the geometric acoustic field; see Fig. 3.1(a). In a related manner ray tracing results in acoustic aliasing since the domain is spatially sampled by a finite number of rays (Lehnert, 1993). The solution for this first issue is to clip or subdivide beams that intersect multiple polygons (Drumm and Lam, 2000). A second drawback inherent in both classical and adaptive beam tracing is a second form of acoustic aliasing, which occurs when the cross-section of a propagating beam becomes larger than a polygon; see Fig. 3.1(b). A simple approach to resolve the second issue is to refine the initial beam density. Lastly, accounting for acoustic diffraction in classical beam tracing is beset by the same difficulties associated with ray tracing. Typically, a ray does not exactly intersect a diffracting edge, so edge detection becomes a difficulty. Heuristic extensions of diffraction formulas based on quantum mechanics and the use of edge

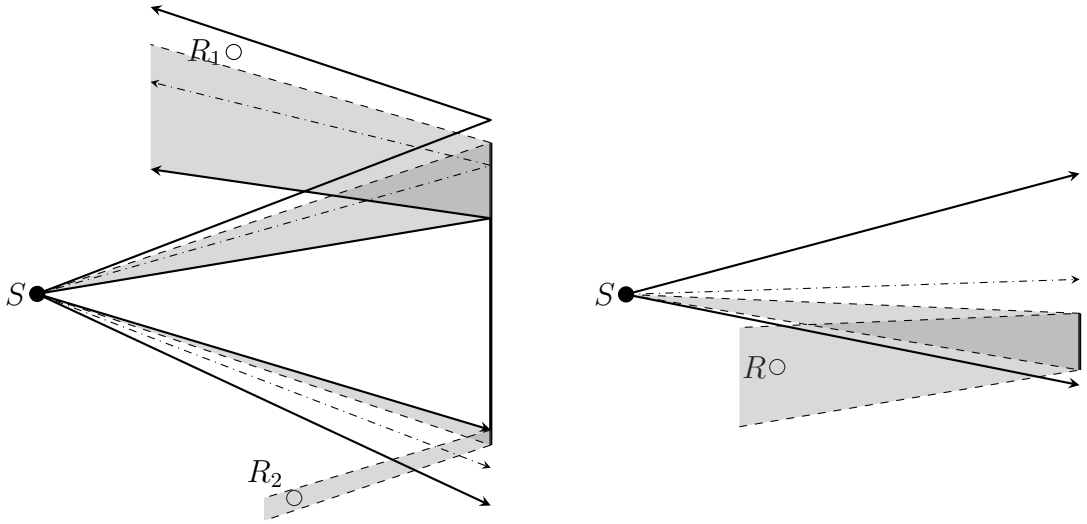

Figure 3.1: Acoustic aliasing for classical and adaptive beam tracing. (a) For classical beam tracing a reliance upon a central ray (dash-dotted ray) for reflection computations lead to incorrect receiver detection, as for R_1, and missed receiver detection, as for R_2. The gray regions denote the correct reflected regions. After (Campo et al., 2000). (b) Both classical and adaptive beam tracing are prone to acoustic aliasing for beams that become larger than a geometric surface. In this case a specular reflection to receiver R is missed.

flags provide a possible solution, but severe limitations are imposed by such an approach (Stephenson, 2008, 2010a,b). Specific limitations include restrictions to two-dimensional geometry, and ambiguous cases of identifying edge diffraction.

3.2 Adaptive Tetrahedral Tracing Algorithm

Conceptually the adaptive tetrahedral tracing algorithm is an exact image source method. Only valid image sources are created through the propagation of polygonal beams. Tetrahedral beams are utilized since cone-shaped beams result in overlapping errors (Funkhouser et al., 2004). The algorithm described in this chapter builds upon many elements from classical beam tracing and past models of adaptive beam tracing. In brief, the adaptive tetrahedral tracing algorithm begins by propagating initial beams throughout the geometric domain. Beams adapt to

occluding geometry through beam clipping operations. Ray tracing techniques are utilized for beam clipping (Drumm and Lam, 2000). For sufficiently complex geometry beam clipping may operate recursively. Geometric details are resolved by the recursive process resulting in subdivided beam mappings of all ensonified regions. Clipped beam profiles, which are not triangular, are subdivided into triangular regions by a constrained Delaunay triangulation (Yvinec, 2013). Finally, the image source location corresponding to each subdivided triangular beam profile is calculated and new tetrahedral beams are reflected throughout the domain.

3.2.1 Surface Geometry

The surface geometry is defined within a Cartesian coordinate system. Polygons are geometric elements that compose the geometric domain. In this study each polygon is a quadrilateral with four vertices, $\vec{v}_1$ to $\vec{v}_4$, and four edge vectors, $\vec{e}_1$ to $\vec{e}_4$, see Fig. 3.2. A vertex is defined as a three-dimensional coordinate, eg. $\vec{v}_1 = (x_1, y_1, z_1)$. Each edge vector is defined as (O'Rourke, 1998, p. 1),

$$\vec{e}_i = \vec{v}_{i \bmod 4+1} - \vec{v}_i \quad \text{for} \quad i = 1, 2, 3, 4, \tag{3.1}$$

where mod is the modulus operator. In the composition of a geometric domain hanging vertices are disallowed, or equivalently adjacent polygons only share common vertices. A hanging vertex is a vertex of a polygon that lies on the edge of another polygon. The unit normal of a polygon is defined as,

$$\hat{n} = \frac{\vec{e}_1 \times \vec{e}_2}{|\vec{e}_1 \times \vec{e}_2|}, \tag{3.2}$$

where $\hat{n}$ is the unit normal, the operator $\times$ is the cross product, and $|\cdot|$ is the norm of the vector. A polygon unit normal is oriented such that the normal points away from the "front" of a polygon. Each polygon is associated with a plane that is

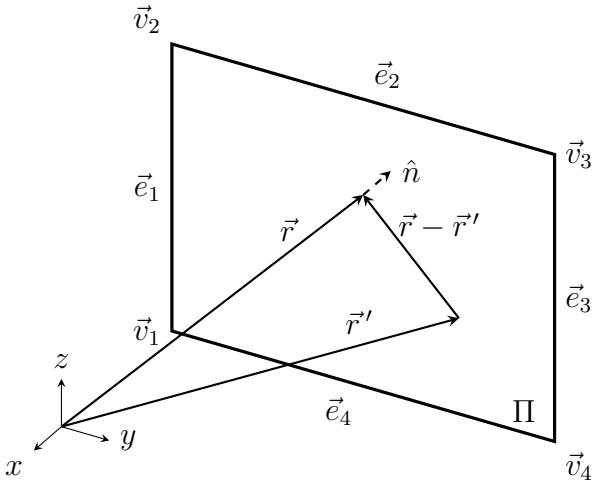

Figure 3.2: Geometric definitions for a polygon. The polygon, Π, is associated with a plane. The position vector $\vec{r}'$ is a known point on the plane and all points on the plane, $\vec{r}$, satisfy Eq. (3.3). The polygon is defined by four vertices, $\vec{v}_1$ to $\vec{v}_4$, and four edge vectors, $\vec{e}_1$ to $\vec{e}_4$. The direction of the polygon unit normal, $\hat{n}$ is governed by the right-hand rule, applied to the cyclic ordering of vertices.

mathematically defined as (Long, 2006, p. 789),

$$\hat{n} \cdot (\vec{r} - \vec{r}') = 0, \tag{3.3}$$

where the operator $\cdot$ is the dot product of two vectors, $\vec{r}'$ is the position vector of a known point on the plane, and $\vec{r}$ is a position vector to points in the plane associated with the polygon Π. Equation (3.3) concisely defines all the points on the plane associated with the polygon Π. The equation stipulates that the dot product between the plane unit normal, $\hat{n}$, and the vector $\vec{r} - \vec{r}'$ must be identically zero for $\vec{r}$ corresponding to points in the plane, see Fig. 3.2.

Expansion of Eq. (3.3) results in another form for the plane equation,

$$n_x(x - x') + n_y(y - y') + n_z(z - z') = 0, \tag{3.4}$$

where the unit normal is defined in terms of Cartesian components, $\hat{n} = n_x\hat{i} + n_y\hat{j} + n_z\hat{k}$, and similarly for the position vectors. Algebraic rearrangement of Eq. (3.4) results in an alternative plane equation,

$$ax + by + cz + d = 0, \tag{3.5}$$

where a, b, and c are the respective vector components of the unit normal vector $\hat{n}$. The perpendicular distance from the plane to the origin is given as $d = -\hat{n} \cdot \vec{r}'$.

In order to facilitate the storage of geometric information, matrices are utilized. A vertex matrix stores each unique vertex in a K by three matrix where K is the total number of vertices and each column corresponds to a Cartesian coordinate. Polygons are specified as a combination of four vertex references in a L by four matrix where L is the total number of polygons and each entry is a vertex reference to the corresponding row in the vertices matrix. Vertices are ordered according to the right hand rule, which dictates the direction of the polygon unit normal. The polygons at the boundaries of the domain have outward pointing normals. Polygon unit normals are in a L by three matrix with each column corresponding to a component of the normal. All the edge vectors are stored in a $4L$ by four matrix. Each row corresponds to a particular edge vector. The first column references a specific polygon and the last three columns are the edge vector components. Lastly, every polygon is defined as either acoustically rigid or anechoic in a column vector with length L. Acoustically rigid polygons are associated with a numerical value of zero and anechoic polygons are associated with a numerical value of one.

3.2.2 Omnidirectional Source

An icosahedron is a geometric primitive that has found common use in beam tracing for modeling an omnidirectional source. The vertices of an icosahedron,

centered at the origin, are defined as (Drumm and Lam, 2000),

$$\begin{aligned}(0, \pm 1, \pm\tau),\\ (\pm 1, \pm\tau, 0),\\ (\pm\tau, 0, \pm 1),\end{aligned} \tag{3.6}$$

where $\tau = (1 + \sqrt{5})/2$ is the golden ratio; see Fig. 3.3(a). The vertices of the icosahedron are normalized to the unit sphere and serve as unit vectors for beam rays; see Eq. (3.7). Other geometric primitives exist for a source definition, but the selection of an icosahedron is motivated by the fact that each face contains equal cross sectional areas. As such, computations based on intensity or the assignment of source directivity are easily facilitated.

In order to resolve detailed geometries, it is necessary to subdivide the cross-sectional areas of the source. Beginning with an icosahedron primitive, the faces of the icosahedron are subdivided in order to increase the density of propagating beams. Subdivision is achieved by bisecting the edges of each icosahedron face (Loop, 1987), projecting all of the resultant vertices to the unit sphere, and finally determining the convex hull of all vertices (Pion and Teillaud, 2013). This method is known as Loop subdivision. See Fig. 3.3(b) for an illustration of an icosahedron source refined twice by Loop subdivision.

3.2.3 Beam Definition

A beam is comprised of three beam rays, three beam planes, and three beam plane unit normals. A matrix with Q rows and three columns stores each beam reference. Each row corresponds to a beam and the entries in each row reference the beam

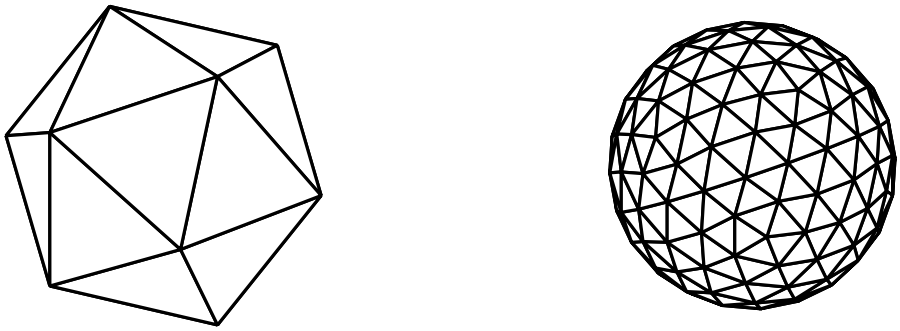

(a) (b)

Figure 3.3: Omnidirectional sources for beam tracing. (a) Icosahedron with 20 faces. (b) An icosahedron refined by two iterations of Loop subdivision resulting in 320 faces.

rays that make up the beam. A beam ray is parametrically defined as,

$$\vec{r}^{(b)}(l) = \vec{s} + \hat{d}^{(b)} l, \tag{3.7}$$

where $\vec{r}^{(b)}$ is the parametric beam ray, $\vec{s}$ is the (image) source position, $\hat{d}^{(b)}$ is the unit vector of the beam ray, l is the length of the ray, and the superscript (b) denotes a geometric property of a beam. For an initial beam the unit vectors correspond to the source vertices, as in Section 3.2.2. The beam ray references are ordered in an anticlockwise manner, viewed from the (image) source position. To ensure the beam rays are referenced in an anticlockwise manner the scalar triple product is used to orient the rays. Given the beam ray unit vectors, and the (image) source position, the beam rays are ordered in a clockwise or anticlockwise manner according to the sign of the triple scalar product (Drumm and Lam, 2000),

$$T_s = (\hat{d}_2^{(b)} - \vec{s}) \cdot \left[(\hat{d}_2^{(b)} - \hat{d}_1^{(b)}) \times (\hat{d}_3^{(b)} - \hat{d}_2^{(b)}) \right], \tag{3.8}$$

where $\hat{d}_1^{(b)}$ to $\hat{d}_3^{(b)}$ are the beam ray unit vectors for one beam, $T_s > 0$ indicates a clockwise orientation (viewed from the source), and $T_s < 0$ an anticlockwise orientation. The beam rays are ordered in an anti-clockwise manner so that the beam plane unit normals point out of the beam (Lewers, 1993). The beam plane unit normals are computed as,

$$\hat{n}_i^{(b)} = \frac{\hat{d}_i^{(b)} \times \hat{d}_{i \bmod 3+1}^{(b)}}{|\hat{d}_i^{(b)} \times \hat{d}_{i \bmod 3+1}^{(b)}|} \quad \text{for} \quad i = 1, 2, 3. \tag{3.9}$$

The beam plane normals are stored in a P by three matrix where each column is a Cartesian component of the beam plane normal. Conceptually a beam is a tetrahedron that expands in volume with a stationary vertex, being the source or image source position (Lewers, 1993). Three bounding planes, $\Pi_1^{(b)}$, $\Pi_2^{(b)}$, and $\Pi_3^{(b)}$ are beam planes which delimit the volume of the beam. The plane equation for each beam plane is defined by the beam plane normal, from Eq. (3.7), and the beam origin, cf. Eq. (3.3). Three bounding beam rays, $\vec{r}_1^{(b)}$, $\vec{r}_2^{(b)}$, and $\vec{r}_3^{(b)}$ define the extent of the beam; see Fig. 3.4.

3.2.4 Beam Propagation

A beam is bounded by three beam rays that define the extent of the beam. In contrast to classical beam tracing, which relies upon a central ray, the adaptive tetrahedral tracing algorithm utilizes each beam ray to determine the full extent of a beam. The added complexity is balanced by the ability to identify multiple polygons intersected by a beam (Lewers, 1993). Alternatively, a central ray can only identify a single polygon intersection. The fundamental geometric principles that govern the extent of rays applies equally to beam rays.

The first step to computing the extent of a beam ray is to determine the length of the ray to the nearest polygon. Substituting Eq. (3.7) into the plane equation,

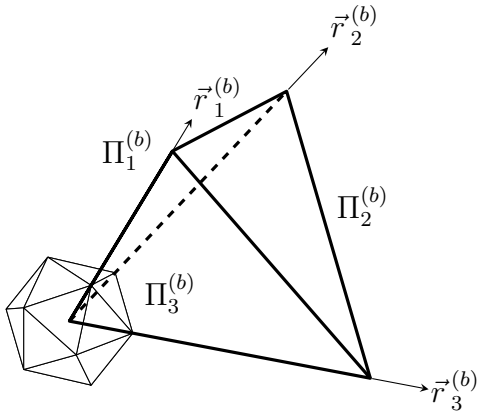

Figure 3.4: A representative beam originating from an icosahedron source. Three beam planes, $\Pi_1^{(b)}$, $\Pi_2^{(b)}$, and $\Pi_3^{(b)}$ delimit the volume of the beam. Associated with each beam plane is a beam plane unit normal that points out of the beam (not shown), defined by Eq. (3.9). Three beam rays, $\vec{r}_1^{(b)}$, $\vec{r}_2^{(b)}$, and $\vec{r}_3^{(b)}$ define the extent of the beam.

Eq. (3.3), and let the known point on the plane be a vertex of the polygon, Π,

$$\hat{n} \cdot (\vec{r}^{(b)}(l) - \vec{v}) = 0, \tag{3.10}$$

where $\vec{v}$ is any one of the four vertices of the polygon Π, and $\hat{n}$ is the polygon normal. Expanding Eq. (3.10) and rearranging terms results in the length of the beam ray (Long, 2006),

$$\hat{n} \cdot (\vec{s} + \hat{d}^{(b)} l - \vec{v}) = 0, \tag{3.11}$$

$$l = \frac{\hat{n} \cdot (\vec{v} - \vec{s})}{\hat{n} \cdot \hat{d}^{(b)}}. \tag{3.12}$$

It must be stressed that this beam ray length is the length of the ray to the plane associated with the polygon Π. It does not necessarily mean the ray intersects Π.

For multiple polygons the ray length computed by Eq. (3.12) is ambiguous since

not every ray length corresponds to a polygon intersection. Multiple tests are applied to confirm which polygon is the nearest polygon intersected by a beam ray. First, the ray length to a plane, associated with a polygon, must be for a potentially visible polygon. A simple test on potential visibility is based on the dot product of the beam ray unit vector and a polygon normal,

$$\hat{d}^{(b)} \cdot \hat{n} > 0, \tag{3.13}$$

which indicates the unit normal and the unit vector point into the same half-space. Once the set of polygons is reduced by Eq. (3.13), all the ray lengths are computed for the reduced set of polygons. Beam propagation is physically constrained for positive ray lengths. Thus, negative ray lengths are excluded from consideration. Finally, a point-in-polygon test is conducted. Several algorithms exist for checking whether a point is within a polygon, but the most computationally efficient algorithm relies upon the Jordan curve theorem (Long, 2006, p. 790). The algorithm is known as the ray-crossing algorithm (O'Rourke, 1998, sec. 7.5). The algorithm is applied to each polygon associated with a positive ray length in ascending order. The first polygon which satisfies the point-in-polygon test is the intersected polygon. The intersected polygon is linked to the beam ray. If a beam ray intersects two or more polygons at a polygon edge or vertex, then a list is generated that links the beam ray with references to each intersected polygon. Initial beam rays are shown for a beam in Fig. 3.5.

3.2.5 Ensonification Mapping

Once the length of each respective beam ray is computed then the ensonified region is mapped. Ensonified regions are demarcated by illumination rays. Illumination rays are traced along the intersection between a beam plane, and a polygon or

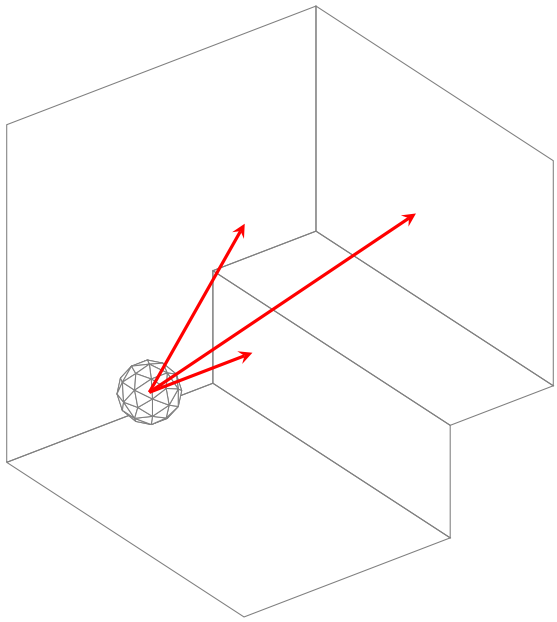

Figure 3.5: Initial propagation of beam rays. The icosahedron source is refined once and the beam rays are indicated by red rays.

multiple polygons. An initial illumination ray begins from the endpoint of one beam ray and ultimately continues until the next beam ray end point. The illumination ray traces a path within the beam plane and along polygons. Once an illumination ray intersects another beam ray endpoint, then another illumination ray is traced along the following beam plane. The process repeats until an enclosed area of ensonification is determined.

The ray equation for an illumination ray depends upon a beam plane and the polygon intersected by a beam ray or illumination ray. The intersection of a beam plane and the polygon depend upon the unit normals of the beam plane and polygon. The unit normal for a beam plane is determined by Eq. (3.9) and the unit normal for a polygon is determined by Eq. (3.2). Computation of the unit vector for the initial illumination ray is based on the cross product of the beam plane normal and polygon normal (Drumm and Lam, 2000),

$$\hat{d}^{(il)} = \hat{n}^{(b)} \times \hat{n}, \tag{3.14}$$

where $\hat{d}^{(il)}$ is the unit vector for the illumination ray. The superscript (il) indicates a property of an illumination ray. The unit vector computed by Eq. (3.14) is collinear with the line of intersection between the beam plane and the plane associated with the intersected polygon.

It is possible for a beam ray to intersect two or more polygons; see Sec. 3.2.4. It was suggested by Drumm and Lam (2000) that when an illumination ray intersects a polygon vertex, the correct unit vector, originating from the vertex, is the one that makes the sharpest turn at the vertex relative to the prior illumination ray. This criteria is closely related to determining the initial unit vector originating from a beam ray end point on a polygon edge or vertex. Computation of the angle between two vectors is facilitated by the dot product. For example, consider the dot product of two unit vectors of subsequent illumination rays,

$$\hat{d}_i^{(il)} \cdot \hat{d}_{i-1}^{(il)} = |\hat{d}_i^{(il)}||\hat{d}_{i-1}^{(il)}| \cos(\theta), \tag{3.15}$$

where the subscripts i and $i-1$ indicates two connected illumination rays in the same beam, and θ is the angle formed between the two unit vectors in three-dimensional space. This criteria may be sufficient to determine a subsequent unit vector; however it is insufficient to determine the initial unit vector for a beam ray intersecting a polygon vertex or edge. The criteria sufficient to handle both cases is based upon a physical argument. An illumination ray that originates from a polygon edge or vertex must continue within another polygon. Concisely, this can be stated as the principle of continuation. Infinitesimal rays are generated from the point of intersection with unit vectors computed according to Eq. (3.14). A point-in-polygon query is conducted for each infinitesimal ray end point and the associated polygon. The ray that continues within another polygon contains the correct unit vector.

Once the correct unit vector for an initial illumination ray is determined then an illumination ray, or multiple illumination rays, are traced to the following beam ray end point. The ray length to another beam plane or polygon is determined by Eq. (3.12). The correct length of an illumination ray is based upon the minimum distance to another polygon or beam plane. If the ray length to a beam plane is equal to or less than the length to the nearest polygon, then the length to the beam plane is selected and a beam plane intersection is noted. Otherwise, if the ray length to the nearest polygon is less than the length to the nearest beam plane, then the length to the polygon is selected and a polygon intersection is noted. For a beam plane intersection, or a polygon intersection, several cases require special attention. The nature of the intersection is evaluated for the purpose of continuing or terminating the ensonification mapping along a beam plane.

If a beam plane is intersected one of three cases are applicable. The first case applies when an illumination ray intersects a beam plane, and the end point of the ray coincides with the following beam ray end point. If this case applies, then the ensonification mapping within the current beam plane is terminated, and ensonification mapping continues along the next beam plane starting at the last intersection point (following beam ray end point). A second case occurs when a beam plane is intersected and the illumination ray end point does *not* coincide with the following beam ray end point. This case applies when an illumination ray traverses into a region of space invisible to the (image) source. In this particular case a reverse ensonification mapping is conducted. The current beam plane normal is reversed, and an illumination ray is generated from the following beam ray end point. This procedure effectively traces illumination rays in a reversed sense along the current beam plane. While a reverse trace is being conducted, each new illumination ray is checked against an overlapping condition with existing illumination rays. If an overlap occurs, then the intersection of the two illumination

rays is computed, the overlapped ray is eliminated, and the illumination ray tracing continues along the following beam plane. The third case occurs for reflected beams. A scenario may arise such that an illumination ray intersects a polygon and a beam plane. Furthermore, the intersection point is *on* the following beam ray. In this case the illumination ray tracing is terminated in the current beam plane and continues along the next beam plane, starting from the following beam ray end point.

If a polygon is intersected, then the next unit vector is determined according to one of two cases. Before defining the treatment of the two cases, it is necessary to define the terms locally concave and locally convex points. For example, the wedge geometry in Fig. 2.3 shows an open wedge angle for a convex wedge since the open wedge angle is greater than 180°. A point on the edge of the wedge is locally convex. In contrast, a concave wedge is a wedge with an open wedge angle less than 180°. Thus, a point on the edge of the wedge is locally concave. If an illumination ray intersects a polygon, then the intersection point is locally convex or locally concave depending upon the orientation of the intersected polygon at the point. However, an intersection point that coincides with three or more polygons may lead to some ambiguity in classifying the local geometry. Assuming that no ambiguity of the intersection point exists, the first case is an illumination ray intersecting a polygon, or multiple polygons, at a locally concave wedge. The following illumination ray is computed according to Eq. (3.14) and the principle of continuation. The second case is the intersection of a locally convex wedge. The visibility of the intersected polygon(s) is/are checked by Eq. (3.13). If the polygons are visible, then the principle of continuation is employed. Otherwise, discontinuous illumination ray tracing is employed. Discontinuous illumination ray tracing is the process of displacing the start point of the following illumination ray. The displaced start point is computed similarly to the end point of a beam ray, as in Sec. 3.2.4. Conceptually, a ray originates from the (image) source point, extends beyond the

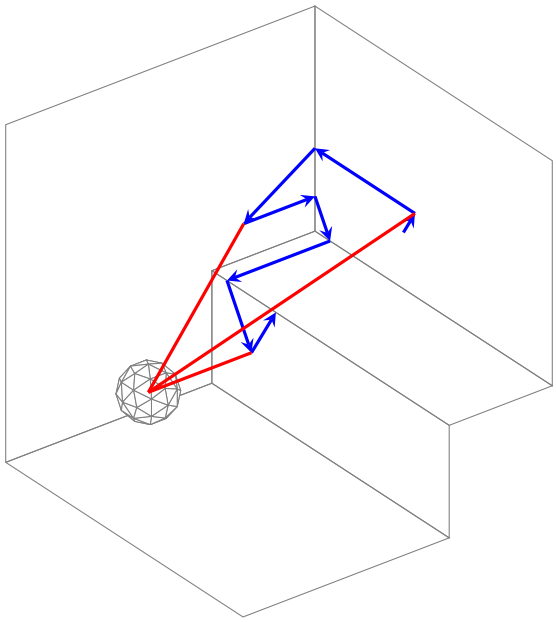

Figure 3.6: All illumination rays traced for a single beam. Illumination rays are indicated by blue rays. Rays are traced along beam planes from one beam ray endpoint to the next. Beam rays are indicated by red line segments. This illustration depicts discontinuous illumination ray tracing.

convex point of intersection, and the nearest polygon intersection is determined. Illumination ray tracing then proceeds from the displaced starting point. Fig. 3.6 illustrates discontinuous illumination ray tracing.

The process of ensonification mapping is inherently neutral with regards to visibility. As a result occluding surfaces will lead to the generation of partially visible or invisible illumination rays relative to the (image) source. Illumination rays originating from a beam ray end point are at least partially visible. Additionally, illumination rays that intersect a locally convex or locally concave point must be checked for visibility. Invisible illumination rays are eliminated and partially visible illumination rays are flagged for further processing. Partially visible rays are corrected through a process of obstruction mapping. Figure 3.7 illustrates the elimination of invisible illumination rays.

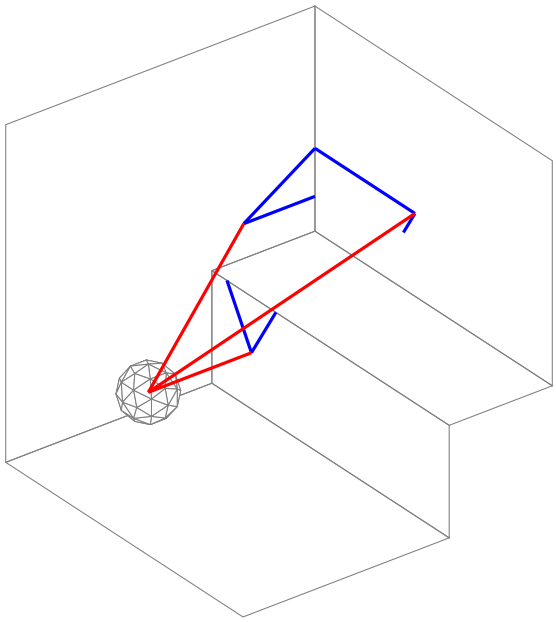

Figure 3.7: Elimination of illumination rays not visible to the source. Illumination rays are indicated by blue line segments and beam rays are indicated by red line segments. Two invisible illumination rays are eliminated within the beam, compare to Fig. 3.6.

3.2.6 Occlusion Mapping

Acoustic shadowing results from occluding geometry. Mapping the ensonification region in the presence of occluding geometry requires special attention. Drumm and Lam (2000) offer vague suggestions for occlusion mapping. In contrast, Campo et al. (2000) describe a more complete description for occlusion mapping, but as the study admits several scenarios are not mapped exactly. Thus, the algorithm sketched below offers a more comprehensive treatment of occlusion mapping.

Mapping the shadowing geometry profiles the occlusion and projects the profile to the furthest reaches of the incident beam. As part of the ensonification mapping procedure, an indication of occluding geometry is noted when an illumination ray intersects a polygon at a locally convex point. A locally convex point indicates the possibility that some geometric feature is occluding a portion of the beam. Confirmation of an occluding feature is dependent upon the convex point satisfying

a grazing incidence condition. The condition of grazing incidence is satisfied if one or more polygons at the convex vertex or edge is not visible to the (image) source. Once grazing incidence is confirmed at a locally convex point then an edge finding algorithm proceeds to find the shadowing edges contained within the beam. Every connected edge is determined by a breadth-first search (Cormen et al., 2009), and pushed onto a first-in first-out stack. Simultaneously the profile of each edge is projected to the furthest extent of the incident beam through a procedure similar to illumination ray tracing; see Section 3.2.5.

While the stack containing the shadowing edges is not empty. the extent of a shadowing edge is determined. The result is a shadow edge ray. It is determined whether a shadow edge ray intersects a polygon, multiple polygons, or a beam plane. If a shadow edge ray intersects a beam plane, and is completely visible, then shadow beam rays are generated from the (image) source through the end points of the shadow edge ray. The intersection points of the shadow beam rays serve as the starting and ending points for shadow illumination ray tracing. The shadow illumination rays are traced from one shadow beam ray end point to the other through the same process as illumination ray tracing, refer to Sec. 3.2.5. If another locally convex point is intersected while tracing a shadow illumination ray, then the occlusion mapping procedure is recursively conducted. Once any recursive procedures have completed then the shadow edge is pushed off the stack. An alternative scenario is when a shadow edge ray intersects a polygon, or multiple polygons. If the intersection point is locally convex, then the same procedure for shadow illumination ray tracing is conducted as above. Afterwards the shadowing edge is pushed off the stack. If the intersection point satisfies the condition of grazing incidence, then adjacent shadowing edges are determined. Otherwise, if the intersection point is locally concave, then the procedure is treated as a beam plane intersection. The process of occlusion mapping continues until the shadow edge

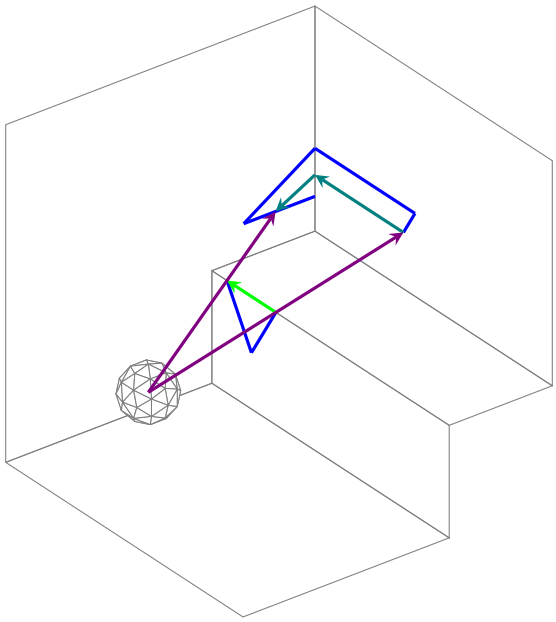

Figure 3.8: Shadow illumination rays are traced for an occluding edge. A shadow edge ray, shown as a green ray, is computed, which intersects a beam plane. Two shadow beam rays, shown as violet rays, project the end points of the shadow edge ray to the furthest extent within the beam. The shadow illumination rays, shown as teal rays, are traced from one shadow beam ray intersection point to the other. The illumination rays are shown as blue line segments.

stack is empty. An example of occlusion mapping is shown in Fig. 3.8.

3.2.7 Ensonification Mapping Corrections

Shadow illumination rays facilitate mapping corrections of illumination rays. Shadow illumination rays demarcate the termination of partially visible illumination rays. A procedure to correct the length of illumination rays must take two cases into account. Either the length of a ray must be modified, or the origin of the ray must be moved and the length modified. In both cases the necessary computations involve computing ray intersections.

The mechanics of determining ray intersections rely upon comparing unit directional vectors. All origin and end points of shadow illumination rays are computed for a particular beam. For each partially visible illumination ray the

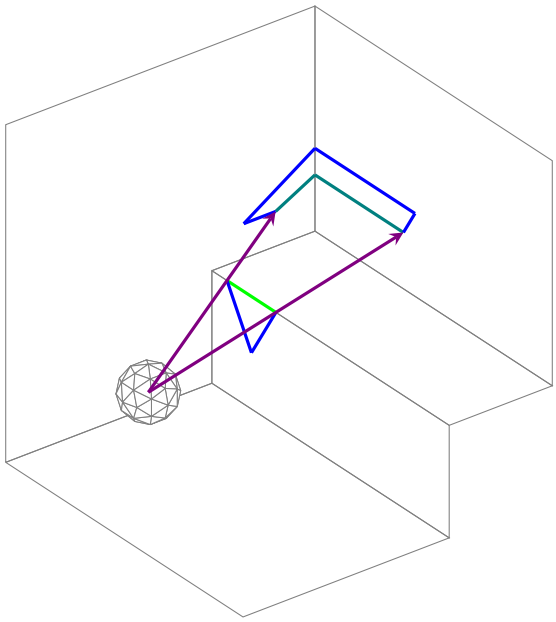

Figure 3.9: Illumination rays, shown as blue line segments, are trimmed according to the location of shadow illumination rays, shown as teal line segments. In this particular case one illumination ray is trimmed, compare to Fig. 3.7.

visible point of the ray is determined. Unit directional vectors from the visible point to each origin/end point of all other shadow rays are compared to the unit directional vector of the illumination ray. If a matching unit directional vector is found then the length of the illumination ray is matched to the length of the vector from the visible point to the origin/end point of the shadow illumination ray. Alternatively, if a match for a reversed unit directional vector is found then the origin of the illumination ray is redefined to be the origin/end point of the shadow ray, and the length of the illumination is adjusted accordingly. Figure 3.9 illustrates one illumination ray trimmed. Compare to Fig. 3.8.

Edge rays are computed from locally concave intersection points by illumination rays or shadow illumination rays. An edge finding algorithm, described in Sec. 3.2.6, is utilized to determine all the edge rays originating from a concave junction that are visible within the beam. As Fig. 3.10 illustrates an edge ray goes beyond the region of visibility. Generally, edge rays are traced until another polygon or beam

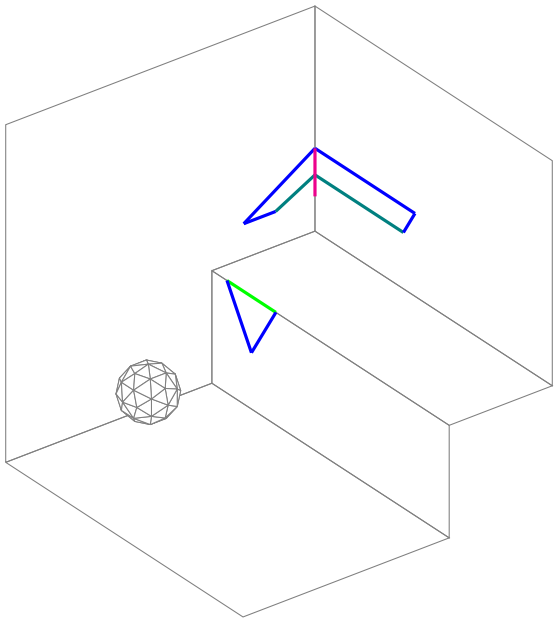

Figure 3.10: Edge rays are traced from concave junctions. One edge ray is shown as a magenta line segment.

plane is intersected. In the case of Fig. 3.10 the vertical edge ray traces from the concave junction to a beam plane. A ray trimming procedure is conducted on all edge rays, similar to illumination rays.

The total ensonification mapping concludes by gathering all illumination rays, shadow illumination rays, shadow edge rays, and edge rays together. Once all trimming corrections are conducted the total mapping for the ensonified region is complete. The conglomeration of all corrected rays are hereafter referred to as ensonification rays. Fig. 3.11 shows all regions of ensonification for a single beam. It is clear that relying upon a central ray for beam propagation is far from accurate considering the effect of shadowing.

3.2.8 Subdivision of Ensonification Mapping

Once an ensonification mapping is completed it may become necessary to subdivide the ensonification regions into coplanar, triangular, regions. Maintaining tetrahedral beam propagation requires the subdivision of non-triangular ensonification regions

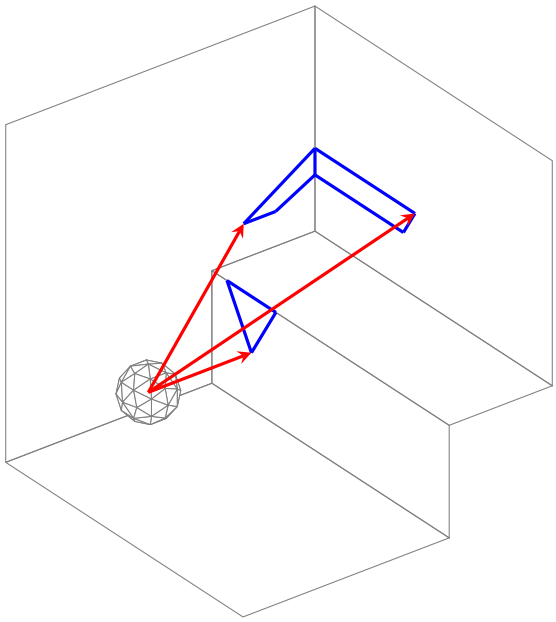

Figure 3.11: Ensonification rays define the extent of direct or reflected acoustic propagation from the source. The ensonification rays shown as blue line segments

into triangular regions. For ensonification regions that map across several polygons the regions must be subdivided into unique coplanar groupings of ensonification rays. Furthermore, each grouping must form a simple closed polygon. For example, Fig. 3.11 illustrates three unique coplanar groupings of ensonification rays. Once each unique coplanar region is identified then the non-triangular regions are subdivided according to a constrained Delaunay triangulation (Yvinec, 2013).

The first challenge for the subdivision of ensonified regions is to determine which ensonification rays are coplanar and form a simple closed polygon. Assuming all the ensonification rays in a beam are unique the first step is to determine which ensonification rays are coplanar. A naive approach is enumerate all triplet combinations of ensonification rays. For a small number of rays this approach is satisfactory; however, as the number of rays increases the number of combinations increases very rapidly since the total number of enumerations is equivalent to the binomial coefficient,

$$\binom{n}{k} = \frac{n!}{(n-k)!k!}, \tag{3.16}$$

where n is the total number of ensonification rays in a beam, and k is three in this case. Triplet combinations are generated since a coplanar test requires three unit vectors. In addition to a prohibiting number of combinations a large number of combinations are generated for physically unconnected rays. Rather than enumerate every combination a more efficient approach is to develop a search tree, which is generated by a breadth-first-search (Cormen et al., 2009) of the ensonification rays. The search tree contains all the ensonification rays as nodes of the tree and physical connections as links between the nodes. The search tree facilitates the generation of a reduced set of triplet combinations. For every ensonification ray triplet, a coplanarity test is based upon the determinant of a matrix of unit directional vectors (Ito, 1993, p. 1679),

$$T_c = \begin{vmatrix} d_{1,x}^{(il)} & d_{1,y}^{(il)} & d_{1,z}^{(il)} \\ d_{2,x}^{(il)} & d_{2,y}^{(il)} & d_{2,z}^{(il)} \\ d_{3,x}^{(il)} & d_{3,y}^{(il)} & d_{3,z}^{(il)} \end{vmatrix}, \tag{3.17}$$

where each row of the matrix above corresponds to a unit directional vector of each ensonification ray [see Eq. (3.14)], and $T_c = 0$ for three coplanar rays. Note, the computed determinant above is equivalent to the scalar triple product for three vectors,

$$T = \vec{a} \cdot (\vec{b} \times \vec{c}), \tag{3.18}$$

where T is the signed volume of a parallelepiped formed by vectors $\vec{a}$, $\vec{b}$, and $\vec{c}$. This is an alternative interpretation of the scalar triplet product as posed in Eq. (3.8). The set of all three ray combinations which satisfy $T_c = 0$, from Eq. 3.17, are inspected further. For each group the plane normal, computed by the cross product between two unit directional vectors [cf. Eq. (3.2)], is determined in order to find the distance of the plane from the origin, see Eq. (3.5). Each coplanar ray grouping

with the same plane normal, and distance from the origin are consolidated further. Set operations are performed on the ray groupings to consolidate the rays that satisfy coplanarity, and connectedness.

For each unique ensonification region, a simple closed polygon is formed and non-triangular regions are subdivided according to a constrained Delaunay triangulation. The formation of a simple closed polygon requires the ensonification rays to be arranged in a cyclic manner (O'Rourke, 1998, pp. 1, 2). Generally ensonification rays are not arranged in a cyclic manner since they are composed of illumination rays, shadow illumination rays, and edge rays. Thus, it becomes necessary to reverse the orientation of rays accordingly. Once all the ensonification rays form a simple closed polygon, the rays are projected to a Cartesian plane. The projection plane is dependent upon the largest component of the plane normal. Whichever component of the normal is largest the plane of projection is the plane formed by the two other Cartesian components. For example, if the component of the normal is largest along the y-axis then the plane of projection is the x-z plane. Constraints for the Delaunay triangulation are specified by an ordered list of ensonification ray origins, which confines the ensonification region. Finally, a constrained Delaunay triangulation is conducted on the ordered vertices, resulting in triangular regions of ensonification; see Fig. 3.12.

3.2.9 Child Beam Generation

If the ensonification mapping includes multiple regions requiring subdivision, then multiple child beams are generated for reflection. Otherwise, for a single triangular region the tetrahedral profile of the beam is preserved for reflection. Each child beam is generated by creating beam rays that originate from the (image) source to the vertices of a triangular region. The beam rays are oriented in an anticlockwise manner with the aid of the triple scalar product, cf. Eq. (3.8). Beam plane normals

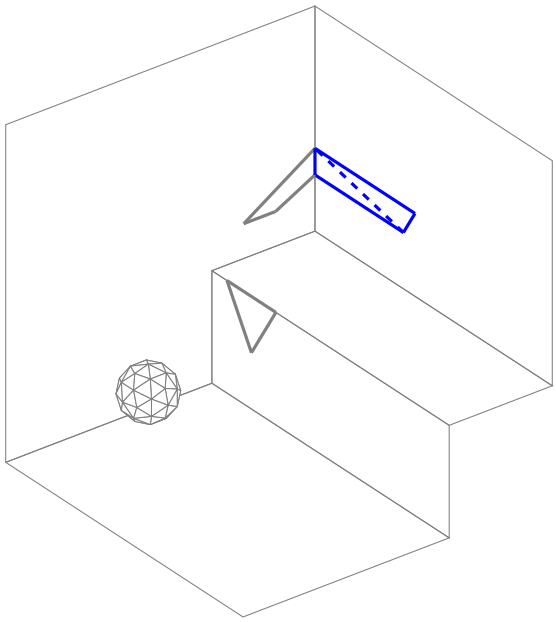

Figure 3.12: Subdivision of ensonification mapping. A coplanar, connected, region is highlighted by blue line segments. Constrained Delaunay triangulation of the region results in triangular regions, denoted by the blue dashed line.

are computed by Eq. (3.9). The intersection points of each beam ray are noted for each child beam, and any beam ray intersecting multiple polygons is noted as in Sec. 3.2.4. A child beam generated by the process of adaptive tetrahedral tracing is shown in Fig. 3.13. In the presence of occluding geometry a tetrahedral beam is clipped according to the extent of the occlusion. The clipping process results in the generation of several new beams. Greater computational resources are required for the adaptive beam tracing process compared to the ray tracing method, but in comparison to the image source method, less resources are required for high reflection orders (Drumm and Lam, 2000). However, in contrast to the ray tracing method or the image source method, the adaptive beam tracing method accurately determines the visibility of diffracting wedges from the (image) source.

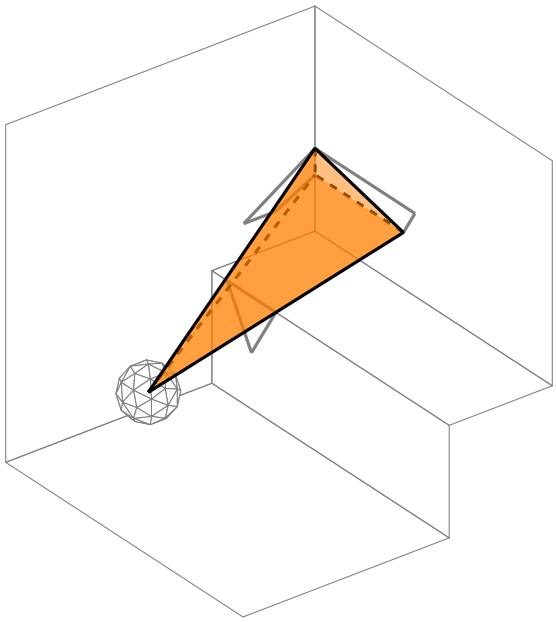

Figure 3.13: A child beam is generated for a portion of an ensonified region. The ensonified region is subdivided into two triangular regions by a constrained Delaunay triangulation. One child beam is shown in orange.

3.2.10 Beam Reflection

Each tetrahedral beam generated by the process in Sections 3.2.3–3.2.9 is either reflected or anechoically absorbed, assuming that all surfaces are either acoustically rigid or anechoic. The reflection of tetrahedral beams is governed by the geometric law of reflection. The geometric law of reflection states that the angle of incidence is equal to the angle of reflection. Equivalently, by the method of images the reflecting ray is determined by creating an image source, which is a mirrored source position about the reflecting point. The image source for a propagating beam is computed as (Drumm, 2005),

$$\vec{s}^{(i)} = \vec{s} + 2[(\hat{d}^{(b)}l) \cdot \hat{n}]\hat{n}, \tag{3.19}$$

where $\hat{d}^{(b)}l$ is the vector associated with a beam ray of a tetrahedral beam, $\vec{s}^{(i)}$ is the the image source position, and $\hat{n}$ is the unit normal of the polygon intersected by the beam ray. Similarly the reflected unit vectors of each beam ray are computed

as (Lewers, 1993),

$$\hat{d}_r^{(b)} = \hat{d}^{(b)} - 2(\hat{d}^{(b)} \cdot \hat{n})\hat{n}, \tag{3.20}$$

where $\hat{d}_r^{(b)}$ is the reflected beam ray unit vector.

Extra caution must be exercised when propagating a reflected tetrahedral beam. In addition to the normal procedure of beam ray propagation, outlined in Sec. 3.2.4, reflected beam rays must take extra considerations into account in order to be physically correct. First, at a minimum the reflected beam ray length must be equal to or greater than the distance from the image source position to the ensonification region. Second, the polygon intersected by the beam ray must be visible from the incident ensonification region. Accounting for these two physical constraints, in addition to the process described in Sec. 3.2.4, results in the correct computation of reflected beam rays.

3.2.11 Receiver Detection

It is suggested by Wareing and Hodgson (2005) that a receiver detection is dependent upon the relative positions of the source, receiver, and beam planes. In other words a receiver detects an incident beam by testing its presence within the three bounding beam planes of a beam. A receiver detection occurs when the following conditional relationship is satisfied (Wareing, 2000),

$$0 \leq \begin{cases} \hat{n}_1^{(b)} \cdot (\vec{r} - \vec{s}), \\ \hat{n}_2^{(b)} \cdot (\vec{r} - \vec{s}), \\ \hat{n}_3^{(b)} \cdot (\vec{r} - \vec{s}), \end{cases} \tag{3.21}$$

where $\hat{n}^{(b)}$ the beam plane normal computed by Eq. (3.9), $\vec{r}$ is the receiver position, and $\vec{s}$ is either the source or image source position. A similar suggestion is made by Drumm and Lam (2000). The scenario where this relationship breaks down is for

non-concave geometric domains. Coupled spaces is one particular example. A receiver may be within the volume of the bounding beam planes, but not within the extent of the beam. A stricter test is based on a different geometric test.

Since every propagating beam is a tetrahedral beam, a geometric query is sufficient to determine if a receiver detects an incident beam. Hence, a point-in-tetrahedron query determines whether a propagating beam intersects a point receiver. The test is based on the Cartesian coordinates of the tetrahedron and receiver. Five determinants are computed for the query (Yamaguchi, 2002, p. 221),

$$d_0 = \begin{vmatrix} t_{1,x} & t_{1,y} & t_{1,z} & 1 \\ t_{2,x} & t_{2,y} & t_{2,z} & 1 \\ t_{3,x} & t_{3,y} & t_{3,z} & 1 \\ s_x & s_y & s_z & 1 \end{vmatrix}, \tag{3.22}$$

$$d_1 = \begin{vmatrix} r_x & r_y & r_z & 1 \\ t_{2,x} & t_{2,y} & t_{2,z} & 1 \\ t_{3,x} & t_{3,y} & t_{3,z} & 1 \\ s_x & s_y & s_z & 1 \end{vmatrix}, \tag{3.23}$$

$$d_2 = \begin{vmatrix} t_{1,x} & t_{1,y} & t_{1,z} & 1 \\ r_x & r_y & r_z & 1 \\ t_{3,x} & t_{3,y} & t_{3,z} & 1 \\ s_x & s_y & s_z & 1 \end{vmatrix}, \tag{3.24}$$

$$d_3 = \begin{vmatrix} t_{1,x} & t_{1,y} & t_{1,z} & 1 \\ t_{2,x} & t_{2,y} & t_{2,z} & 1 \\ r_x & r_y & r_z & 1 \\ s_x & s_y & s_z & 1 \end{vmatrix}, \tag{3.25}$$

$$d_4 = \begin{vmatrix} t_{1,x} & t_{1,y} & t_{1,z} & 1 \\ t_{2,x} & t_{2,y} & t_{2,z} & 1 \\ t_{3,x} & t_{3,y} & t_{3,z} & 1 \\ r_x & r_y & r_z & 1 \end{vmatrix}, \tag{3.26}$$

where $t_{i,j}$ is the j-component of the i^{th} tetrahedral vertex ($i = 1, 2, 3$, and $j = x$, y, and z), and $\vec{s}$ is source or image source position. The tetrahedral vertices referenced in Eqs. (3.22)–(3.26) are the vertices at the base of the tetrahedron. The source position is the apex of the tetrahedron. The receiver position is denoted by $\vec{r}$. The receiver is within the tetrahedron if all the determinants in Eqs. (3.22)–(3.26) are all either greater than or less than zero. If any of the determinants are equal to zero then the receiver is on a boundary of the tetrahedron.

3.3 Summary

The tetrahedral tracing algorithm is an adaptive and recursive process of determining the extent of propagating beams in a geometric domain. An omnidirectional source is defined as either an icosahedron, or an icosahedron refined by Loop subdivision. Beam rays are propagated from the source to the furthest extent in the geometric domain. Illumination ray tracing maps the ensonification region delimited by the beam rays. If occluding geometry is present within a beam then shadow ray tracing determines the profile of occluding geometry and the projection of the occluding profile to the furthest extent of the beam. If necessary ensonification mapping corrections are conducted to completely map the ensonified region or regions. If multiple ensonification regions are generated by a beam, then each coplanar, connected region is identified and subdivided by constrained Delaunay triangulation. Child beams are generated after the ensonification regions are subdivided into triangular regions. The propagation of reflected beams are

governed by the geometric law of reflection. Finally, receiver detection is based on a point-in-tetrahedron query, which eliminates false-positive detections past strategies employed.

One particular advantage the adaptive tetrahedral tracing algorithm has compared to other geometric methods is the identification of diffracting edges. This capability is utilized to link together the algorithm with a secondary source model for edge diffraction; see Secs. 2.6.2–2.6.4. Details on joining the two models of acoustic propagation are given in Ch. 4.

Chapter 4

Fusion of Adaptive Tetrahedral Tracing and Edge Diffraction

Scattering by rigid acoustic diffusors is a combination of geometric propagation and diffraction. The multitude of interactions include reflections, diffractions, and permutations of the two mechanisms. Wave-based prediction methods, outlined in Chapter 2, solve for the scattered field as the sum total of all permutations of reflections and diffraction. The identification of individual propagation mechanisms is not possible due to the mathematical formulation. In contrast, an edge diffraction model accounts for specific, identifiable diffraction events; see Sec. 2.6. Similarly, a geometric propagation method accounts for specific, identifiable reflection contributions. The two models taken alone are insufficient to characterize diffusor scattering; however, linking the two offers an alternative approach for time-domain prediction.

In contrast to image source methods or ray tracing methods, adaptive tetrahedral tracing is highly compatible with edge scattering models. The adaptive tetrahedral tracing algorithm, described in Chapter 3, precisely maps the incident and reflected sound fields. In the presence of geometric discontinuities the mapping

is generated by splitting incident and reflected beams. The same geometric discontinuities that lead to beam splitting may also lead to acoustic diffraction. By design the acoustic mapping generated by adaptive tetrahedral tracing inherently contains information required for edge diffraction computations. Therefore, by extracting the information required for edge diffraction computations from the acoustic mapping, a bridge is formed between adaptive tetrahedral tracing and edge scattering models.

The chapter proceeds by exploring the link between adaptive tetrahedral tracing and an edge diffraction model in Sec. 4.1. After, in Sec. 4.2 graph theory is applied to the generation of geometric reflection and diffraction permutations. Sec. 4.3 details the generation of digital impulse responses from scattering predictions. The joint model for acoustic scattering is numerically verified by three case studies in Sec. 4.4. Finally, a summary is given in Sec. 4.5.

4.1 Linking Adaptive Tetrahedral Tracing and Edge Diffraction

The adaptive tetrahedral tracing method generates an acoustic mapping of incident and reflected sound fields. The incident and reflected sound fields are determined by propagating tetrahedral beams from the source or image sources. In the presence of surface discontinuities a propagating tetrahedral beam is split, conforming to the incident geometry. The conforming nature of adaptive tetrahedral tracing is the key element for identifying diffracting edges.

If a tetrahedral beam is split, then portions of split profiles may be collinear with surface discontinuities. For each child beam, new beam rays are computed from the (image) source to the triangular profile, as in Sec. 3.2.4. At a surface discontinuity a beam ray intersects two or more polygons. If two or more beam rays

of a child beam intersect multiple polygons, then a diffracting edge may be collinear with a portion of the beam profile. The condition of collinearity is satisfied if two polygon unit normals, associated with one beam ray, match two other polygon unit normals, associated with another beam ray.

Once a diffracting edge is identified the wedge geometry is deduced from the available information. First, the z-axis of a cylindrical coordinate system is aligned with the edge. The direction of the axis is opposite to the edge vector of the reference polygon. More precisely, the reference polygon contains a unit normal in the opposite direction of the azimuth unit vector. In other words, the fingers of a right hand come out of the reference polygon when the thumb is aligned with the z-axis of the wedge. Once the reference polygon is established then the open wedge angle is computed with the aid of the triple scalar product,

$$T_s = -\hat{k} \cdot (\hat{n}_1 \times \hat{n}_2), \tag{4.1}$$

where $\hat{k}$ is the unit vector aligned with the z-axis, $\hat{n}_1$ is the reference polygon unit normal, $\hat{n}_2$ is the second polygon forming the wedge, and T_s is the triple scalar product. The computation of the open wedge angle depends upon the sign of the triple scalar product,

$$\theta_W = \begin{cases} \pi - \arccos(\hat{n}_1 \cdot \hat{n}_2) & \text{if } T_s < 0, \\ \arccos(\hat{n}_1 \cdot \hat{n}_2) + \pi & \text{if } T_s > 0, \end{cases} \tag{4.2}$$

where θ_W is the open wedge angle computed in radians. If the open wedge angle is any angle equal to π/m radians, where m is an integer, then no acoustic diffraction is emitted from the wedge (Biot and Tolstoy, 1957). After the open wedge angle is computed, the length of the diffracting wedge is determined by the distance between the two beam ray end points. Finally, the cylindrical coordinates of the (image)

source and (image) receiver are computed relative to the wedge by two coordinate transformations. The global Cartesian coordinate system is mapped to a local Cartesian coordinate system along the wedge. The local coordinate system is oriented such that the x-axis points into the reference polygon, and the y-axis points away from the reference polygon unit normal. The local Cartesian coordinates are then transformed to cylindrical coordinates.

The extraction of wedge parameters from an acoustic mapping of sound propagation links together adaptive tetrahedral tracing and edge diffraction models. Specifically, a secondary source model for edge diffraction, described in Sec. 2.6, is well-suited for computing first-order, second-order, and higher-order diffraction in the time-domain. The wedge parameters generated by the extraction process are sufficient for the computation of first-order diffraction impulse responses. However, additional considerations are required for second, and higher-order diffraction.

4.2 Graph Theory Applied to Multiple-Order Diffraction

Determination of sound propagation paths from source, to multiple edges, and then to a receiver is essentially a problem associated with graph theory (Bang-Jensen and Gutin, 2001). The problem is similar to finding sound transmission paths in statistical energy analysis (Guasch and Cortes, 2009). Given the source, edges, and receiver are considered as nodes in a directed graph it becomes essential to determine which paths are valid; see Fig. 4.1(a). A defining feature of a directed graph for sound propagation is the one-way sound transmission from source to all visible edges. Furthermore, all edges visible to the receiver result in sound diffraction directed to the receiver. Sound transmission is bidirectional between edges, if a portion of one edge is visible to another. Construction of the directed

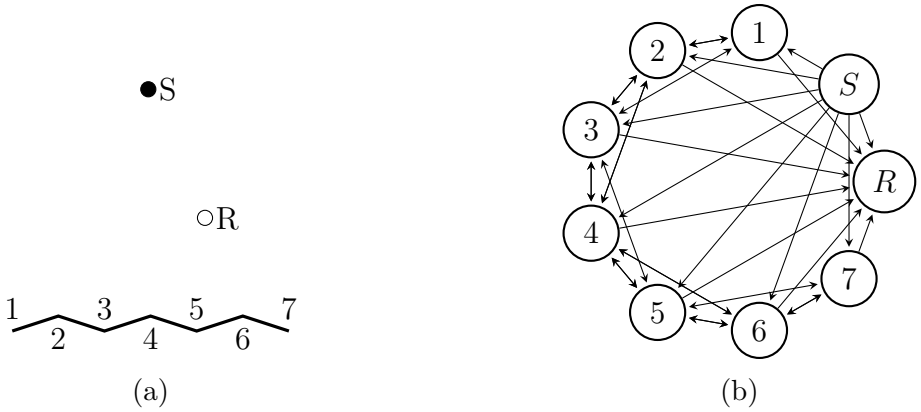

Figure 4.1: Directed graph representation of source, edges, and receiver. (a) Physical geometry of source, scattering object, and receiver. Each diffracting edge of the object is labeled numerically. (b) Directed graph indicating paths of sound propagation from source to receiver, and source to edges to receiver.

graph, for sound propagation, is based on visibility. Visibility between a source to an edge, an edge to another edge, and an edge to a receiver is necessary for diffraction sound propagation. Source to edge, or receiver to edge visibility is determined by the adaptive beam tracing algorithm. By tracing beams from either the source or receiver, visible edges are identified by the beam clipping and subdivision process; see Ch. 3. On the other hand, edge to edge visibility is a distinct challenge since it requires computing region to region visibility, rather than point to region visibility. Several different approaches exist to determine edge to edge visibility (Cohen-Or et al., 2003). The following discussion is limited to two different approaches for determining edge to edge visibility.

Various methods exist for determining edge to edge visibility, ranging from the simple to very complex. A simplistic manner of determining edge to edge visibility is based upon a ray casting technique from each edge midpoint; refer to Sec. 3.2.4. If no obstructions exist between each edge midpoint, then the edges are considered visible. A more accurate method is based on computing conservative from-region visibility between edges to identify all possible mutually diffracting edges (Antani et al., 2012). After the conservative from-region visibility computation each

diffracting edge is subdivided into equal sized segments. Ray casting between each segment midpoint is conducted in order to determine the mutual visibility of edge segments. Unobstructed rays between each segment midpoint indicates a visible edge segment. Visible edge to edge segments give second order diffraction contributions as in Eq. 2.77. The first approach based upon ray-casting from an edge midpoint to another edge midpoint is used for visibility testing in the present study in order to avoid time-consuming computations for from-region visibility, as in (Antani et al., 2012). A further simplification is to assume each mutually visible edge is completely visible. Thus, no account is taken of partially visible edges for second- and higher-order diffraction. This assumption is justifiable when computing two-dimensional acoustic diffusors since the diffracting edges have a consistent profile in two-dimensions. Once visibility computations are completed then the relationships between the source, edges, and receiver are established as a directed graph; see Fig. 4.1(b). In the directed graph representation the source, diffracting edges, and receiver are treated as nodes. The sound transmission paths between the source, edges, and receiver are denoted as directed edges or links in the directed graph. The computational equivalent of the directed graph is the adjacency matrix.

The adjacency matrix is a graph theoretic data structure which defines the relationships between nodes of a directed graph (Bang-Jensen and Gutin, 2001, p. 30). Each entry of the adjacency matrix is either a zero or a one. A entry of one in the i^{th} row and j^{th} column of the matrix indicates a directed link between the nodes i and j. The adjacency matrix, formed by edge to edge visibility, is a subset of the complete adjacency matrix. Provided the source to edge visibility and edge to receiver visibility information are known, the full adjacency matrix is formed by including edge to edge visibility. The analog of the adjacency matrix is an incidence list, which is also known as an adjacency list representation (Bang-Jensen and Gutin, 2001, p. 30). An incidence list is formed from the adjacency matrix in order

to facilitate path searching. The ultimate goal is to determine every single path from the source node to the receiver node based on a user-defined depth. In other words all paths for n orders of diffraction are formed by the traversal of $n+1$ edges along the directed graph, from the source to receiver nodes. Such a path is known as a (s,t)-walk of length $n+1$, where s is the source node and t is the terminal node (Bang-Jensen and Gutin, 2001, p. 11). The incidence list, formed from the adjacency matrix facilitates the discovery of sound diffraction paths.

Searching the directed graph for specific paths, with a defined length, is based on the generated incidence list and two well-known searching algorithms. First, a modified breadth first search (BFS) is conducted on the incidence list resulting in a search tree based on the directed graph. Typical BFS algorithms search a directed graph until all nodes are discovered and then stop (Cormen et al., 2009, pp. 531–534). Nodes which are discovered are marked as such and only new nodes are found through the process. The BFS algorithm is modified in the present study in order to continue searching through the directed graph for a specified depth. The modified algorithm purposefully forgets nodes discovered in order to trace paths going over previously visited nodes. Instead of marking a node as visited and preventing the node from being revisited, the modified algorithm marks a node as visited and allows the same node to be revisited. Since some edge nodes are directed to each other, some paths of the search tree will include recurring paths between edge nodes. This behavior is desirable since any arbitrary order of diffraction is placed in a search tree by the modified BFS. After a modified BFS is conducted, a modified depth first search (DFS) is applied to the search tree. Typical DFS algorithms search a directed graph similar to a BFS (Cormen et al., 2009, pp. 540, 541). The modified DFS begins from the receiver vertex and determines path sequences to the source vertex for each level of the tree. The search begins at the receiver node since the receiver typically views less of the total geometric domain

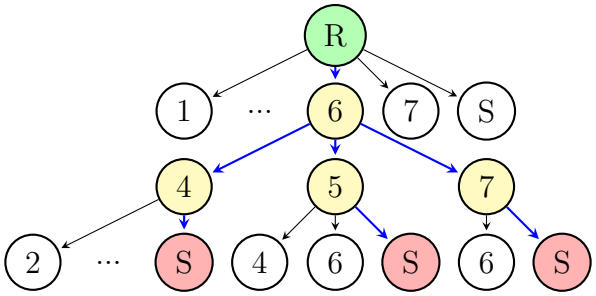

Figure 4.2: Partial search tree of a directed graph from Fig. 4.1(b). The partial search tree is generated by a modified BFS. The depth of search tree is three. Yellow nodes indicate diffracting wedges. Blue arrows show paths of second-order diffraction. A DFS begins at the receiver, R, and searches for all paths ending at the source, S, for a specified depth.

than the source when computing acoustic scattering polar responses; see Sec. 4.4.2. The search concludes once all valid sequences of the maximum depth are enumerated. An example of second-order diffraction paths associated with edge six of Fig. 4.1(a) is illustrated in Fig. 4.2. The directed graph from Fig. 4.1(b) is converted into a search tree of depth three for the purpose of finding second-order diffraction paths from the source to the receiver. In the language of graph theory all (s,t)-walks of length three are determined where the source vertex, s, is the receiver, and the target vertex, t, is the source. A partial representation of the search tree is given in Fig. 4.2.

4.3 Digital Synthesis of an Impulse Response

The total sound field is approximated by summing free field, geometric, and diffraction components of the sound field. In the continuous time-domain the summation of all three components is represented as,

$$h(t) = h_{FF}(t) + h_{GA}(t) + h_D(t), \tag{4.3}$$

where $h_{FF}(t)$ is the free field impulse response, $h_{GA}(t)$ is the geometric impulse response, and $h_D(t)$ is the diffraction impulse response. The summation of acoustic components is valid for linear acoustics. The free field and geometric sound fields are determined directly by the beam tracing algorithm; see Ch. 3. The free field impulse response is simply a scaled Dirac delta function,

$$h_{FF}(t) = \frac{\delta(t - R_0/c)}{R_0}, \tag{4.4}$$

where δ is the Dirac delta function, and R_0 is the distance from the source to receiver. Specular reflection is accounted for by determining image source contributions,

$$h_{GA}(t) = \sum_{n=1}^{N} \frac{\delta(t - R_n/c)}{R_n}, \tag{4.5}$$

where R_n are the distances from image sources to receiver and N is the total number of image sources. Note, Eq. (4.5) implies acoustically rigid boundary conditions for reflecting surfaces. The diffraction sound field is approximated by summing a finite number of diffraction contributions by the secondary source model for edge diffraction (see Section 2.6),

$$h_D(t) = \sum_{i=1}^{K} h_{D,i}(t), \tag{4.6}$$

where K is the total number of diffraction permutations.

Acoustic scattering by diffusors is approximated by Eq. (4.3) where Eq. (4.6) is the approximating term. Since scattering by diffusors is limited to a finite number of reflections Eq. (4.4) satisfies the geometric field exactly. However, a finite-number of diffraction permutations is accounted for in Eq. (4.6). For example, in the present study, permutations include any number of geometric reflections proceeding or succeeding diffraction. However, geometric reflections between diffraction events are

not accounted for. An extra layer of complexity is required for computing geometric reflections between diffraction events. Image, or mirrored, edges must be computed for determining such permutations. Additionally, slope diffraction is neglected (Summers, 2013) and a finite order of diffraction is computed.

The numerical computation of Eq. (4.3) is synthesized digitally by converting the continuous-time expressions to discrete-time expressions. The Dirac delta function in Eqs. (4.4) and (4.5) are converted to a Kronecker delta function, which is either equal to zero or one when the time delay factor R/c exactly corresponds to a discrete-time sample. Discrete time expressions for first- and second-order diffraction are given in Eqs. (2.76) and (2.77), respectively. Generally, the argument for the Kronecker delta function, associated with either Eq. (4.4) or Eq. (4.5), is never exactly equal to zero for a discrete-time sample. Oftentimes a fractional delay is associated with the onset of arrival for a pulse. The arrival time is usually between two discrete-time samples. The difference between the onset of arrival and the nearest time sample, prior to the arrival time, is known as the fractional delay. Thus, it becomes necessary to distribute the impulse contribution over more than one time sample. Similarly, the discrete-time contribution of diffraction in Eqs. (2.76) and (2.77) must consider fractional delays.

One approach for handling a fractional delay is to apply a fractional delay (FD) finite impulse response (FIR) filter, in order to distribute a transient pulse. The low impulse method is a particular implementation of a FD FIR filter (Peterson, 1986). A sinc function is Hanning windowed and designed with 40 taps. The Hanning window is applied to the sinc function in order to reduce Gibbs phenomenon, which reduces ripples in the frequency response near the Nyquist frequency. The frequency response of the filter is very good up to 90% of the Nyquist frequency. The trade-off associated with the filter is the long filter length. Another type of FD FIR filter is the Lagrange interpolator.

Design of a maximally flat filter, at zero frequency, results in a filter based on Lagrange interpolation. The form of the the Lagrange FIR FD filter is (Laakso et al., 1996),

$$h[n] = \prod_{\substack{k=0 \\ k \neq n}}^{N} \frac{D-k}{n-k} \qquad \text{for } n = 0, 1, 2, ..., N, \tag{4.7}$$

where N is the filter order, and D is the fractional delay of the signal. The ideal phase response for a FD FIR filter is linear phase, which means all the frequency components of a signal have equal delay times. In order to form a Lagrange filter with the best phase characteristics the fractional delay, D, must be within a certain range based on the filter order. For an even order filter the optimal fractional delay is $(N/2) - 1 \leq D \leq (N/2) + 1$, and for an odd order filter the optimal range is $(N-1)/2 \leq D \leq (N+1)/2$ (Välimäki, 1995). A special case of the Lagrange interpolator is choosing a filter order of one. The resulting filter is the linear interpolator,

$$\begin{aligned} h[0] &= 1 - D, \\ h[1] &= D, \end{aligned} \tag{4.8}$$

which is suggested by Svensson et al. (1999) for distributing second order diffraction contributions in Eq. (2.77). The magnitude and phase of the linear interpolator ($N = 1$) are shown in Fig. 4.3. Fractional delay values range from 0.0 to 1.0 for each subfigure. The magnitude response is symmetric for pairs of fractional delays, such as 0.1 and 0.9, 0.2 and 0.8, and so on. The largest attenuation occurs for a delay value of 0.5. Linear phase is only preserved for low frequencies. The magnitude response of the linear interpolator exhibits a low-pass characteristic with a narrow region that is flat. Improvement of the linear interpolator is possible by extending the filter order of the Lagrange interpolator. The greatest relative gains, in terms of

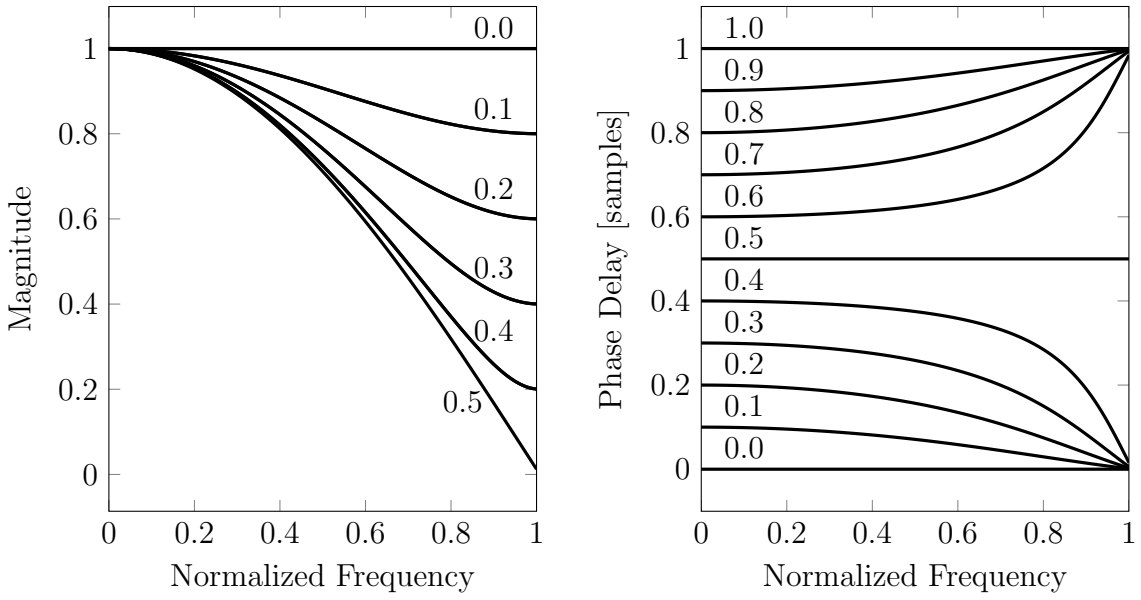

Figure 4.3: First order ($N = 1$) Lagrange fractional delay finite impulse response filter (linear interpolator). (a) Magnitude responses for eleven fractional delays, from 0.0 to 1.0. The magnitude responses are symmetric such that a fractional delay of 0.9 overlaps a fractional delay of 0.1. (b) Phase delay responses for eleven fractional delays, from 0.0 to 1.0.

widening the low-pass band and preserving linear phase, results from increasing the filter order to three. Figure 4.4 shows the magnitude and phase of the third order ($N = 3$) Lagrange interpolator. Compared to the linear interpolator the third order Lagrange interpolator has a wider low-pass band. For example, given a fractional delay of 1.5, a 0.1 dB or larger attenuation occurs for frequencies greater than 27% of the Nyquist frequency. The same attenuation for a linear interpolator, and a fractional delay of 0.5, occurs for frequencies greater than 10% of the Nyquist frequency.

Based on the advantages of a short filter length, good low-pass bandwidth, and linear phase characteristics the third-order Lagrange interpolator is utilized for the digital synthesis of direct, reflected, second-order diffraction, and higher-order diffraction impulse responses in the present study. Broadband frequency responses, with little magnitude and phase distortion, are possible by setting the sampling

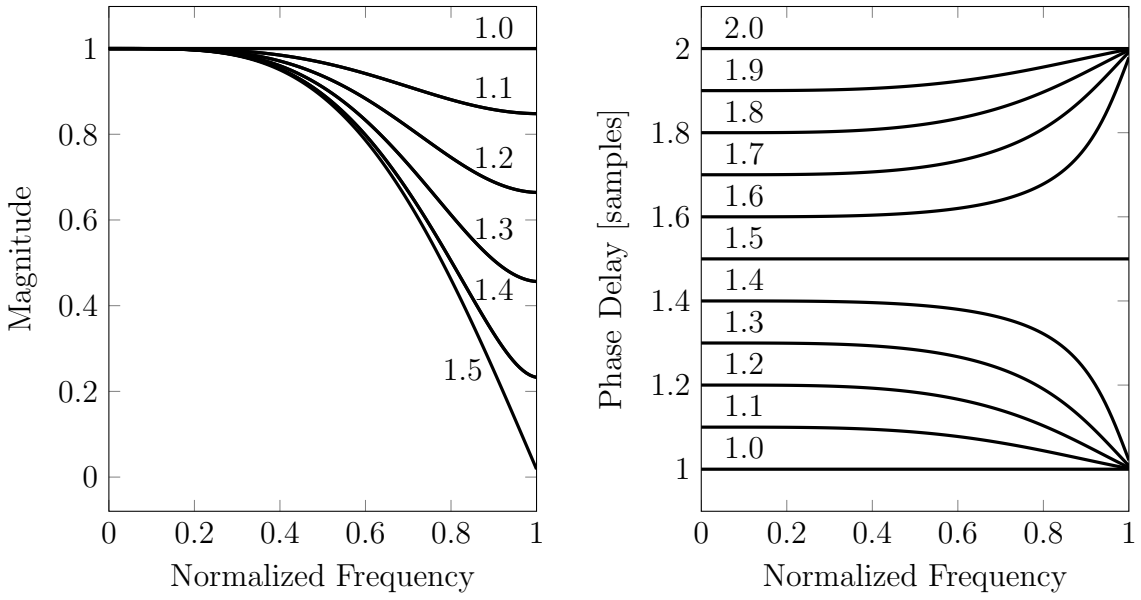

(a) (b)

Figure 4.4: Third order Lagrange fractional delay finite impulse response filter. (a) Magnitude responses for eleven fractional delays, from 1.0 to 2.0. The magnitude responses are symmetric such that a fractional delay of 1.9 overlaps a fractional delay of 1.1. (b) Phase delay responses for eleven fractional delays, from 1.0 to 2.0.

frequency to 160 kHz. Frequency responses in the range of 0 to 20 kHz have negligible magnitude and phase distortion. Digital synthesis of first-order diffraction is treated separately by increasing the sampling frequency to 800 kHz and resampling the resulting impulse response down to 160 kHz. The resampling is necessary in order to combine first-order diffraction impulse responses with other impulse responses.

4.4 Verification Cases

The fusion of adaptive tetrahedral tracing and a secondary source model for edge diffraction is numerically validated against three test cases. The adaptive tetrahedral tracing algorithm, and interface with the edge diffraction model were coded in MATLAB. The edge diffraction model was coded by Peter Svensson, in MATLAB. The first test case is on the scattering of a rigid acoustic wedge. The

second test case is on the scattering of a rigid panel. The third test case is on the scattering of a triangular diffusor. For the first test case numerical results are compared against an asymptotic formulation of diffraction. For the last two test cases numerical results are compared against BEM predictions. The first test case illustrates the capability of the adaptive tetrahedral tracing procedure to identify wedge parameters for first order diffraction calculations. The second test case demonstrates a capability for calculating higher-order diffraction and geometric reflection. Lastly, the third test case demonstrates the limitations on computing a finite number of reflection and diffraction permutations.

4.4.1 Rigid Acoustic Wedge

The acoustic scattering of a rigid acoustic wedge, with a closed wedge angle, θ_{WC}, of $\pi/2$ is computed with adaptive tetrahedral tracing and a secondary source model for edge diffraction, and compared with an asymptotic formulation for diffraction (Pierce, 1974; Hadden, Jr. and Pierce, 1981). The source and receiver have cylindrical coordinates ($r_S = 1$, $\theta_S = 4\pi/3$, $z_S = 0$) and ($r_R = 3$, $\theta_R = \pi/4$, $z_R = 0$), respectively. The diffraction formulation by Pierce (1974) is based on acoustic diffraction from an infinitely long wedge. The geometry of the tested scenario is shown in Fig. 4.5.

A portion of the total acoustic field is composed of free field radiation and geometric propagation, referred hereafter as the geometric acoustic sound field. In (Pierce, 1974) a time dependence of $e^{-i\omega t}$ is assumed; however, a time dependence of $e^{j\omega t}$ is used for the following variable definitions. Geometric parameters corresponding to source, receiver, and wedge face angles are the basis for the

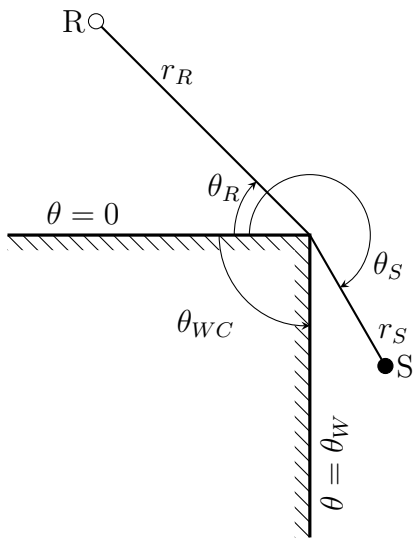

Figure 4.5: Right angled wedge geometry for comparing hybrid method and Pierce's formulation for wedge diffraction. The closed wedge angle, θ_{WC}, is $\pi/2$. The source, S, has the following cylindrical coordinates: ($r_S = 1$, $\theta_S = 4\pi/3$, $z_S = 0$). The receiver, R, has the following cylindrical coordinates: ($r_R = 3$, $\theta_R = \pi/4$, $z_R = 0$).

geometric acoustic sound field (Hadden, Jr. and Pierce, 1981),

$$\theta_1 = |\theta_S - \theta_R|, \tag{4.9a}$$

$$\theta_2 = \theta_S + \theta_R, \tag{4.9b}$$

$$\theta_3 = 2\theta_W - (\theta_S + \theta_R), \tag{4.9c}$$

$$\theta_4 = 2\theta_W - |\theta_S - \theta_R|, \tag{4.9d}$$

where θ_1 is the exterior angle formed by the source and receiver, θ_2 is the exterior angle formed by the source reflected about the $\theta = 0$ plane and receiver, θ_3 is the exterior angle formed by the source reflected about the $\theta = \theta_W$ plane and receiver, and θ_4 is the exterior angle formed by the source reflected about the $\theta = \theta_W$ plane and the receiver reflected about the $\theta = 0$ plane. Each of the above parameters corresponds to a component of the geometric sound field. The angle θ_1 corresponds to the direct wave, θ_2 corresponds to the wave reflected from the $\theta = 0$ plane, θ_3 corresponds to the wave reflected from the $\theta = \theta_W$ plane, and θ_4 corresponds to the

wave reflected from the $\theta = 0$ and $\theta = \theta_W$ planes. The total geometric sound field, cast as a Green's function, is given as a sum of each geometric component,

$$G(\vec{r}_S; \vec{r}_R)_G = \sum_{i=1}^{4} \frac{e^{-jkR_i}}{R_i} H(\pi - \theta_i), \tag{4.10}$$

where G_G is the geometric acoustic Green's function from the source position $\vec{r}_S$ to the receiver position $\vec{r}_R$, $H(\pi - \theta_i)$ is the Heaviside step function, e^{-jkR_i}/R_i represents a spherically diverging wave, and R_i represents the distance from the (image) source to the (image) receiver,

$$R_i = \sqrt{r_S^2 + r_R^2 + (z_S - z_R)^2 - 2r_R r_S \cos\theta_i}. \tag{4.11}$$

To complete the computation of the sound field the diffracted sound field must be considered.

The diffracted sound field is formulated through an asymptotic expansion of a contour integral. The Green's function for diffraction is (Pierce, 1974),

$$G(\vec{r}_S; \vec{r}_R)_D = \frac{e^{-jkL_0}}{L_0} \frac{e^{-j\pi/4}}{\sqrt{2}} (S_+ + S_-), \tag{4.12}$$

where L_0 is the least time path from the source to the receiver; see Sec. 2.6.1. The variable $S_\pm = S(\theta_R \pm \theta_S)$ is similar to all other variables with a plus or minus subscript, and is defined as,

$$S_\pm = \frac{\pi(1 + \Delta_\pm) W_\pm A_D(W_\pm) - \Delta_\pm}{\pi X_\pm}, \tag{4.13}$$

where $X_\pm = X(\theta_R \pm \theta_S)$, $W_\pm = W(\theta_R \pm \theta_S)$, and $\Delta_\pm = \Delta(\theta_R \pm \theta_S)$. Each of the

variables in $S_{\pm}$ are defined as,

$$X(\theta) = \gamma M_{\nu}(\theta), \tag{4.14a}$$

$$W(\theta) = \gamma N_{\nu}(\theta), \tag{4.14b}$$

$$\Delta(\theta) = \frac{\cos(\nu\pi)}{2} \frac{\cos(\nu\pi) - \cos(\nu\theta)}{1 - \cos(\nu\pi)\cos(\nu\theta)}, \tag{4.14c}$$

where $\nu = \pi/\theta_W$ is the wedge index and,

$$M_{\nu}(\theta) = \frac{\cos(\nu\pi) - \cos(\nu\theta)}{\nu \sin(\nu\pi)}, \tag{4.15a}$$

$$N_{\nu}(\theta) = \frac{\cos(\nu\pi) - \cos(\nu\theta)}{\nu\sqrt{1 - \cos(\nu\pi)\cos(\nu\theta)}}, \tag{4.15b}$$

$$\gamma = \sqrt{\frac{2r_S r_R}{\lambda L_0}}, \tag{4.15c}$$

where $\lambda = c/f$ is the acoustic wavelength. The parameter $A_D(W)$ is defined as,

$$A_D(W) = \text{sign}(W)[f(|W|) + jg(|W|)], \tag{4.16}$$

where the auxiliary Fresnel functions $f(W)$ and $g(W)$ are defined in terms of the Fresnel integrals,

$$\begin{aligned} f(W) = {} & [(1/2) - S(W)]\cos([1/2]\pi W^2) \\ & - [(1/2) - C(W)]\sin([1/2]\pi W^2), \end{aligned} \tag{4.17a}$$

$$\begin{aligned} g(W) = {} & [(1/2) - C(W)]\cos([1/2]\pi W^2) \\ & + [(1/2) - S(W)]\sin([1/2]\pi W^2), \end{aligned} \tag{4.17b}$$

and the Fresnel cosine and sine integrals are,

$$C(W) = \int_0^{|W(\theta)|} \cos([1/2]\pi t^2)\,\mathrm{d}t, \tag{4.18a}$$

$$S(W) = \int_0^{|W(\theta)|} \sin([1/2]\pi t^2)\,\mathrm{d}t. \tag{4.18b}$$

The Fresnel integrals are computed by adaptive Simpson quadrature (Gander and Gautschi, 2000). The total sound field is simply a summation of geometric and diffraction Green's functions from Eqs. (4.10) and (4.12).

A reasonable comparison between the hybrid method and Pierce's method, which assumes an infinite wedge, requires a sufficiently long finite wedge. The reason is the low frequency response is dictated by the decaying tail of diffraction, which is affected by the length of the wedge. A longer wedge results in a longer diffraction tail. A wedge 40 m long was computed with the adaptive tetrahedral tracing edge diffraction method. The length is sufficiently long such that the frequency response at low frequencies does not change considerably given a longer wedge.

In order to compare the results against Pierce's formulation a transfer function is generated for each respective solution. The transfer function is computed relative to free field radiation at 1 m. The conversion of the transient impulse response, Eq. (4.3), to the frequency domain is conducted by a Fast Fourier Transform, through a MATLAB subroutine. The transfer function relative to free field radiation at 1 m is computed as,

$$\mathrm{TF} = 20\log_{10}(|H|), \tag{4.19}$$

where H is either the complex frequency response of the impulse response, or the summation of Green's functions from Eqs. (4.10) and (4.12).

Figure 4.6 compares the adaptive tetrahedral tracing and edge diffraction results

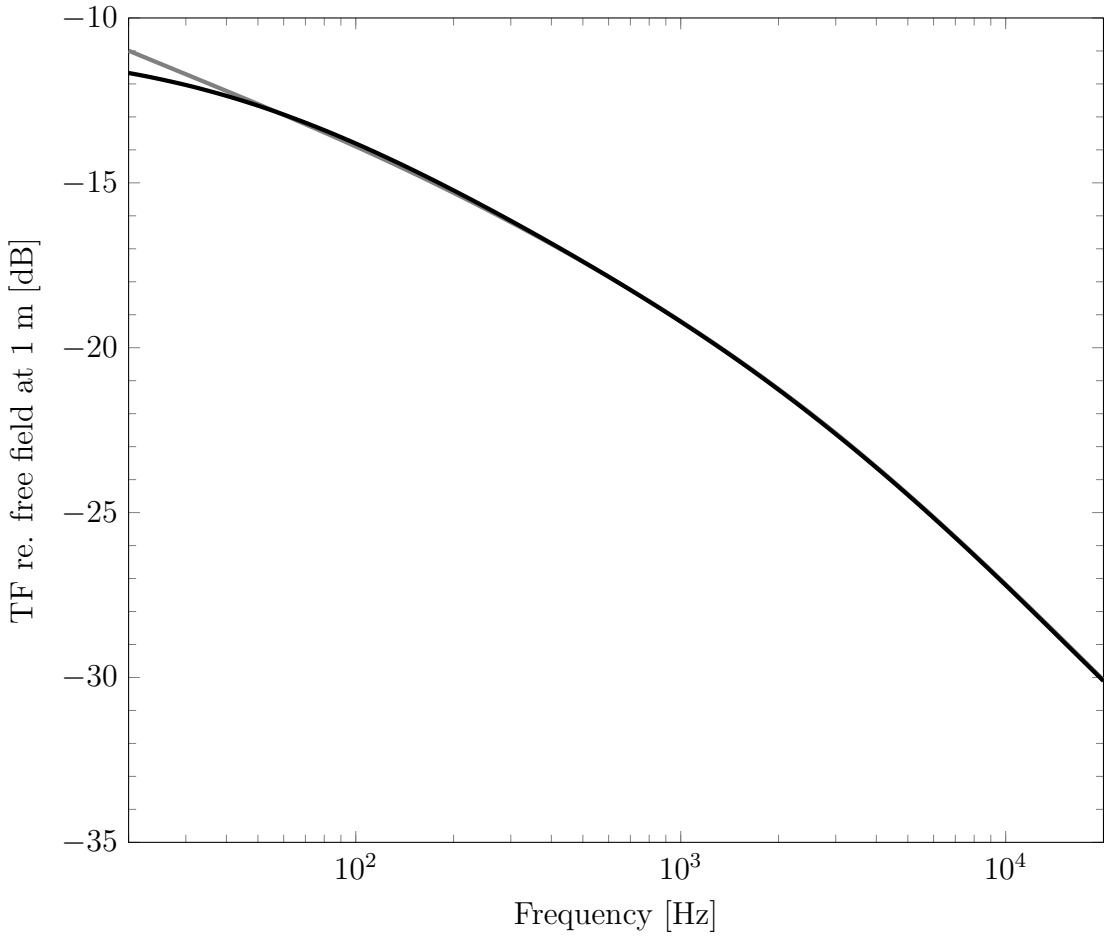

Figure 4.6: Frequency response due to a monopole source located at ($r_S = 1$, $\theta_S = 4\pi/3$, $z_S = 0$) and a receiver located at ($r_R = 3$, $\theta_R = \pi/4$, $z_R = 0$) in the vicinity of a rigid right angled wedge, with closed wedge angle, $\pi/2$. Adaptive tetrahedral tracing with edge diffraction (black curve) compared against Pierce's formulation (gray curve).

against Pierce's formulation. A very good agreement between the two methods is evident for a wide frequency range. Deviation between the two approaches is apparent for low frequencies, which is expected since Pierce's formulation is an asymptotic solution with greater accuracy at high frequencies. The inherent assumption in Pierce's formulation is that the source and receiver are at a distance from the wedge much greater than a wavelength. From this comparison it is clear that the tetrahedral tracing algorithm is able to identify the diffracting edge and pass along the wedge parameters to the secondary source model for edge diffraction.

4.4.2 Rigid Panel

Acoustic scattering of a rigid panel, 3.6 m wide, is compared between the adaptive tetrahedral tracing edge diffraction method and BEM results (Cox and D'Antonio, 2011). An array of 37 receivers surround the panel, separated at five degree intervals, 50 m away from the center of the panel. A source is normal to the panel center and 100 m away. The source and receiver configuration correspond to BEM calculations (Cox and D'Antonio, 2009, p. 134). The length of the scattering panel is set to 20 m long in order to compare three-dimensional results (adaptive tetrahedral tracing and edge diffraction) against two-dimensional results (BEM).

The BEM calculations are based on the thin-panel assumption applied to the Kirchhoff-Helmholtz equation; see Eq. (2.23). The thin-panel assumption casts the problem in terms of pressure differences and pressure sums across the thin panel. The derivative of Eq. (2.23) is used with the original equation in order to simultaneously solve for pressures at the front and back of a surface (Terai, 1980). The thin-panel BEM is based on Eqs. (2.29)–(2.31).

A comparison of the adaptive tetrahedral tracing edge diffraction method with the BEM is made across one-third octave bands. One-third octave band spectra are computed by a conversion of frequency points corresponding to 1/18-octave band center frequencies to 1/3-octave band spectra. The 1/18-octave band center frequencies are computed according to a base ten system (S1, 1986),

$$f_m = f_r(U^k), \tag{4.20}$$

where f_m is the center frequency of each 1/18-octave band, f_r is the reference frequency (1000 Hz), k is an integer value, and the frequency ratio U is,

$$U = 10^{(3b/10)}, \tag{4.21}$$

where $b = 1/18$ is known as the bandwidth designator, hence the 1/18-octave band designation. The integer k ranges from -63 to 57 (121 discrete frequencies) such that each 1/3-octave band spectra is based on a conversion from 1/18-octave band center frequencies according to the following sum (Long, 2006, p. 60),

$$L(f_{1/3}) = 10 \log_{10} \sum_{i}^{'} 10^{L_i(f_{1/18})/10}, \tag{4.22}$$

where L is the level at either 1/3-octave band center frequencies, $f_{1/3}$, or 1/18-octave band center frequencies, $f_{1/18}$, and the prime in the summation indicates the sum is over seven 1/18-octave band center frequencies centered about each 1/3-octave band center frequency.

Figure 4.7 shows six 1/3-octave band polar plots for the relative scattered level. The scattered acoustic pressure level is normalized to the maximum value and offset by 50 dB. The adaptive tetrahedral tracing edge diffraction method shows good agreement against the BEM results. Solutions deviate for large scattering angles at low frequencies. For example, the relative scattered level in the 100 Hz 1/3-octave band at a scattering angle of 90° (also −90°) exhibits a 13.1 dB discrepancy between the two prediction methods. Normally, for large scattering angles several orders of diffraction must be computed in order to minimize the error of the computed sound field (Chu et al., 2007). At middle to high frequencies the discrepancy between the relative scattered levels decreases. The difference at the extreme scattering angles for the 1000 Hz 1/3-octave band is 6.3 dB and for the 8000 Hz 1/3-octave band 0.5 dB. As the frequency increases higher-order diffractions have less of a contribution to the scattered sound field. The spatial distribution of the scattered sound field is also indicative of the acoustic wave interaction. For very low frequencies the wavelength is large relative to the characteristic dimensions of the panel. As a result for large wavelengths the scattering of the rigid panel becomes more hemispherical,

resembling point scattering. For higher frequencies a single strong lobe is generated indicative of the strong specular reflection in the normal direction. The lobe broadens as the frequency decreases due to the increasing influence of diffraction.

The root-mean-square error (RMSE) is computed between the adaptive tetrahedral tracing edge diffraction method and the BEM. The RMSE is computed as,

$$RMSE(f_{1/3}) = \sqrt{\left\{\sum_{i=1}^{N}\left[L_{ATTED}(f_{1/3}) - L_{BEM}(f_{1/3})\right]^2\right\}/N}, \tag{4.23}$$

where $N = 37$ is the total number of receivers, L_{ATTED} is the 1/3-octave band spectra for the adaptive tetrahedral tracing edge diffraction method, and L_{BEM} is the 1/3-octave band spectra for the BEM. One-third-octave bands ranging from 100 Hz to 8000 Hz, with various orders of diffraction included in the calculation are shown in Table 4.1. Generally, the RMSE increases as the frequency decreases. The result is expected since the inclusion of a finite number of diffraction orders results in an approximation of the acoustic field. The inclusion of higher orders of diffraction results in lower RMSE values, which is expected since the approximate solution converges to the actual sound field by including higher orders of diffraction. However, little to no reduction in the RMSE is evident by the inclusion of third-order diffraction. Compared to the peak magnitude of second-order diffraction, third-order diffraction is two orders of magnitude smaller. However, a systematic error may be present due to neglecting slope diffraction. Depending upon the accuracy required, and the problem geometry, calculations including first- or second-order diffraction may suffice.

4.4.3 Triangular Diffusor

Acoustic scattering of a geometric diffusor is compared between the adaptive tetrahedral tracing edge diffraction method and the BEM (Cox and D'Antonio,

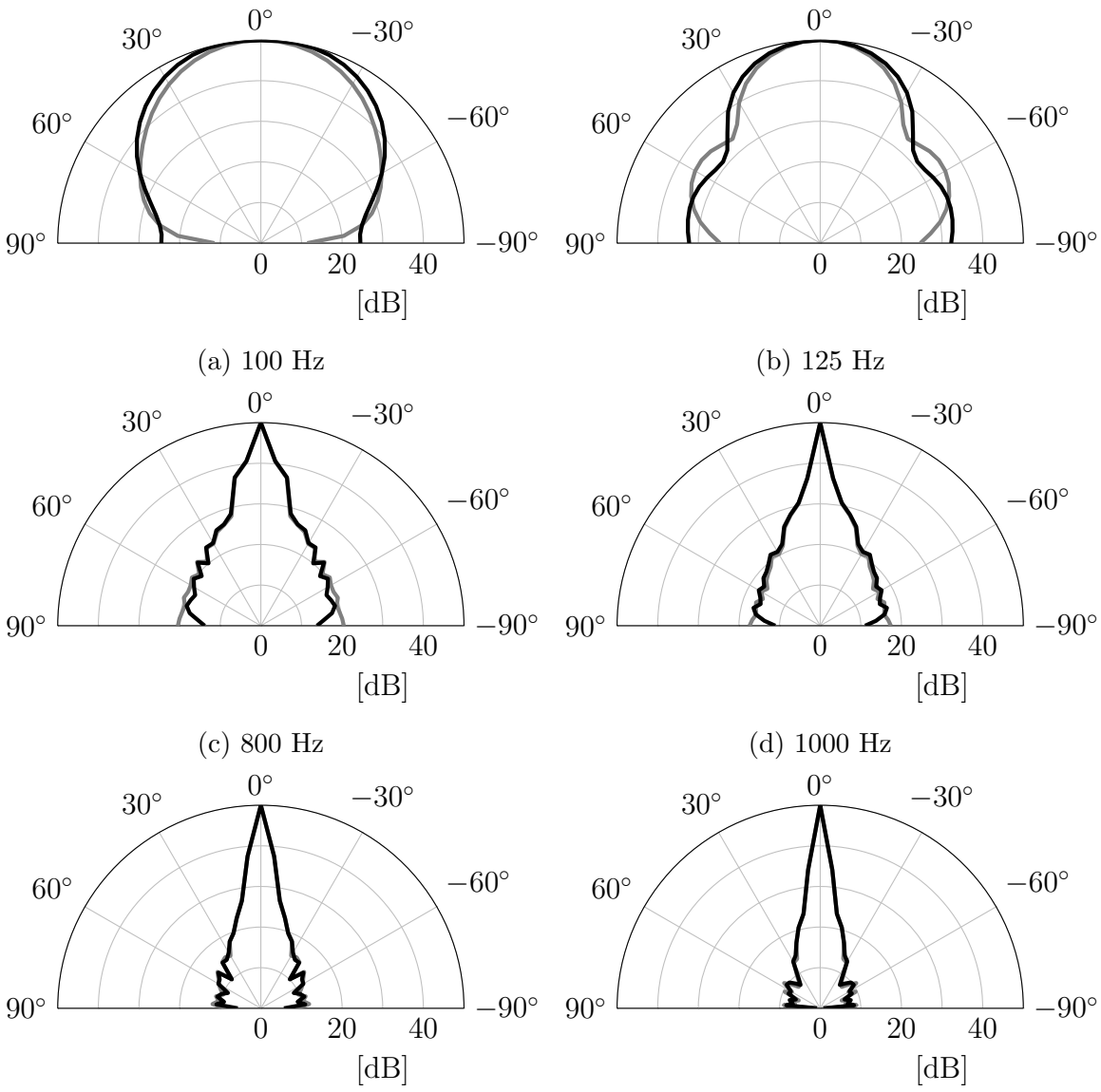

(a) 100 Hz

(b) 125 Hz

(c) 800 Hz

(d) 1000 Hz

(e) 6300 Hz

(f) 8000 Hz

Figure 4.7: Relative scattered levels for a rigid panel are compared between adaptive tetrahedral tracing edge diffraction results (black curve) and BEM results (gray curve). The source is normal to the panel. One-third octave band results are shown in (a) through (f). Up to third-order diffraction is included.

Table 4.1: Root-mean-square error (RMSE) of the relative scattered pressure levels for rigid panel scattering between the adaptive tetrahedral tracing edge diffraction model and the BEM. Source is normal to finite panel.

	RMSE [dB]		
1/3 Octave Band [Hz]	Diffraction Order Included		
	First	Second	Third
100	5.9	3.4	3.5
125	4.4	3.2	3.1
160	3.7	2.4	2.4
200	2.4	2.3	2.4
250	1.5	1.0	1.0
315	1.2	1.7	1.7
400	1.6	2.4	2.4
500	1.5	2.2	2.2
630	1.9	2.7	2.7
800	1.2	2.1	2.0
1000	0.8	1.7	1.7
1250	1.1	0.9	0.9
1600	2.4	1.5	1.6
2000	1.0	0.9	0.9
2500	1.2	1.6	1.6
3150	1.6	1.0	1.0
4000	0.6	1.0	1.0
5000	0.6	1.5	1.4
6300	0.8	0.9	0.9
8000	1.1	0.6	0.6

2011). The geometric diffusor is a triangular diffusor that is 3.66 m wide with three periods of triangles. Each triangular profile forms an isosceles triangle with two congruent angles of 18° at the base of each triangle. The choice of a triangular diffusor is motivated by the fact that multiple specular reflections occur and the the effect of omitting certain permutations of diffraction is illustrated.

Figure 4.8 shows six 1/3-octave band relative scattered levels for the triangular diffusor. In this particular case the source is oblique to the normal by 57°. The overall character of the acoustic scattering is captured at low frequencies; however, large discrepancies are evident. The reason for the discrepancy must be due to the omission of certain diffraction permutations. Second-order diffraction that is the result of one edge scattering event, a reflection, and another edge scattering event may be particularly important for this geometry. As the frequency increases the agreement improves for the adaptive tetrahedral tracing edge diffraction method. It is interesting to note that the main scattering lobe at low frequencies corresponds to the specular reflection angle; however, a stronger lobe away from the specular angle exists at higher frequencies. The strong scattering in the direction of $-20°$ and $-90°$ is due to the geometry of the triangular profiles. For a normally incident sound field the primary lobes occur at 36° and $-36°$, which is twice the acute angle of each triangle (Cox and D'Antonio, 2009, p. 340). For an oblique incident sound field it is expected that the lobes have the same relative position with respect to the scattering angle, which is confirmed in Figs. 4.8(e) and 4.8(f). Based on a separation of 36° from the specular angle it is expected the main lobes to appear at $-21°$ and $-93°$. According to Figs. 4.8(e) and 4.8(f) it can be seen that the main lobes correspond to what is expected geometrically.

The root-mean-square error (RMSE) is computed between the adaptive tetrahedral tracing edge diffraction method and the BEM. One-third octave bands ranging from 100 Hz to 8000 Hz, with various orders of diffraction included in the

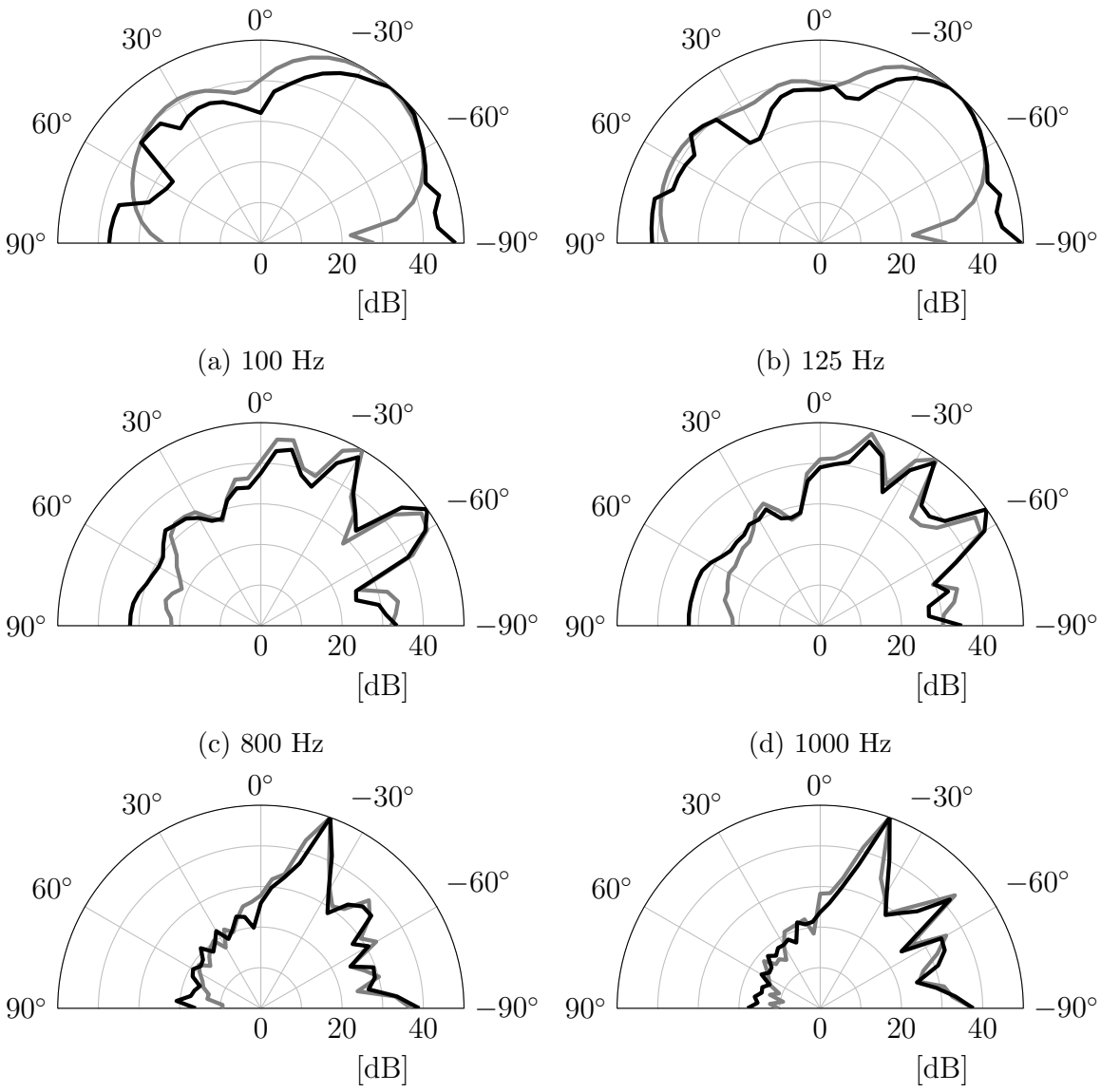

(a) 100 Hz

(b) 125 Hz

(c) 800 Hz

(d) 1000 Hz

(e) 6300 Hz

(f) 8000 Hz

Figure 4.8: Relative scattered levels for a rigid triangular diffusor are compared between adaptive tetrahedral tracing edge diffraction results (black curve) and BEM results (gray curve). The source is oblique to the normal at 57°. One-third octave band results are shown in (a) through (f). Up to second-order diffraction is included.

calculation are shown in Table 4.2. Generally, the RMSE increases as the frequency decreases. The result is expected since the inclusion of a finite number of diffraction orders results in an approximation of the acoustic field. Compared to the rigid panel, Table 4.1, the RMSE at high frequencies is consistently 2 dB above. The inclusion of higher orders of diffraction generally results in lower RMSE values; however, for very low frequencies inclusion of third-order diffraction increases the RMSE. This artifact must be due to physically incorrect diffraction paths computed according to the enumeration procedure in Sec. 4.2. For mid- to high-frequency computations the adaptive beam tracing edge diffraction method is well-suited for diffusor scattering prediction.

Table 4.2: Root-mean-square error (RMSE) of the relative scattered pressure levels for rigid triangular diffusor scattering between the adaptive tetrahedral tracing edge diffraction model and the BEM. Source is oblique with an angle of incidence 57°.

	RMSE [dB]		
1/3 Octave	Diffraction Order Included		
Band [Hz]	First	Second	Third
100	9.8	7.3	8.9
125	9.3	6.1	8.2
160	10.0	5.5	6.8
200	10.3	5.4	5.7
250	8.1	4.8	4.3
315	7.1	3.6	3.3
400	6.5	4.4	4.1
500	7.0	4.3	4.6
630	6.1	4.1	4.5
800	4.8	4.3	4.8
1000	4.7	4.5	4.4
1250	5.0	5.2	4.9
1600	3.8	3.8	3.8
2000	3.6	3.4	3.1
2500	3.7	3.3	3.2
3150	3.6	3.3	3.3
4000	3.4	3.3	3.2
5000	3.2	3.0	3.0
6300	3.3	3.3	3.3
8000	3.0	3.0	3.0

4.5 Summary

The compatibility of the adaptive tetrahedral tracing algorithm is based upon a link that exists between the acoustic mapping and the identification of edge diffraction. It was shown how wedge parameters are extracted from the acoustic mapping and passed along to the secondary source model for edge diffraction. Higher-order diffraction requires a procedure to enumerate the multitude of diffraction paths. Utilizing the concept of a directed graph and modified graph searching algorithms the multitude of higher-order diffraction paths are identified. The process of adaptive tetrahedral tracing results in determining the geometric acoustic field. The diffracted sound field is computed by the secondary source model for edge diffraction. The digital synthesis of an impulse response is considered as a linear combination of the free-field radiation, geometric acoustics, and diffracted sound. Fractional delays corresponding to exact arrival times are handled by a third-order Lagrange interpolator. Finally, numerical verification of the combined adaptive tetrahedral tracing algorithm and secondary source model for edge diffraction is based upon three test cases. The scattering characteristics of a rigid right-angled wedge, rigid panel, and rigid triangular diffusor are compared against analytic and BEM results. It is shown that the adaptive tetrahedral tracing edge diffraction method is particularly well-suited to compute the scattering characteristics of a panel and triangular diffusor at mid- to high-frequencies.

Chapter 5

Goniometer Measurements

The measurement of the scattered impulse response for a diffusor is accomplished with an instrument known as a goniometer. The principle of the diffusor measurement is based on estimating the scattered impulse response by deconvolving the loudspeaker-microphone transfer function from the subtracted impulse response. The subtracted impulse response is a subtraction of the impulse response with the diffusor present, and without the diffusor present. The subtraction is conducted in order to eliminate the direct sound.

In the present study a boundary layer goniometer is employed for the measurement of acoustic diffusors. The instrument is a fixed semicircular microphone array with a diffusor at the center of the array and a loudspeaker outside of the array emitting an interrogating signal; see Fig. 5.2. Two types of stimuli are tested: a maximum length sequence (MLS) and a logarithmic swept-sine (LSS). The merits of either signal are compared and contrasted.

Section 5.1 introduces the theoretical concepts that form the basis of a goniometer measurement. The signal processing involved in the measurement procedure are shown to produce an estimate of the scattered impulse response of an acoustic diffusor. In Sec. 5.2 the specific instrumentation of the goniometer is

described. The arrangement of the measurement apparatus is shown in detail. A comparison between measured polar responses and predicted polar responses, by the adaptive tetrahedral tracing edge diffraction method, are given in Sec. 5.3. Lastly, a summary is given in Sec. 5.4.

5.1 Theoretical Aspects of a Goniometer Measurement

A goniometer is a multi-microphone array that measures the scattered signal of a diffusor excited by a single loudspeaker. In order to arrive at the scattered polar response, the scattered impulse response must be estimated from the measurement. Three essential measurements are necessary for estimating the scattered impulse response (Cox and D'Antonio, 2009, pp. 111-121). The first measurement is the loudspeaker-to-microphone measurement. The purpose of the loudspeaker-to-microphone measurement is to characterize the transfer path between the loudspeaker and each microphone. This measurement captures the magnitude and phase distortion introduced by the measurement equipment. The second measurement, called the sample measurement, is conducted with the diffusor placed at the center of the microphone array. In this measurement the direct and scattered signals are measured by the array. The third measurement, called the background measurement, is conducted with no diffusor present. This last measurement captures the direct signal measured by the array. Each of these measurements is fundamental to estimating the scattered impulse response.

5.1.1 Estimation of the Scattered Impulse Response

It is important to stress that the scattered impulse response is an estimated impulse response. Analysis of the measured signals in the discrete-time domain show how

the scattered impulse response is estimated. In discrete-time the measured sample response is denoted as (Hayes, 1996, p. 369),

$$q_s[n] = r[n] * h_s[n] + w_s[n], \tag{5.1}$$

where n is the discrete-time sample index, q_s is the measured sample response, r is the loudspeaker-to-microphone response for a given excitation signal, h_s is the sample impulse response, w_s is additive noise during the sample measurement, and the $*$ operator denotes discrete-time convolution. The loudspeaker-to-microphone response is based upon a convolution of the excitation signal and the loudspeaker-to-microphone response,

$$r[n] = s[n] * g[n], \tag{5.2}$$

where s is the excitation signal, and g is the loudspeaker-to-microphone impulse response. Similar to the sample measurement the background measurement response is given as,

$$q_b[n] = r[n] * h_b[n] + w_b[n], \tag{5.3}$$

where q_b is the measured background response, h_b is the background impulse response, and w_b is the additive noise during the background measurement. The sample impulse response is computed exactly by deconvolving the loudspeaker-to-microphone response after subtracting the noise from the sample response,

$$h_s[n] = r^{-1}[n] * (q_s[n] - w_s[n]), \tag{5.4}$$

where r^{-1} is the inverse filter of the loudspeaker-to-microphone response satisfying the following relationship,

$$r^{-1}[n] * r[n] = \delta[n] \tag{5.5}$$

where δ is the Kronecker delta function. Similarly the background impulse response is computed exactly by a deconvolution,

$$h_b[n] = r^{-1}[n] * (q_b[n] - w_b[n]). \tag{5.6}$$

The scattered impulse response is determined exactly by subtracting the sample impulse response, Eq. (5.4), from the background impulse response, Eq. (5.6),

$$h_{sc}[n] = h_s[n] - h_b[n] = r^{-1}[n] * (q_s[n] - q_b[n]) + r^{-1}[n] * (w_b[n] - w_s[n]), \tag{5.7}$$

where h_{sc} is the scattered impulse response.

In practice it is assumed the additive noise in the sample and background measurements is negligible (AES Standards Committee, 2001). If the signal-to-noise ratio is high enough, then neglecting noise is a reasonable assumption. The subtraction process does not completely eliminate the direct and reflected sound due to time-variance. Instead, the process decreases the contributions of direct and reflected sound within the scattered impulse response. A rectangular weighting is then applied to the time region when sound scattering occurs in order to eliminate to a large extent the direct and reflected sound residuals in the subtracted impulse response. Hence, the scattered impulse response is estimated as,

$$\hat{h}_{sc}[n] = w[n](\hat{h}_s[n] - \hat{h}_b[n]) = w[n] \left(r^{-1}[n] * (q_s[n] - q_b[n]) \right), \tag{5.8}$$

where $w[n]$ is a rectangular weighting applied to time samples when acoustic scattering is present, and the hat above each impulse response indicates an estimate of the impulse response. Furthermore, the processing of each measured signal is generally conducted in the frequency domain. For example, the estimated scattered impulse response is computed in the discrete frequency domain by a N-point

discrete Fourier transform (DFT) of the respective signals,

$$\hat{H}_{sc}[k] = \frac{Q_s[k] - Q_b[k]}{R[k]} = \frac{Q_s[k] - Q_b[k]}{S[k]G[k]} \qquad \text{for } k = 0,...,\text{N - 1}, \tag{5.9}$$

where the index k corresponds to discrete frequencies. Caution must be exercised when conducting a deconvolution in the time-domain. Due to the inherent periodicity of the DFT, the number of points of the DFT, N, must be at least equal to the signal length of the subtracted measurements plus the signal length of the loudspeaker-microphone response. The scattered impulse response is then computed by an inverse DFT of the result in Eq. (5.9). It is preferred to process the signals in the frequency domain since the division operation effectively deconvolves the signal(s) in the denominator, which is a faster operation by the Fast Fourier Transform (FFT) than by deconvolution in the discrete-time domain (Oppenheim et al., 1999, p. 655).

An important consideration in measuring the scattered signal is the necessary condition for recovering the scattered impulse response. The arrangement of a loudspeaker, microphone array, and an acoustic diffusor within a testing space must be such that no reflections contaminate the time window for acoustic scattering, and the direct to scattered signals are separated well enough in time. A quasi-anechoic setup was developed by D'Antonio and Konnert (1992) to satisfy this necessary condition. Later, the arrangement of the loudspeaker and microphone array was optimized to maintain a specific specular region width, and a quasi-anechoic condition (D'Antonio and Rife, 2011). Further details on the quasi-anechoic conditions are in Sec. 5.2.2.

5.1.2 Excitation Signal

The choice of excitation signal is particularly important for the estimation of the scattered impulse response. The ideal signal is broadband in nature, exhibits a high signal-to-noise ratio, and is short in length. Of the available excitation signals three general categories exist: periodic signals, transient, and non-transient aperiodic (Schoukens et al., 1988). Periodic signal types include stepped sinusoid, swept sine, multisine, periodic noise, maximum length binary sequence, and discrete interval binary sequence. Transient signal types include impulse and random burst. Lastly, an aperiodic signal is random noise. A comparison of all the signals mentioned above shows that deterministic signals such as the swept-sine, multisine, and maximum length binary sequence are very good at estimating the transfer function in the presence of a flat noise spectrum (Schoukens et al., 1988).

Early measurements of acoustic diffusors utilized a system employing time-delay spectrometry (TDS) (D'Antonio and Konnert, 1992). A single microphone was used for the measurement of a semicircular polar response. The excitation signal in a TDS measurement is a linearly swept-sinusoidal signal (Müller and Massarani, 2001). The principle behind the measurement technique is based on the modulation theorem (Oppenheim et al., 1999, pp. 61, 62). A delayed excitation signal is modulated with the received signal producing sum and difference products of the signal. If the delay corresponds to the acoustic path of the excitation signal from the loudspeaker, then the difference product is ideally at the DC frequency. Low-pass filtering removes the sum product from the frequency response, effectively isolating the frequency response of the acoustic diffusor. Some drawbacks of the technique include long measurement times and the delicate setting for the modulated signal delay (Poletti, 1988). After some time TDS was replaced in favor of an alternative excitation signal.

The maximum length sequence (MLS) is currently the excitation signal of choice

for acoustic diffusor measurement (D'Antonio, 1995, pp. 112, 113). The excitation signal is based on a binary sequence generated by a feedback shift register (MacWilliams and Sloane, 1976; Vanderkooy, 1994). A MLS is categorized as a psuedorandom periodic sequence. The signal length is dependent on the order of the feedback shift register,

$$L = 2^m - 1, \tag{5.10}$$

where m is the order number, and L is the periodic length of the sequence. The circular autocorrelation of an MLS signal is nearly a Kronecker delta function and the energy density spectrum of the circular autocorrelation is white, except at DC (Vanderkooy, 1994). The advantage of using an MLS signal is the broadband nature of the signal, and no need for averaging. Furthermore, when compared to TDS the use of an MLS signal allows quicker measurement times and better frequency resolution (Vanderkooy, 1994). If the noise spectrum in the measurement is not flat, then the MLS may be preemphasized in the frequency domain in order to achieve a uniform signal-to-noise ratio (Mommertz and Müller, 1995). Disadvantages associated with the use of a MLS signal include the nonuniform distribution of harmonic distortion in the recovered impulse response, the required fine tuning of the gain to minimize harmonic distortion and maximize the signal-to-noise ratio, sensitivity to time-variance, and the enhancement of harmonic distortion by averaging (Müller and Massarani, 2001; Vanderkooy, 1994). Since the harmonic distortion is non-uniformly distributed throughout the causal part of the impulse response, it contaminates the estimated impulse response without remedy (Vanderkooy, 1994).

Another measurement signal well-suited for acoustic diffusor measurement is the logarithmic swept-sine (LSS). Similar to the linear swept-sine the logarithmic swept-sine is a frequency modulated sinusoidal signal with advantageous properties. The advantages of a LSS signal include a higher signal-to-noise ratio compared to

MLS, advancing in time harmonic distortion, and a greater insensitivity to time-variance (Farina, 2000; Müller and Massarani, 2001). The discrete-time representation of the LSS is (Farina, 2000; Stan et al., 2002),

$$s[n] = A\sin\left(\frac{N\omega_i}{f_s\log(\omega_f/\omega_i)}\left[e^{n\log(\omega_f/\omega_i)/N} - 1\right]\right) \qquad \text{for } n = 0,...,\text{N - 1}, \qquad (5.11)$$

where N is the total number of samples for the signal, f_s is the sampling frequency, ω_i is the initial sweeping frequency in radians per second, and ω_f is the final sweeping frequency. The energy density spectrum of the LSS has a negative slope of 3 dB per doubling of frequency, known as a pink frequency spectrum. The pink frequency spectrum of the LSS is beneficial when conducting measurements in an environment with a noise spectrum that increases for lower frequencies. The harmonic distortion products of a measurement are advanced in time from the recovered impulse response by a linear deconvolution of the input signal (Müller and Massarani, 2001). The recovered impulse response is windowed to eliminate the harmonic distortion.

In the present study both the MLS and LSS signals are used to estimate the scattered impulse response of acoustic diffusors. A comparison of the two excitation signals is given in Sec. 5.3.

5.2 Measurement Setup

5.2.1 Measurement Equipment and Arrangement

The experimental setup of the goniometer consists of a desktop computer, a bank of four multichannel microphone preamplifiers, a power amplifier, a loudspeaker, a 32 microphone array, and a measurement platform; see Fig. 5.1. The desktop computer is an HP Compaq 6200 Pro SFF PC with a quad-core Intel i5-2400 central

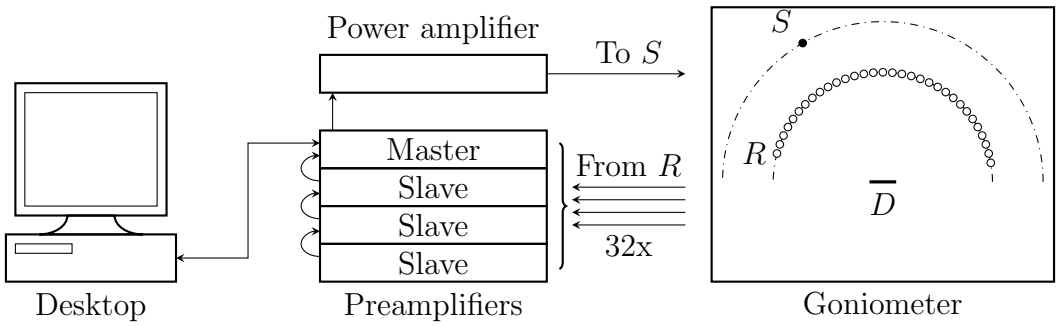

Figure 5.1: Schematic of experimental arrangement for acoustic diffusor testing. The desktop computer relays an excitation signal to the master preamplifier, the preamplifier outputs the signal to the power amplifier, and the signal is reproduced by the loudspeaker at S. The 32 electret condenser microphones, R, are connected to each multichannel preamplifier in groups of eight. The preamplifiers are arranged in a master-slave relationship as shown and digitally acquire the recorded signal with 24 bits of encoding at a sampling frequency of 48 kHz relaying the digital signals to the measurement desktop. During a sample measurement, an acoustic diffusor D is placed at the center of the microphone array of the goniometer.

processing unit having a clock frequency of 3.1 GHz, eight gigabytes of random-access memory, and a 64-bit Windows 7 operating system. The audio recording software is a package entitled Reaper, version 4.261/x64. Post-processing software was written in MATLAB, version 7.8.0 (R2009a). Each microphone preamplifier is a Motu 8 Pre which contains eight channels providing 48 V of phantom power to each condenser microphone. The preamplifiers are linked together in a master-slave relationship with one master preamplifier and three slave pre-amplifiers. The preamplifiers also work in tandem with the measurement desktop to acquire signals with 24-bit encoding at a sampling frequency of 48 kHz. The power amplifier is a Hafler P1000 amplifier, which delivers the excitation signal to the loudspeaker via the master preamplifier. The loudspeaker is a Bose Jewel Cube loudspeaker with a two inch driver. Each microphone is a Crown GLE-100 electret condenser microphone. The microphones have an omnidirectional polar pattern. The measurement platform is 0.21 m thick MDF measuring 4.53 m by 3.63 m.

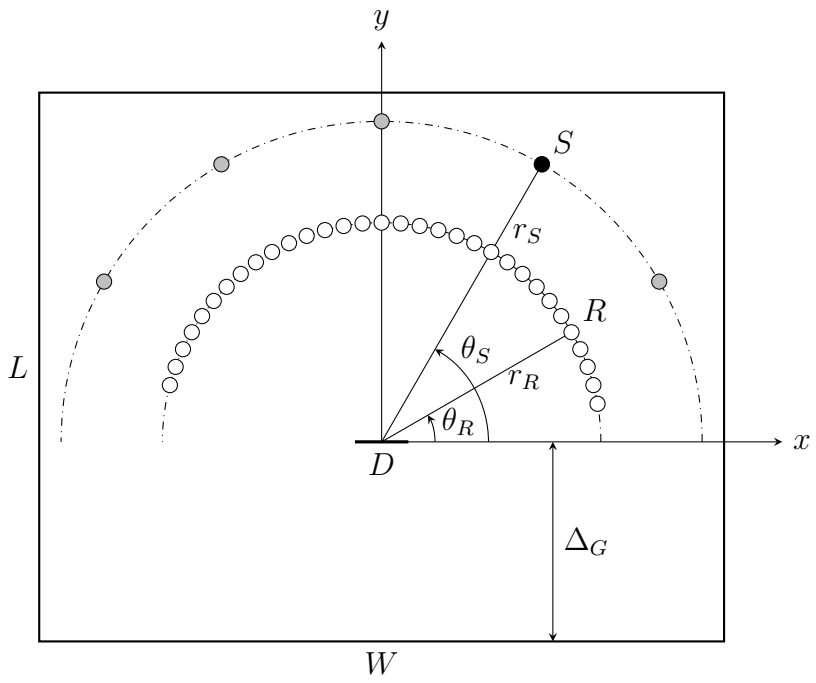

Figure 5.2: The goniometer is arranged on a measurement platform measured $W = 4.53$ m by $L = 3.63$ m. Thirty-two microphones are placed on an arc with radius $r_R = 1.45$ m. The microphones have angular positions θ_R ranging from 10° to 165° separated by 5° increments. The source is placed on an arc with radius $r_S = 2.12$ m. The source is placed at one of the angular positions θ_S ranging from 30° to 150° separated by 30° increments. The microphone array is displaced from the rear of the measurement platform by $\Delta_G = 1.32$ m.

On top of the measurement platform is situated the microphone array, loudspeaker, and acoustic diffusor during the sample measurement; see Fig. 5.2. The microphone array is comprised of 32 microphones arranged in a semicircular arc. The radius of the array is 1.45 m. Microphones are positioned at angular positions starting from 10° to 165° spaced in 5° increments. The center point of the arc is 1.32 m from the rear of the platform and centered along the width of the platform. The loudspeaker is placed in one of five angular positions pointing towards the center of the microphone array. Each position is situated at a radial distance of 2.12 m and the angular positions are separated by 30° starting from 30° and terminating at 150°. The front midpoint of an acoustic diffusor is centered in the microphone array during a sample measurement.

5.2.2 Quasi-anechoic Conditions

As mentioned in Sec. 5.1.1 it is important that the scattered signal be conducted under quasi-anechoic conditions. A quasi-anechoic condition is satisfied if the scattered signal is captured in a time window free of direct sound and room reflections. The concept of applying a quasi-anechoic measurement for acoustic diffusors was pioneered by D'Antonio and Konnert (D'Antonio and Konnert, 1992). The original conception of a quasi-anechoic measurement is based upon an equivalent idea called the reflection free zone (Cox and D'Antonio, 2009, pp. 113, 114). Ideally, direct sound precedes the onset of the scattered signal by two milliseconds and room reflections proceeds the onset of the scattered signal by two milliseconds. The original goniometer geometry could not sufficiently separate the direct and scattered signals for large scattering angles (D'Antonio and Konnert, 1992). By a process of refinement and lately through numerical optimization the geometric configuration of the goniometer evolved to the present configuration shown in Fig. 5.2 (D'Antonio and Rife, 2011).

The quasi-anechoic conditions are analyzed by geometric considerations. The quasi-anechoic boundary is a surface in space beyond which room reflections occur two milliseconds after the onset of the scattered signal. Each source to microphone has a different quasi-anechoic boundary. The derivation of the geometric parameters for each quasi-anechoic boundary is based upon Fig. 5.3. It is understood that a source S has the polar coordinates (r_S, θ_S), and a receiver R has the polar coordinates (r_R, θ_R). A coordinate system is established with its origin at the center of the microphone array. In a sample measurement a diffusor D is placed at the origin. It can be assumed that the onset of the scattered signal occurs along a path from S to D and then D to R, which is denoted as $\overrightarrow{SDR}$. In order to determine the quasi-anechoic boundary, it is desired to first compute the corresponding elliptical parameters associated with the path $\overrightarrow{SDR}$. It is recognized that the foci of the

ellipse are S and R. The focal length is denoted as f where twice the focal length is equal to the distance between S and R, $|\overrightarrow{SR}| = 2f$. The center of the ellipse C is the midpoint of the path $\overrightarrow{SR}$. The interior angle associated with $\angle SDR$ is denoted as α. The interior angle is computed as the absolute difference between θ_R and θ_S,

$$\alpha = |\theta_R - \theta_S|. \tag{5.12}$$

By the law of sines the interior angle of $\angle DSR$ is computed as,

$$\beta = \arcsin[r_R \sin(\alpha)/2f], \tag{5.13}$$

where $\beta = \angle DSR$. The rotation angle of the ellipse is computed as,

$$\gamma = \begin{cases} \theta_S - \beta & \text{if } \theta_R - \theta_S \geq 0, \\ \theta_S + \beta & \text{if } \theta_R - \theta_S < 0. \end{cases} \tag{5.14}$$

By the properties of ellipsis the major and minor axis of the ellipse, which correspond to the rotated and translated coordinate system at C, are computed as,

$$a = \frac{r_S + r_R}{2}, \tag{5.15}$$

$$b = \sqrt{a^2 - f^2}, \tag{5.16}$$

where a and b are the lengths of the major and minor axis of the ellipse, respectively. The ellipse with the parameters computed from Eqs. (5.14)–(5.16) is shown as a black dashed ellipse in Fig. 5.3. In a large part the generated ellipse is dependent upon the path lengths from the source to diffusor and diffusor to receiver. In a like manner the quasi-anechoic boundary is based upon the path lengths from the source

to diffusor, diffusor to receiver, and a buffer distance based upon the buffer time,

$$d = c\tau, \tag{5.17}$$

where d is the buffer distance, c is the speed of sound, and τ is the buffer time (4 ms). The buffer time allows for time spreading due to surface scattering and an allowance for a time window free of reflections. The major axis and minor axis of the quasi-anechoic boundary is computed similarly to Eqs. (5.15) and (5.16) by considering the buffer distance,

$$a_{QA} = \frac{r_S + r_R + d}{2}, \tag{5.18}$$

$$b_{QA} = \sqrt{a_{QA}^2 - f^2}, \tag{5.19}$$

where a_{QA} and b_{QA} are the lengths of the major and minor axis of the quasi-anechoic boundary ellipse, respectively. It is important to note that the total quasi-anechoic boundary is a hemiellipsoid generated as a surface of revolution about the elliptical major axis. The quasi-anechoic boundary is denoted as a red dashed ellipse in Fig. 5.3. Thus, for no room reflections to occur within the buffer time window after the onset of scattering, no reflecting surfaces besides the diffusor can exist within the hemiellipsoid of the quasi-anechoic boundary. Another consideration is the time separation between the direct sound and the onset of scattering. The time separation is based upon the difference in the path lengths $\overrightarrow{SR}$ and $\overrightarrow{SDR}$. In general the buffer time of two milliseconds is satisfied by the goniometer configuration; however for some particular source and receiver angles the path length difference corresponds to less than the buffer time. For example, given a source position at 30° and a receiver at 165° the path length difference is 0.262 m, which is a 0.76 ms time difference between the direct and scattered sound.

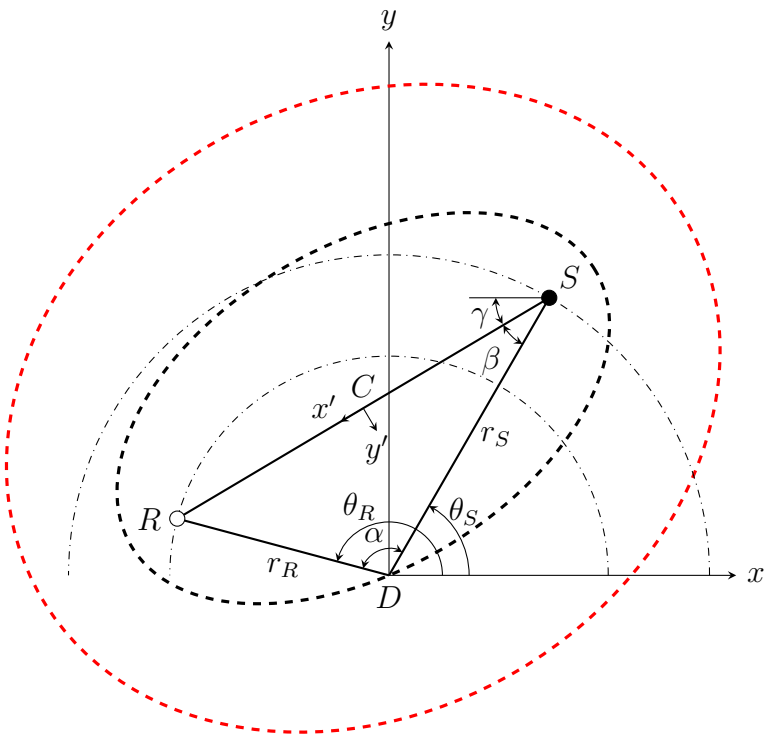

Figure 5.3: Quasi-anechoic conditions for the sample measurement. Geometry for the derivation of the quasi-anechoic boundary. The goniometer measurement consists of a diffusor located at D, one receiver of 32 shown as R, and the source S. The quasi-anechoic boundary, denoted as a dashed red ellipse, defines the extent of sound propagation from S, to a room reflection, and then to R two milliseconds after the onset of the scattered response ($\overrightarrow{SDR}$). The quasi-anechoic boundary is a hemiellipsoid in three-dimensional space being a surface of revolution about the major axis with a center at C. The hemiellipsoid has foci at S and R. The positions of the source and receiver are defined in terms of polar coordinates (r_S, θ_S), and (r_R, θ_R), respectively.

For room reflections to be delayed in time sufficiently ahead the onset of scattering, a clear distance must exist around and above the goniometer. Analysis of the quasi-anechoic boundary leads to the conclusion that the hemiellipsoid is largest when $\theta_R = \theta_S$. By Eq. (5.18) the major axis of the hemiellipsoid does not change, since the buffer distance and the radii of the source and receivers are constant. However, the minor axis of the hemiellipsoid changes based on a varying focal length; see Eq. (5.19). The focal length is a minimum when $\theta_R = \theta_S$. In the horizontal plane the quasi-anechoic boundary is shown in Fig. 5.4. Around the measurement platform exists a clear strip of space that is 1.37 m wide. In general this clear space prevents any room reflections from reaching the receiver within the buffer time. Vertically, the quasi-anechoic boundary extends to a maximum height equal to the minor axis of the ellipse, see Eq. (5.19). The height of the measurement room is 2.43 m and the maximum length of the minor axis is 2.40 m. Thus, the measurement room is sufficiently large to facilitate a quasi-anechoic measurement.

5.2.3 Excitation Signals

Two excitation signals are used with the goniometer. The traditional MLS is a 17^{th} order signal that is pre-emphasized. The signal was generated by the software EASERA version 1.2 (GmbH, 2012, p. 32). The transition frequency of the pre-emphasized MLS is approximately 350 Hz where the lower frequencies are emphasized relative to the higher frequencies. Since the MLS is a 17^{th} order signal by Eq. (5.10) the signal has a length of 131071 samples. At a sampling frequency of 48 kHz this translates into a signal duration of 2.73 seconds. The energy density spectrum of the MLS is shown in Fig. 5.5. The second excitation signal is a LSS. The signal length is comparable to the length of the MLS. The signal has a length of 131072 (2^{17}) samples. The initial sweep frequency is 80 Hz and the final sweep frequency is 24 kHz. The signal is filtered by a second-order Butterworth filter with

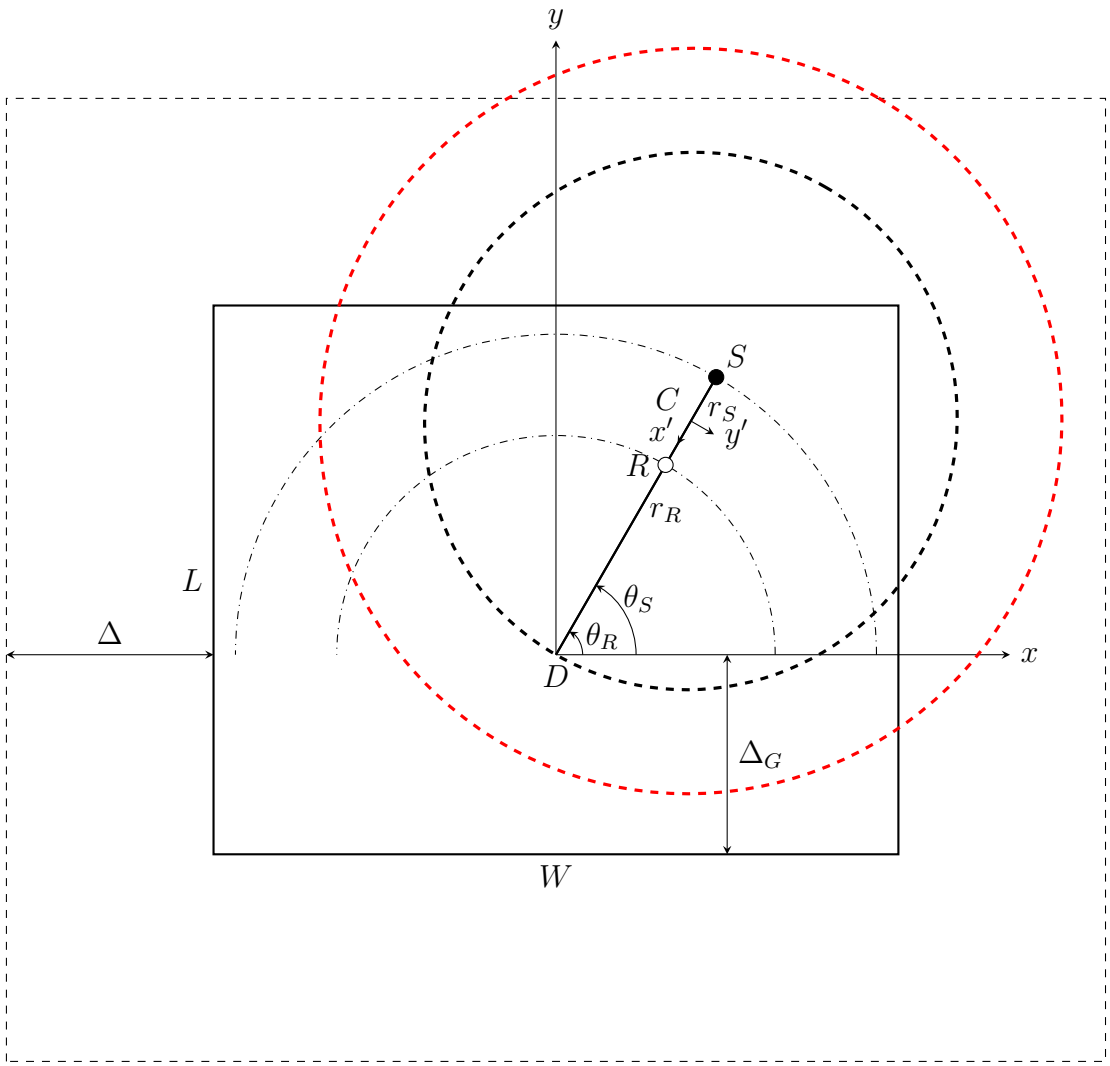

Figure 5.4: The quasi-anechoic boundary is largest when $\theta_R = \theta_S$. Here the goniometer is shown in the context of the measurement platform and a strip of free space surrounding the platform. The measurement platform has the following dimensions: $W = 4.53$ m by $L = 3.63$ m. The microphone array is displaced from the rear of the measurement platform by $\Delta_G = 1.32$ m and the strip of free space has a constant width of $\Delta = 1.37$ m. The walls of the measurement room are outside the strip of free space.

cutoff frequencies at 60 Hz and 23 kHz. The energy density spectrum of the LSS is shown in Fig. 5.5. The signal energy and energy density spectrum are defined as (Oppenheim et al., 1999, pp. 60, 621),

$$E = \sum_{i=0}^{N-1} |s[n]|^2 = \frac{1}{N} \sum_{k=0}^{N-1} |X[k]|^2, \tag{5.20}$$

where E is the signal energy, the signal is nonzero for the indices zero to $N-1$, and $|X[k]|^2$ is the energy density spectrum. The original intention was to have the signal energy of the LSS equivalent to the MLS signal. Significant distortion was observed during the emission of the LSS signal by the loudspeaker. Therefore, the energy of the LSS signal was reduced by decreasing the amplitude of the signal.

5.2.4 Diffusor Samples

A geometric diffusor and a number theoretic diffusor are the two diffusors of interest in this study. The geometric diffusor is formed by six periods of extruded triangular profiles; see Fig. 5.6(a). The cross-section of each profile is an isosceles triangle with the base measuring 52 mm and the height measuring 26 mm. The length of each triangular section is 314 mm. A square base is attached to the back of the six period assembly with a thickness of 19 mm. The number theoretic diffusor is a quadratic residue diffusor; see Fig. 5.6(b). Three periods of each quadratic residue diffusor form the complete assembly. The depth of each diffusor is 19 mm, and it is 120 mm square. A 6 mm backing plate holds the three diffusors together. The depths of the diffusor wells are based upon a seven-period quadratic residue sequence. The wells are proportional to the sequence of numbers 0, 1, 4, 2, 2, 4, and 1 (Cox and D'Antonio, 2009, p. 291). The well depth associated with the sequence number one is 4.6 mm. Each diffusor is constructed of different materials. The geometric diffusor is constructed of wood and the quadratic residue diffusor is

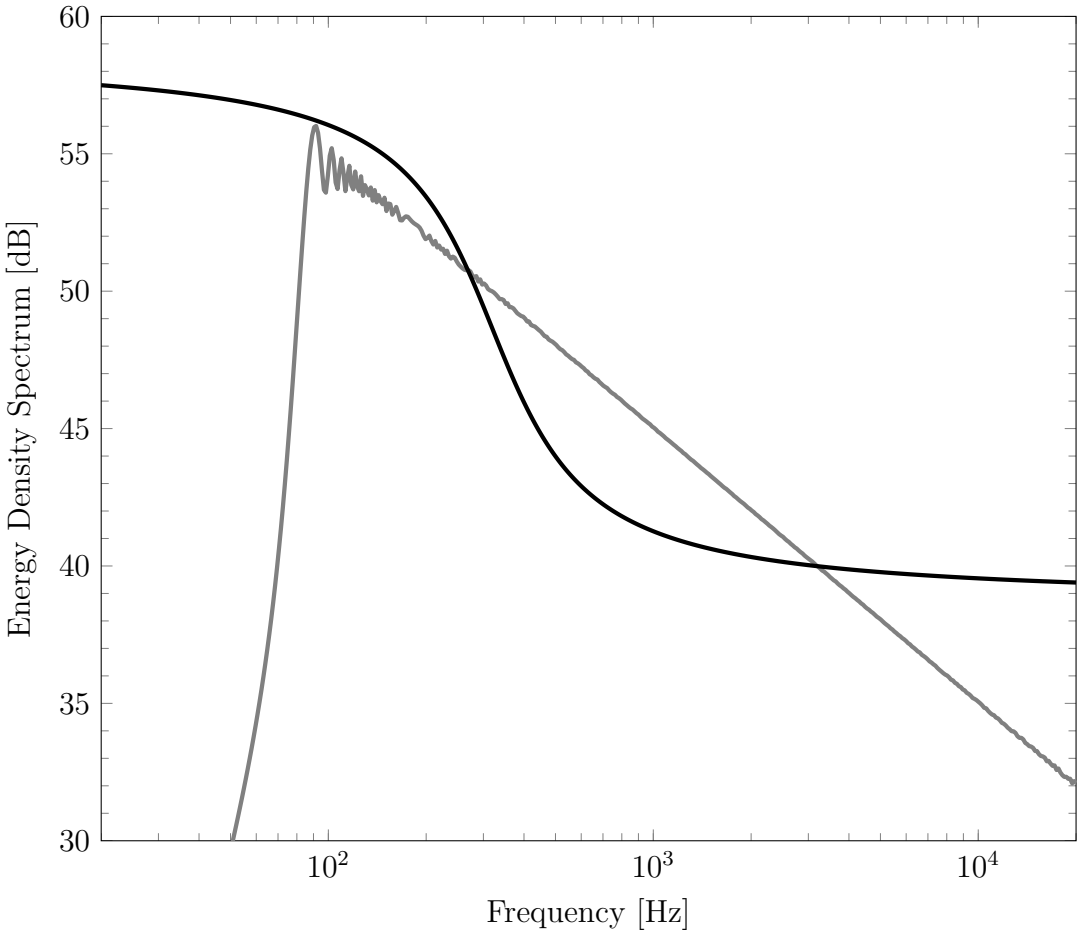

Figure 5.5: The energy density spectrum of a logarithmic swept-sine signal (gray curve) and a maximum length sequence signal (black curve).

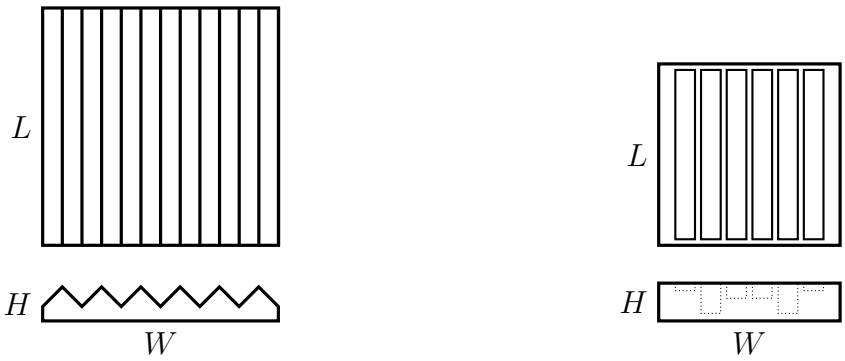

Figure 5.6: Geometry of a periodic triangular diffusor and a quadratic residue diffusor. (a) The overall dimensions of the periodic triangular diffusor are $W = 312$ mm, $L = 314$ mm, and $H = 45$ mm. (b) One period of the quadratic residue diffusor is illustrated. The overall dimensions are $W = 120$ mm, $L = 120$ mm, and $H = 25$ mm.

constructed of an epoxy-sealed gypsum powder. The backing plate for each diffusor assembly is medium-density fibreboard.

5.3 Measurement Results

The scattered impulse response of an acoustic diffusor is measured by a goniometer. The measurement is conducted at three angles of incidence (90°, 120°, and 150°) for symmetric samples and five angles of incidence (30°, 60°, 90°, 120°, and 150°) for an asymmetric sample. Since the triangular diffusor and quadratic residue diffusor are both symmetric samples three angles of incidence are measured. An experimental comparison of the MLS and LSS excitation signals is given. After, a comparison between prediction results, generated by the adaptive beam tracing edge diffraction model, and experimental results based on a MLS excitation is analyzed.

5.3.1 Signal Excitation Comparison

A MLS signal and a LSS signal are both used as stimuli for a goniometer measurement. Traditionally the MLS has found widespread application for

measuring the acoustic scattering of diffusors (D'Antonio, 1995, pp. 112, 113). More recently the LSS has found increasing use in the measurement of room impulse responses (Stan et al., 2002). It is of interest to compare the scattered polar responses derived from the scattered impulse responses.

Figs. 5.7 and 5.8 show the relative scattered polar plots of the triangular diffusor and quadratic residue diffusor for a select number of 1/3-octave band frequencies. The polar plots are nearly indistinguishable for 1/3-octave bands across the middle frequencies. For low frequencies inconsistent differences are apparent for the triangular diffusor. The results generated via a MLS excitation versus the results generated via a LSS excitation generally have slight differences except at the extreme ends of the audible frequency spectrum; refer to Figs. 5.7(a), 5.7(b), 5.8(d), and 5.8(e). It must be emphasized that the frequencies shown in Fig. 5.8 are frequencies scaled by a factor of five. The actual frequencies for the scaled diffusor are a factor of five higher than shown. It is conjectured that the primary differences in the 1/3-octave band frequencies shown is primarily due to the limited bandwidth of the LSS signal, or the relative differences in the spectral energy; refer to Fig. 5.5. Particularly, at the low and high ends of the frequency spectrum it is conceivable that major differences are expected for such large differences between the LSS signal spectrum and MLS signal spectrum. An additional factor is the very low signal to noise ratio available at the low end of the frequency spectrum. The driver of the loudspeaker is small enough to be a poor radiator of sound energy at low frequencies.

To quantify the relative differences of the scattered polar plots, the average relative difference is defined. The average relative difference is defined as,

$$ARD = \frac{1}{M}\sum_{i=1}^{M}\frac{L_{MLS,i} - L_{LSS,i}}{(L_{MLS,i} + L_{LSS,i})/2}, \tag{5.21}$$

where ARD is the average relative difference, $L_{MLS,i}$ is the relative scattered level

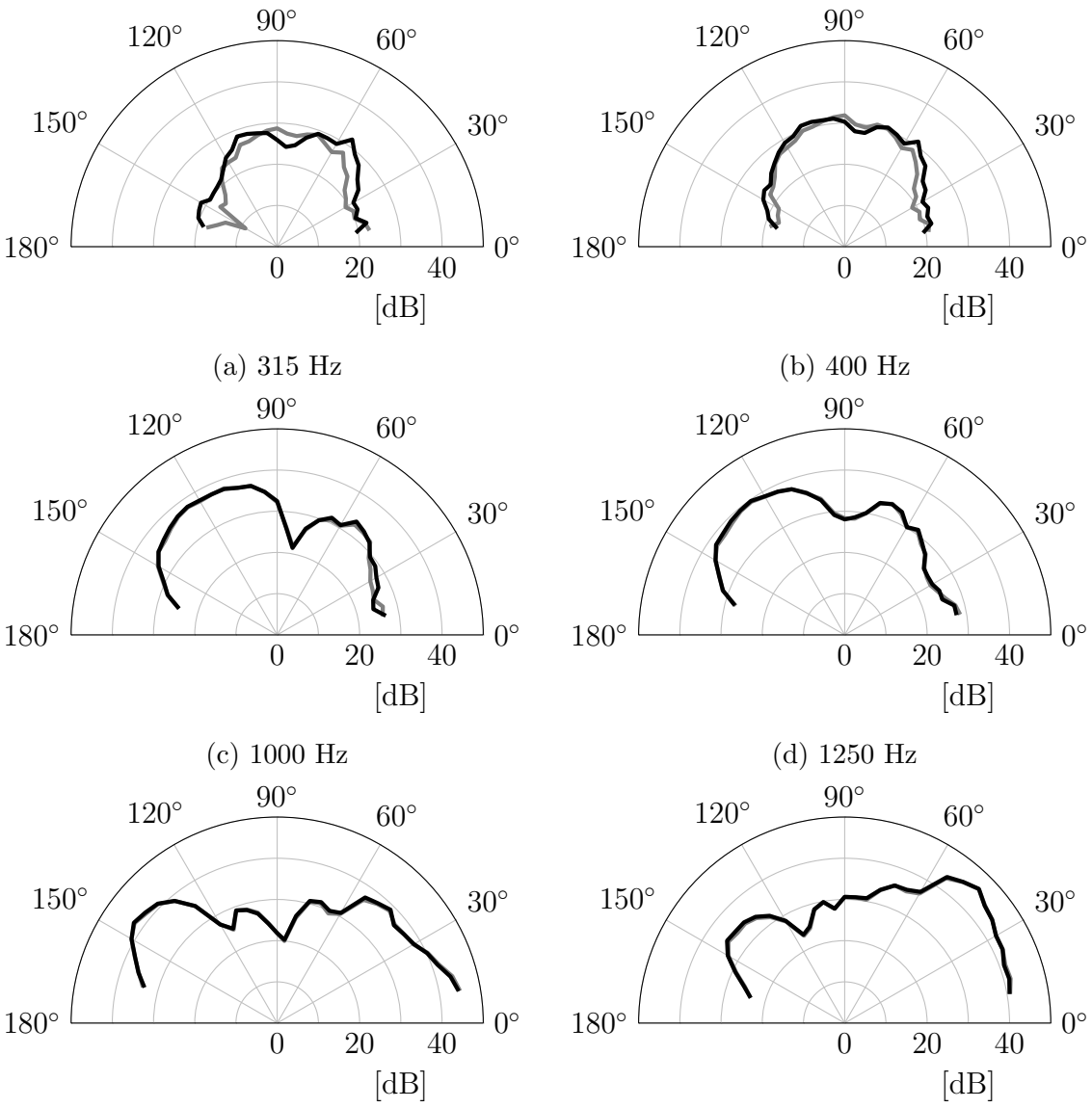

(a) 315 Hz

(b) 400 Hz

(c) 1000 Hz

(d) 1250 Hz

(e) 3150 Hz

(f) 4000 Hz

Figure 5.7: Experimental relative scattered levels for a triangular diffusor are compared between a MLS signal (black curve) and a LSS signal (gray curve). The source is incident from a polar angle of 30°. One-third octave band results are shown in (a) through (f).

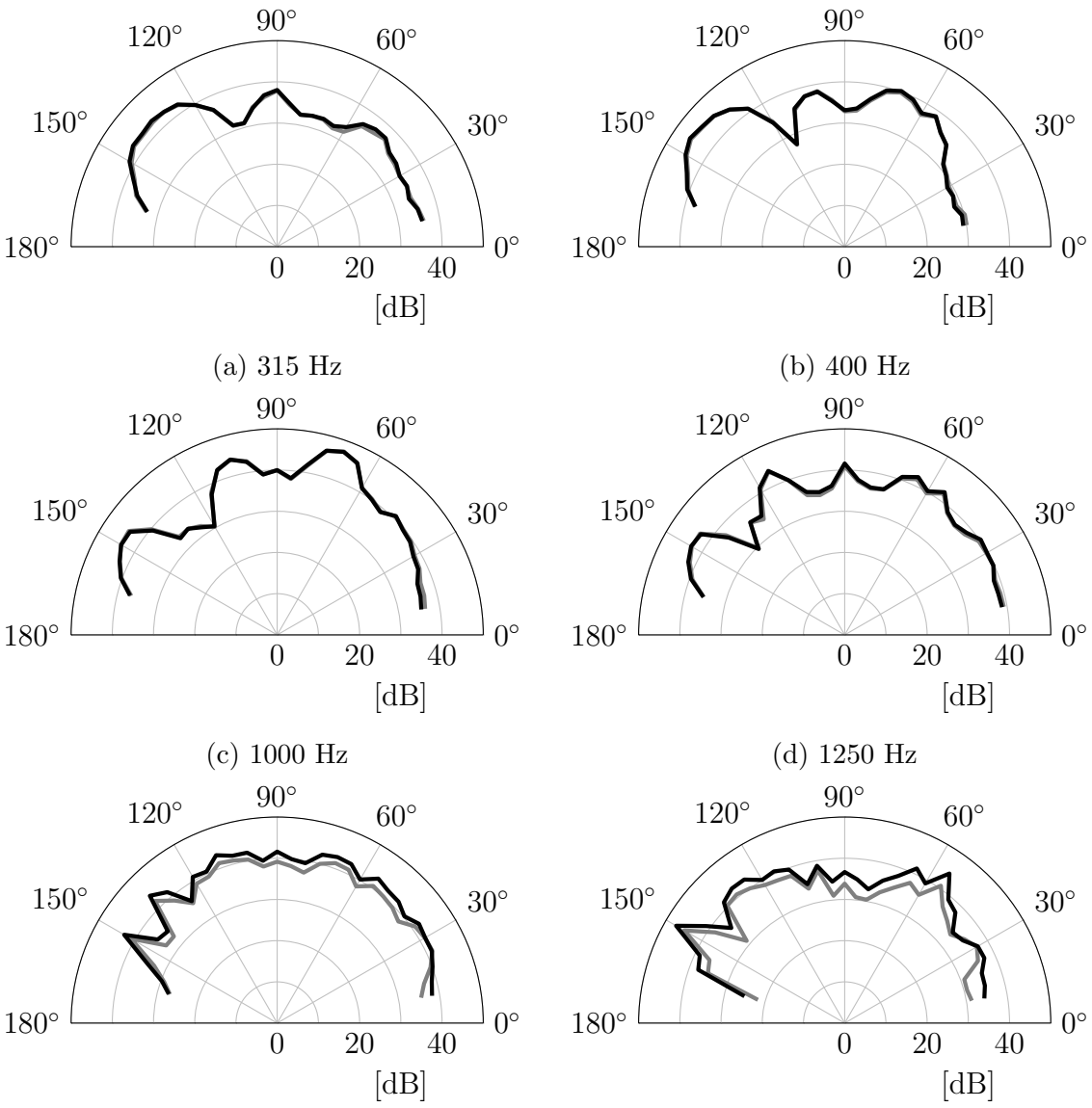

(a) 315 Hz

(b) 400 Hz

(c) 1000 Hz

(d) 1250 Hz

(e) 3150 Hz

(f) 4000 Hz

Figure 5.8: Experimental relative scattered levels for a quadratic residue diffusor are compared between a MLS signal (black curve) and a LSS signal (gray curve). The source is incident from a polar angle of 30°. One-third octave band results are shown in (a) through (f).

at a specific 1/3-octave band frequency and receiver position for a MLS signal excitation, $L_{LSS,i}$ is the relative scattered level at a specific 1/3-octave band frequency and receiver position for a LSS signal excitation, and M is the total number of receivers (32 in this case). Tables 5.1 and 5.2 show the average relative difference of the scattering by a triangular diffusor and the quadratic residue diffusor, respectively. Three columns are tabulated for source angles of incidence 30°, 60°, and 90°. The 100 Hz 1/3-octave band, in Table 5.1, shows a large inconsistency across the source angles of incidence. A possible source for this inconsistency is an increase of background noise stemming from mechanical building HVAC equipment. In contrast, from 125 Hz and upwards the average relative differences are fairly consistent across the three source angles of incidence. From 125 Hz and upward the average relative difference diminishes for increasing frequency eventually leveling off. Unlike the triangular diffusor the average relative difference increases as the frequency increases for the quadratic residue diffusor; refer to Table 5.2. In spite of the contradictory trends in the average relative difference, the polar plots in Figs. 5.7 and 5.8 indicate a scaling error at high frequencies for the quadratic residue diffusor and a low signal to noise ratio at the low frequency for the triangular diffusor. Despite the LSS signal having less signal energy, as defined by Eq. (5.20) and compared to the MLS signal, a good agreement exists between the relative scattered levels derived by either excitation signal.

5.3.2 Prediction and Measurement Comparison

A comparison between the adaptive beam tracing edge diffraction model and the goniometer measurement of the triangular diffusor tested serves the purpose of numerical validation. The essential details of the goniometer measurement are modeled. The geometry of the diffusor, extent of the measurement platform, source positions, and receiver positions are modeled. The comparison is qualitatively

Table 5.1: Average relative difference for relative scattered levels of a triangular diffusor measured by MLS and LSS.

1/3-Octave	Angle of Incidence		
Band [Hz]	30°	60°	90°
100	2.38	4.87	2.32
125	0.27	0.21	0.37
160	0.16	0.12	0.18
200	0.14	0.08	0.14
250	0.11	0.07	0.10
315	0.08	0.06	0.07
400	0.05	0.05	0.04
500	0.03	0.02	0.03
630	0.02	0.02	0.03
800	0.02	0.02	0.03
1000	0.02	0.02	0.03
1250	0.01	0.02	0.03
1600	0.02	0.02	0.03
2000	0.02	0.02	0.03
2500	0.01	0.02	0.03
3150	0.01	0.02	0.02
4000	0.01	0.02	0.03
5000	0.01	0.03	0.03
6300	0.02	0.02	0.02
8000	0.01	0.02	0.02
10000	0.01	0.04	0.02
12500	0.02	0.02	0.02
16000	0.03	0.02	0.03
20000	0.03	0.02	0.03

Table 5.2: Average relative difference for relative scattered levels of a quadratic residue diffusor measured by MLS and LSS. The frequencies are scaled down by a factor of five due to the scale size of the sample.

1/3-Octave	Angle of Incidence		
Band [Hz]	30°	60°	90°
100	0.07	0.06	0.03
125	0.06	0.05	0.03
160	0.04	0.04	0.03
200	0.02	0.03	0.03
250	0.02	0.02	0.03
315	0.01	0.01	0.03
400	0.01	0.01	0.02
500	0.01	0.01	0.02
630	0.01	0.01	0.02
800	0.01	0.01	0.02
1000	0.01	0.02	0.02
1250	0.02	0.03	0.03
1600	0.02	0.03	0.03
2000	0.02	0.03	0.04
2500	0.05	0.06	0.07
3150	0.08	0.10	0.12
4000	0.11	0.14	0.17

analyzed by an examination of the relative scattered level polar plots and the root-mean-square error between the predicted and measured results.

Figure 5.9 shows the relative scattered levels determined by experiment and prediction. The source is incident from an angle of 30°. Up to second-order diffraction is computed. The agreement between experiment and prediction is best at the 4000 Hz 1/3-octave band and gradually declines for lower 1/3-octave band frequencies. The departure from agreement is attributed to two factors, and possibly an additional third factor: the increasing importance of higher-order diffraction, the omission of reflection-diffraction combinations, and diaphragmatic absorption. Higher-order diffraction plays an essential role in the scattered field for low frequencies (Chu et al., 2007). In a similar vein the omission of reflection-diffraction combinations affects the magnitude of the scattered sound field. For example, the mechanism of wedge diffraction, reflection, and wedge diffraction is omitted, which may play an essential role in predicting the magnitude of the scattered sound field accurately at mid-frequencies. Lastly, diaphragmatic absorption possibly explains the reduced experimental magnitude of the scattered field at low frequencies (D'Antonio and Konnert, 1992). Since, the prediction assumes a perfectly rigid surface, no acoustic absorption is accounted for.

The root-mean-square error (RMSE) of the relative scattered levels between the experimental results and prediction results are tabulated in Table 5.3. The RMSE is greatest at low frequencies with the exception of 100 Hz, and 125 Hz 1/3-octave bands. The importance of including higher-order diffraction, and additional reflection-diffraction combinations is stressed by the high RMSE below 1000 Hz, which is greater than or equal to 10.0 dB for the 1/3-octave bands 160 Hz to 800 Hz. The magnitude of the RMSE is smaller for 1000 Hz and above, however, the values do not monotonically decrease to zero as the frequency increases. It is conjectured that as the frequency increases the directivity of the loudspeaker limits

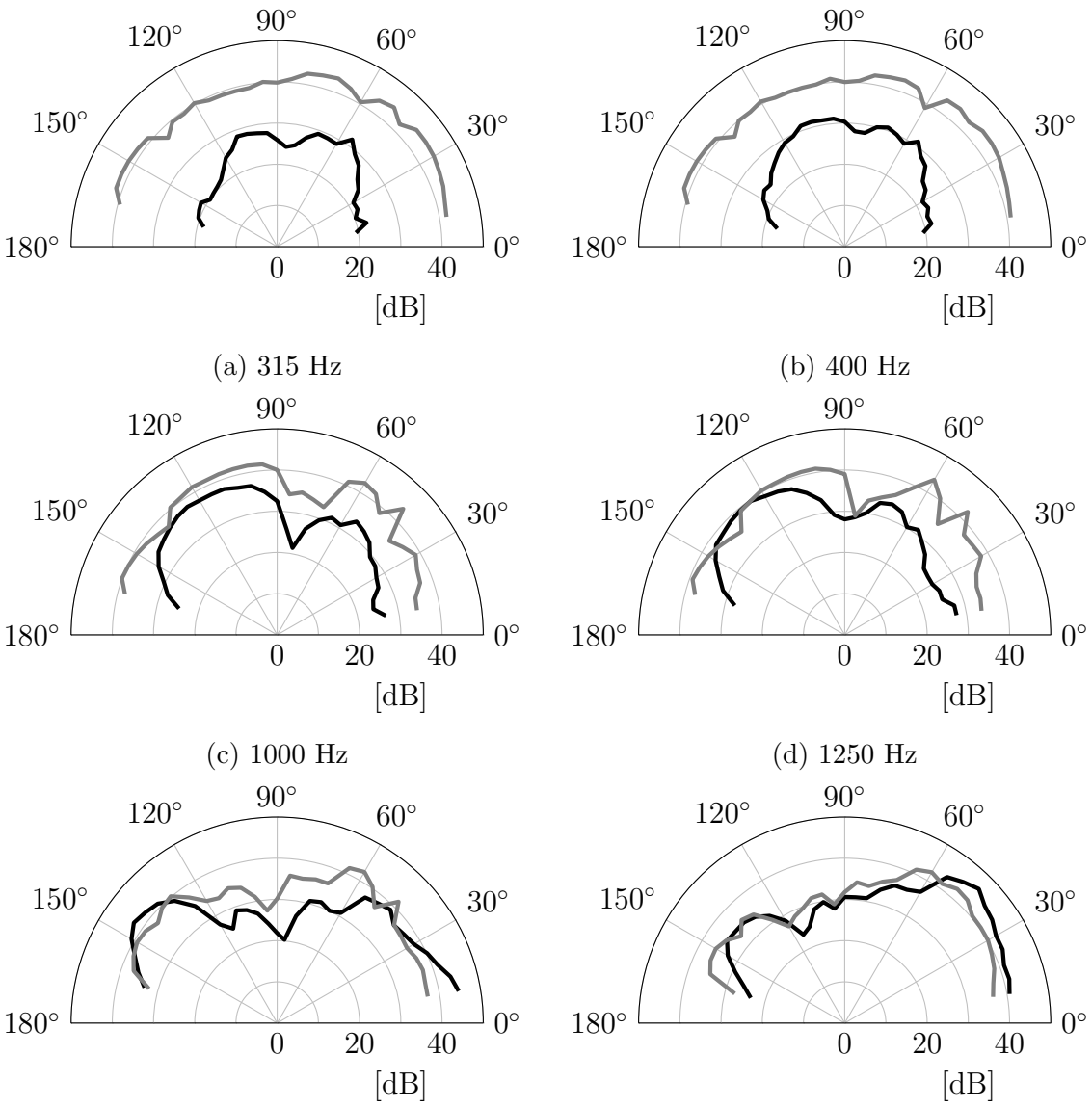

(a) 315 Hz

(b) 400 Hz

(c) 1000 Hz

(d) 1250 Hz

(e) 3150 Hz

(f) 4000 Hz

Figure 5.9: Experimental (black) versus predicted (gray) relative scattered levels for a periodic triangular diffusor. The source is incident from a polar angle of 30°. Up to second-order diffraction is computed in the prediction. One-third octave band results are shown in (a) through (f).

the agreement between prediction and measurement.

Table 5.3: Root-mean-square error of the relative scattered levels between prediction and experiment for a triangular diffusor. The diffusor is composed of six periodic triangles with base angles of 45°. The source is incident from a polar angle of 30°. The prediction includes up to second-order diffraction.

1/3-Octave Band [Hz]	RMSE [dB]
100	4.9
125	8.7
160	12.2
200	17.6
250	19.2
315	17.4
400	15.7
500	14.3
630	13.7
800	10.0
1000	8.1
1250	7.7
1600	6.4
2000	5.0
2500	5.5
3150	5.9
4000	3.6
5000	5.2
6300	4.4
8000	7.0

5.4 Summary

The theoretical aspects of a goniometer measurement show that the measurement estimates the scattered impulse response by a subtraction and deconvolution method. The method involves measuring a sample response, a background response, subtracting the two impulse responses, and deconvolving the loudspeaker to microphone impulse response. Since it is assumed that the signal to noise ratio is high, the noise is neglected and the scattered impulse response is estimated.

The goniometer measurement involves various experimental apparatus. The goniometer itself consists of a measurement platform, a 32 microphone array, and a loudspeaker. The microphone array is powered by a bank of four preamplifiers in a master-slave setup, and the loudspeaker is powered by a power amplifier. The power amplifier is connected to the master preamplifier and the four preamplifiers are connected to a measurement desktop. Physical considerations are taken into account for the purpose of conducting a measurement in a quasi-anechoic condition. It is verified that quasi-anechoic conditions are present during a measurement with the exception of a few source and receiver angles.

Measurement of acoustic scattering by a geometric diffusor and a number theoretic diffusor is conducted with two types of excitation signals. The MLS and LSS excitation signals are compared in a relative sense for the relative scattered levels derived from the measurement. In spite of containing less energy the employed LSS signal resulted in measurements that agree very well with the MLS measurements over several 1/3-octave band frequencies. The largest relative differences are for low frequencies. Finally, a numerical validation of the prediction model, developed in this dissertation, is conducted with the result that predictions are best suited for high frequencies.

Chapter 6

Conclusions

The purpose of the present study is to investigate the capabilities and limitations of a combined adaptive tetrahedral tracing and edge diffraction model. The case study of interest is the prediction of scattering by diffusors. Viewing an acoustic diffusor as an ensemble of finite reflective surfaces comprised of scattering wedges leads to a particularly useful approach. Three challenges exist in the realization of this modeling approach. The first challenge is determining, and if applicable defining, the geometric acoustics model appropriate for diffusor scattering predictions. The second challenge is to identify and define an interface between the geometric acoustic model and a edge scattering model. Lastly, the third challenge is to numerically verify, and validate the proposed approach.

6.1 General Conclusions

The first research challenge is to identify, and if necessary define, a relevant geometric acoustics model for the combined model. Of the available techniques, the adaptive beam tracing model shows the greatest promise since it maps the incident and reflected sound fields in a continuous manner. The advantage of mapping the incident and reflected sound fields continuously is evident by the capability to

identify scattering wedge parameters. The relevant literature on acoustic adaptive beam tracing omits several algorithmic aspects crucial for the physically correct mapping of incident and reflected sound fields. Upon further investigation the necessary elements were derived for the model and the algorithm termed adaptive tetrahedral tracing. The fundamental algorithmic procedures include ensonification mapping, occlusion mapping, and the subdivision of the total ensonification mapping (for further details see Sec. 3.2). An added advantage of adaptive tetrahedral tracing is the ability to map the incident and reflected sound fields on the boundaries of the geometric domain. This characteristic establishes a vital interface for an edge scattering model.

The second challenge is to identify and define an interface between the geometric acoustic model and an edge scattering model. The adaptive tetrahedral tracing algorithm maps the incident and reflected acoustic sound fields on the boundaries of the geometric domain. Once the mapping is established a system identifies the diffracting edges. The parameters of each scattering wedge are extracted from the acoustic mapping and funneled to the edge scattering model. Geometric parameters such as the wedge angle, relative cylindrical coordinates of the source and receiver, and extent of the ensonified edge are extracted from the acoustic mapping. Higher-order diffraction is treated from the perspective of graph-theory. Permutations of reflection and diffraction are enumerated through modified graph-theoretic search procedures. Details are provided in Secs. 4.1 through 4.3.

The third and final challenge is to numerically verify, and validate the combined adaptive tetrahedral tracing edge diffraction model. The model is numerically verified against three scattering geometries. Overall the agreement against analytic and boundary element predictions (BEM) predictions is good. It is determined that as the geometry of the diffusor becomes more complex, then a greater need for higher-order diffraction and additional diffraction-reflection permutations are

necessary to correctly model wave propagation at low frequencies; see Sec. 4.4. Numerical validation is conducted against goniometer measurements of two geometric diffusors. The resulting comparisons between prediction and experimental results suggests that the model requires higher-order diffraction and additional diffraction-reflection permutations for broadband predictions; see Sec. 5.3.2.

Additionally, part of the experimental portion involves an investigation into measurements with two different stimuli. Traditionally the maximum length sequence (MLS) is used most widely in the measurement of acoustic diffusors. It is of interest to examine an alternative stimuli, specifically the logarithmic swept-sine (LSS). The choice of a LSS stimuli is motivated by the fact that the method rejects harmonic distortion, and is capable of conducting measurements at a higher signal to noise ratio. Measurements of acoustic diffusors show that the LSS stimuli is an acceptable signal type since very good agreement exists for the scattered polar responses over a large frequency range when compared against measurements with MLS stimuli; see Sec. 5.3.1.

6.2 Present Challenges and Opportunities

Several opportunities are available to extend the adaptive tetrahedral tracing and edge diffraction model. One particular challenge is to dynamically identify geometry that would otherwise go undetected by the model; see Fig. 3.1(b) for an example. Small geometric features relative to the propagating tetrahedral cross-section result in one type of acoustic aliasing. Drumm and Lam (2000) claim that their algorithm identifies geometric features wholly contained within a beam, but no substantial details exist on how to dynamically identify such a scenario. The solution proposed in this study is to increase the beam density ensuring that this type of acoustic aliasing is avoided. However, this solution is far from ideal since it is based on a

trial and error process.

Another challenge is to model additional reflection-diffraction permutations. For example, the inclusion of diffraction, reflection, and diffraction combinations may improve the agreement between predictions and experiment. The challenge of computing such combinations includes modeling image edges instead of image source, and computing from region visibility (Antani et al., 2012). In the present study it is assumed that mutually visible edges are completely visible to one another. A from region visibility computation where the mutual visibility of edges are considered would correct that assumption. Furthermore, the secondary source model for edge diffraction does not account for slope diffraction (Summers, 2013). Slope diffraction is an important component of the sound field generated by wave guides (Mentzer et al., 1975). The quadratic residue diffusor and other diffusors that exhibit semi-enclosed volumes act as acoustic wave guides. Current models that compute electromagnetic slope diffraction in the time-domain may be applicable to sound propagation (Rousseau and Pathak, 1995).

Geometric domains that contain many polygons present a particular computational bottleneck for naive ray-polygon intersection queries. Approximately only half of the polygons are discarded based on the directional vector of the ray and each polygon normal. A major improvement to the adaptive tetrahedral tracing algorithm is accelerating ray-polygon intersection tests. The most notable techniques for accelerating ray-polygon intersection queries are kd-tree traversal and binary space partitioning. Binary space partitioning is used by Funkhouser et al. (2004) in a beam tracing algorithm for purpose of computing real-time auralizations. Binary space partitioning splits the geometric domain into convex parallelepipeds and constrains the query space to a subset of the total geometric domain. Another technique well-suited to adaptive tetrahedral tracing is kd-tree traversal (Overbeck et al., 2007; Hapala and Havran, 2011). Similar to binary-space

partitioning the geometric domain is split into cells that subdivide the geometric domain, which accelerates the ray-polygon query.

Lastly, modeling acoustic impedance in the time-domain is a current challenge with some approaches suggested within the literature. Going beyond rigid or anechoic boundaries requires special considerations: for example, how to model the multiple convolutions that physically occur during beam-boundary interactions. Work applied to the finite difference time-domain method (Kowalczyk and van Walstijn, 2008a,b) may find application with adaptive tetrahedral tracing. Plus, diffraction of general impedance wedges is as of now an open problem. The closest solution was developed for an isovelocity wedge with varying densities (Chu, 1989).

Bibliography

AES Standards Committee. Aes information document for room acoustics and sound reinforcement systems - characterisation and measurement of surface scattering uniformity. Technical Report AES-4id-2001 (r2007), Audio Engineering Society, Inc., 2001.

Jont B. Allen and David A. Berkley. Image method for efficiently simulating small-room acoustics. *The Journal of the Acoustical Society of America*, 65(4): 943–950, 1979.

Lakulish Antani, Anish Chandak, Micah Taylor, and Dinesh Manocha. Efficient finite-edge diffraction using conservative from-region visibility. *Applied Acoustics*, 73(3):218–233, 2012.

Andreas Asheim and U. Peter Svensson. An integral equation formulation for the diffraction from convex plates and polyhedra. *The Journal of the Acoustical Society of America*, 133(6):3681–3691, June 2013 2013.

Keith Attenborough, Kai Ming Li, and Kirill Horoshenkov. *Predicting outdoor sound*. Taylor & Francis, London ; New York, 2007.

Jørgen Bang-Jensen and Gregory Gutin. *Digraphs: theory, algorithms, and applications*. Springer, London ; New York, 2001.

Imran Bashir, Shahram Taherzadeh, and Keith Attenborough. Diffraction assisted

rough ground effect: Models and data. *The Journal of the Acoustical Society of America*, 133(3):1281–1292, 2013.

John R. Berryhill. Diffraction response for nonzero separation of source and receiver. *Geophysics*, 42(6):1158–1176, 1977.

David A. Bies and Colin H. Hansen. *Engineering noise control: theory and pratice*. Spon Press/Taylor & Francis, London ; New York, 4th edition, 2009.

M. A. Biot. Reflection on a rough surface from an acoustic point source. *The Journal of the Acoustical Society of America*, 29(11):1193–1200, 1957.

M. A. Biot and I. Tolstoy. Formulation of wave propagation in infinite media by normal coordinates with an application to diffraction. *The Journal of the Acoustical Society of America*, 29(3):381–391, 1957.

D. Botteldooren. Acoustical finite-difference time-domain simulation in a quasi-cartesian grid. *The Journal of the Acoustical Society of America*, 95(5): 2313–2319, 1994.

Patrice Boulanger, Keith Attenborough, Shahram Taherzadeh, Tim Waters-Fuller, and Kai Ming Li. Ground effect over hard rough surfaces. *The Journal of the Acoustical Society of America*, 104(3):1474–1482, 1998.

J. J. Bowman, Thomas B. A. Senior, P. L. E. Uslenghi, and J. S. Asvestas. *Electromagnetic and acoustic scattering by simple shapes*. Hemisphere Pub. Corp., New York, rev print edition, 1987.

T. J. I'A Bromwich. Diffraction of waves by a wedge. *Proceedings of the London Mathematical Society*, 14(1):450–463, 1915.

A. J. Burton and G. F. Miller. The application of integral equation methods to the numerical solution of some exterior boundary-value problems. *Proceedings of the*

Royal Society of London.Series A, Mathematical and Physical Sciences, 323 (1553):201–210, 1971.

Nicola Campo, Paolo Rissone, and Marco Toderi. Adaptive pyramid tracing: a new technique for room acoustics. *Applied Acoustics*, 61(2):199–221, 2000.

H. S. Carslaw. Diffraction of waves by a wedge of any angle. *Proceedings of the London Mathematical Society*, s2-18(1):291–306, 1920.

Dezhang Chu. Impulse response of density contrast wedge using normal coordinates. *The Journal of the Acoustical Society of America*, 86(5):1883–1896, 1989.

Dezhang Chu, Timothy K. Stanton, and Allan D. Pierce. Higher-order acoustic diffraction by edges of finite thickness. *The Journal of the Acoustical Society of America*, 122(6):3177–3194, 2007.

C. S. Clay and Wayne A. Kinney. Numerical computations of time-domain diffractions from wedges and reflections from facets. *The Journal of the Acoustical Society of America*, 83(6):2126–2133, 1988.

D. Cohen-Or, Y. L. Chrysanthou, C. T. Silva, and F. Durand. A survey of visibility for walkthrough applications. *Visualization and Computer Graphics, IEEE Transactions*, 9(3):412, 2003.

Thomas H. Cormen, Charles E. Leiserson, Ronald L. Rivest, and Clifford Stein. *Introduction to algorithms*. The MIT Press, Cambridge Massachusetts ; London, 3 edition, 2009.

T. Cox and Y. W. Lam. Prediction and evaluation of the scattering from quadratic residue diffusers. *The Journal of the Acoustical Society of America*, 95(1):297–9, 1994.

Trevor J. Cox. The optimization of profiled diffusers. *The Journal of the Acoustical Society of America*, 97(5):2928–2936, 1995.

Trevor J. Cox and Peter D'Antonio. *Acoustic absorbers and diffusers: theory, design and application*. Taylor & Francis, London ; New York, 2 edition, 2009.

Trevor J. Cox and Peter D'Antonio. Acoustic surface reflection database, 2011.

Konstantinos Dadiotis, Jamie A. S. Angus, and Trevor J. Cox. Lüke and power residue sequence diffusers. *The Journal of the Acoustical Society of America*, 123 (4):2035–2042, 2008.

Norm Dadoun, David G. Kirkpatrick, and John P. Walsh. The geometry of beam tracing. In *SCG '85: Proceedings of the first annual symposium on Computational geometry*, pages 55–61, New York, NY, USA, 1985. ACM.

Bengt-Inge L. Dalenbäck. Room acoustic prediction based on a unified treatment of diffuse and specular reflection. *The Journal of the Acoustical Society of America*, 100(2):899–909, 1996.

Peter D'Antonio. Performance evaluation of optimized diffusors. *The Journal of the Acoustical Society of America*, 97(5):2937–2941, 1995.

Peter D'Antonio and John Konnert. The directional scattering coefficient: Experimental determination. *J. Audio Eng. Soc.*, 40(12):997–1017, 1992.

Peter D'Antonio and Brian Rife. The state of the art in the measurement of acoustical coefficients. volume 12, page 015008. ASA, 2011.

I. A. Drumm. The application of adaptive beam tracing and managed directx for the visualisation and auralisation of virtual environments. In *Information Visualisation, 2005. Proceedings. Ninth International Conference*, pages 961–965, 2005.

I. A. Drumm and Y. W. Lam. The adaptive beam-tracing algorithm. *Journal of the Acoustical Society of America*, 107(3):1405–1412, 2000.

José Escolano, Finn Jacobsen, and José J. López. An efficient realization of frequency dependent boundary conditions in an acoustic finite-difference time-domain model. *Journal of Sound and Vibration*, 316(15):234–247, 2008.

Angelo Farina. Simultaneous measurement of impulse response and distortion with a swept-sine technique. 2000.

T. Funkhouser, N. Tsingos, I. Carlbom, G. Elko, M. Sondhi, J. E. West, G. Pingali, P. Min, and A. Ngan. A beam tracing method for interactive architectural acoustics. *Journal of the Acoustical Society of America*, 115(2):739–756, 2004.

W. Gander and W. Gautschi. Adaptive quadrature - revisited. *BIT*, 40(1):84–101, 2000.

Dan Givoli. *Numerical methods for problems in infinite domains*, volume 33. Elsevier, Amsterdam, 1992.

AFMG Technologies GmbH. Easera tutorial. Technical Report EASERA 1.2, AFMG Technologies GmbH, 2012.

Oriol Guasch and Lluis Cortes. Graph theory applied to noise and vibration control in statistical energy analysis models. *The Journal of the Acoustical Society of America*, 125(6):3657–3672, 2009.

W. James Hadden, Jr. and Allan D. Pierce. Sound diffraction around screens and wedges for arbitrary point source locations. *The Journal of the Acoustical Society of America*, 69(5):1266–1276, 1981.

Thorkild Hansen and Arthur D. Yaghjian. *Plane-wave theory of time-domain fields: near-field scanning applications*. IEEE Press, New York, NY, 1999.

M. Hapala and V. Havran. Review: Kd-tree traversal algorithms for ray tracing. *Computer Graphics Forum*, 30(1):199–213, 2011.

Jonathan A. Hargreaves and Trevor J. Cox. A transient boundary element method model of schroeder diffuser scattering using well mouth impedance. *The Journal of the Acoustical Society of America*, 124(5):2942–2951, 2008.

T. Hargreaves, T. Cox, Y. Lam, and P. D'Antonio. Surface diffusion coefficients for room acoustics: Free-field measures. *The Journal of the Acoustical Society of America*, 108(4):1710–1720, 2000.

M. H. Hayes. *Statistical digital signal processing and modeling*. John Wiley & Sons, New York, 1996.

Paul S. Heckbert and Pat Hanrahan. Beam tracing polygonal objects. In *SIGGRAPH '84: Proceedings of the 11th annual conference on Computer graphics and interactive techniques*, pages 119–127, New York, NY, USA, 1984. ACM.

K. Ito. *Encyclopedic Dictionary of Mathematics: The Mathematical Society of Japan*, volume 1. MIT Press, 1993.

Cheol-Ho Jeong. Absorption and impedance boundary conditions for phased geometrical-acoustics methods. *The Journal of the Acoustical Society of America*, 132(4):2347–2358, 2012.

Wayne A. Kinney, C. S. Clay, and Gerald A. Sandness. Scattering from a corrugated surface: Comparison between experiment, helmholtz–kirchhoff theory, and the facet-ensemble method. *The Journal of the Acoustical Society of America*, 73(1):183–194, 1983.

Lawrence E. Kinsler, Austin R. Frey, Alan B. Coppens, and James V. Sanders. *Fundamentals of acoustics*. Usa, John Wiley & Sons. Inc., fourth edition, 2000.

R. G. Kouyoumjian and P. H. Pathak. A uniform geometrical theory of diffraction for an edge in a perfectly conducting surface. *Proceedings of the IEEE*, 62(11): 1448, 1974.

Konrad Kowalczyk and Maarten van Walstijn. Modeling frequency-dependent boundaries as digital impedance filters in fdtd and k-dwm room acoustics simulations. *J.Audio Eng.Soc*, 56(7/8):569–583, 2008a.

Konrad Kowalczyk and Maarten van Walstijn. Formulation of locally reacting surfaces in fdtd/k-dwm modelling of acoustic spaces. *Acta Acustica united with Acustica*, 94(6):891–906, 2008b.

Andrzej Kulowski. Algorithmic representation of the ray tracing technique. *Applied Acoustics*, 18(6):449–469, 1985.

T. I. Laakso, V. Valimaki, M. Karjalainen, and U. K. Laine. Splitting the unit delay [fir/all pass filters design]. *Signal Processing Magazine, IEEE*, 13(1):30–60, 1996.

H. Lehnert. Systematic-errors of the ray-tracing algorithm. *Applied Acoustics*, 38 (2-4):207–221, 1993.

T. Lewers. A combined beam tracing and radiant exchange computer-model of room acoustics. *Applied Acoustics*, 38(2-4):161–178, 1993.

Marshall Long. *Architectural acoustics*. Elsevier/Academic Press, Amsterdam ; Boston, 2006.

Charles Loop. Smooth subdivision surfaces based on triangles. Master's thesis, University of Utah, 1987.

R. J. Lucas and V. Twersky. Coherent response to a point source irradiating a rough plane. *The Journal of the Acoustical Society of America*, 76(6):1847–1863, 1984.

H. M. Macdonald. A class of diffraction problems. *Proceedings of the London Mathematical Society*, 14(1):410–427, 1915.

F. J. MacWilliams and N. J. A. Sloane. Pseudo-random sequences and arrays. *Proceedings of the IEEE*, 64(12):1715–1729, 1976.

Z. Maekawa. Noise reduction by screens. *Applied Acoustics*, 1(3):157, 1968.

H. Medwin. Shadowing by finite noise barriers. *The Journal of the Acoustical Society of America*, 69(4):1060–1064, 1981.

Herman Medwin, Emily Childs, and Gary M. Jebsen. Impulse studies of double diffraction: A discrete huygens interpretation. *The Journal of the Acoustical Society of America*, 72(3):1005–1013, 1982.

C. Mentzer, L. Peters Jr., and R. Rudduck. Slope diffraction and its application to horns. *Antennas and Propagation, IEEE Transactions*, 23(2):153–159, 1975.

E. Mommertz and Swen Müller. Measuring impulse responses with digitally pre-emphasized pseudorandom noise derived from maximum-length sequences. *Applied Acoustics*, 44(3):195–214, 1995.

Swen Müller and Paulo Massarani. Transfer-function measurement with sweeps. *Journal of the Audio Engineering Society*, 49(6):443–471, 2001.

Jorge C. Novarini and Herman Medwin. Computer modeling of resonant sound scattering from a periodic assemblage of wedges: Comparison with theories of diffraction gratings. *The Journal of the Acoustical Society of America*, 77(5): 1754–1759, 1985.

Alan V. Oppenheim, Ronald W. Schafer, and John R. Buck. *Discrete-time signal processing*. Prentice Hall, Upper Saddle River, N.J., 2 edition, 1999.

Joseph O'Rourke. *Computational geometry in C*. Cambridge University Press, Cambridge UK, 2 edition, 1998.

Ryan Overbeck, Ravi Ramamoorthi, and William R. Mark. A real-time beam tracer with application to exact soft shadows. In *EuroGraphics Symposium on Rendering*, June 2007.

P. Peterson. Simulating the response of multiple microphones to a single acoustic source in a reverberant room. *The Journal of the Acoustical Society of America*, 80(5):1527–3, 1986.

Allan D. Pierce. Diffraction of sound around corners and over wide barriers. *The Journal of the Acoustical Society of America*, 55(5):941–955, 1974.

Sylvain Pion and Monique Teillaud. *3D Triangulations*. CGAL Editorial Board, 4.3 edition, 2013.

Mark A. Poletti. Linearly swept frequency measurements, time-delay spectrometry, and the wigner distribution. *Journal of the Audio Engineering Society*, 36(6): 457–468, 1988.

J. Redondo, R. Pico, B. Roig, and M. R. Avis. Time domain simulation of sound diffusers using finite-difference schemes. *Acta Acustica united with Acustica*, 93 (4):611–622, 2007.

Christoph Richter, Junis Abdel Hay, Łukasz Panek, Norbert Schönwald, Stefan Busse, and Frank Thiele. A review of time-domain impedance modelling and applications. *Journal of Sound and Vibration*, 330(16):3859–3873, 2011.

P. R. Rousseau and P. H. Pathak. Time-domain uniform geometrical theory of diffraction for a curved wedge. *Antennas and Propagation, IEEE Transactions*, 43 (12):1375–1382, 1995.

S1. American national standard specification for octave-band and fractional-octave-band analog and digital filters. Technical Report ANSI S1.11-1986, American Institute of Physics, 1986.

H. Schenck. Improved integral formulation for acoustic radiation problems. *The Journal of the Acoustical Society of America*, 44(1):41–18, 1968.

J. Schoukens, R. Pintelon, E. van der Ouderaa, and J. Renneboog. Survey of excitation signals for fft based signal analyzers. *Instrumentation and Measurement, IEEE Transactions on*, 37(3):342–352, 1988.

M. R. Schroeder. Diffuse sound reflection by maximum - length sequences. *The Journal of the Acoustical Society of America*, 57(1):149–150, 1975.

M. R. Schroeder. Binaural dissimilarity and optimum ceilings for concert halls: More lateral sound diffusion. *The Journal of the Acoustical Society of America*, 65(4):958–963, 1979.

M. R. Schroeder and R. Gerlach. Response to "comments on 'diffuse sound reflection by maximum length sequences' ". *The Journal of the Acoustical Society of America*, 60(4):954, 1976.

A. Sommerfeld and R. J. Nagem. *Mathematical Theory of Diffraction: Based on Mathematische Theorie Der Diffraction*. Birkhäuser, 2004.

Arnold Sommerfeld. *Partial differential equations in physics*, volume 1. Academic Press, New York, 1949.

Guy-Bart Stan, Jean-Jacques Embrechts, and Dominique Archambeau. Comparison of different impulse response measurement techniques. *Journal of the Audio Engineering Society*, 50(4):249–262, 2002.

Uwe M. Stephenson. Quantized pyramidal beam tracing - a new algorithm for room acoustics and noise immission prognosis. *Acta Acustica united with Acustica*, 82: 517–525(9), 1996.

Uwe M. Stephenson. Can also diffracted sound be handled as flow of particles? some new results of a beam tracing approach based on the uncertainty principle. *The Journal of the Acoustical Society of America*, 123(5):3759, 2008.

Uwe M. Stephenson. An analytically derived sound particle diffraction model. *Acta Acustica United with Acustica*, 96(6):1051–1068, 2010a.

Uwe M. Stephenson. An energetic approach for the simulation of diffraction within ray tracing based on the uncertainty relation. *Acta Acustica United with Acustica*, 96(3):516–535, 2010b.

Jason E. Summers. Inaccuracy in the treatment of multiple-order diffraction by secondary-edge-source methods. *The Journal of the Acoustical Society of America*, 133(6):3673–367, 2013.

U. P. Svensson and P. T. Calamia. Edge-diffraction impulse responses near specular-zone and shadow-zone boundaries. *Acta Acustica United With Acustica*, 92(4):501–512, 2006.

U. Peter Svensson, Roger I. Fred, and John Vanderkooy. An analytic secondary source model of edge diffraction impulse responses. *The Journal of the Acoustical Society of America*, 106(5):2331–2344, 1999.

T. Terai. On calculation of sound fields around three dimensional objects by integral equation methods. *Journal of Sound and Vibration*, 69(1):71–100, 1980.

Lonny L. Thompson. A review of finite-element methods for time-harmonic

acoustics. *The Journal of the Acoustical Society of America*, 119(3):1315–1330, 2006.

R. Torres, U. P. Svensson, and M. Kleiner. Computation of edge diffraction for more accurate room acoustics auralization. *The Journal of the Acoustical Society of America*, 109(2):600–11, 2001.

Vesa Välimäki. *Discrete-Time Modeling of Acoustic Tubes Using Fractional Delay Filters*. PhD thesis, Helsinki University of Technology, 1995.

John Vanderkooy. Aspects of mls measuring systems. *J. Audio Eng. Soc.*, 42(4): 219–231, 1994.

Michael Vorländer. *Auralization*. 2008.

Andrew Wareing. Acoustical modeling of rooms with extended-reaction surfaces. Master's thesis, University of British Columbia, 2000.

Andrew Wareing and Murray Hodgson. Beam-tracing model for predicting sound fields in rooms with multilayer bounding surfaces. *The Journal of the Acoustical Society of America*, 118(4):2321–2331, 2005.

J. A. C. Weideman. Computation of the complex error function. *SIAM Journal on Numerical Analysis*, 31(5):1497–1518, 1994.

Fujio Yamaguchi. *Computer-aided geometric design: a totally four-dimensional approach*. Springer, Tokyo ; New York, 2002.

Mariette Yvinec. *2D Triangulations*. CGAL Editorial Board, 4.3 edition, 2013.

O. C. Zienkiewicz, Robert L. Taylor, and Perumal Nithiarasu. *The finite element method for fluid dynamics*. Elsevier Butterworth-Heinemann, Amsterdam; Boston, 6th edition, 2005a.

O. C. Zienkiewicz, Robert L. Taylor, and J. Z. Zhu. *The finite element method*. Elsevier Butterworth-Heinemann, Amsterdam; Boston, 6th edition, 2005b.